Physical Mechanisms Controlling Self-Aggregation of Convection in Idealized Numerical Modeling Simulations

by

Allison A. Wing

B.S. Atmospheric Science, Cornell University (2008)

Submitted to the Department of Earth, Atmospheric and Planetary Sciences
in partial fulfillment of the requirements for the degree of

Doctor of Philosophy

at the

MASSACHUSETTS INSTITUTE OF TECHNOLOGY

June 2014

Author .....
Department of Earth, Atmospheric and Planetary Sciences
March 14, 2014

Certified by .....
Kerry Emanuel
Cecil & Ida Green Professor of Atmospheric Science
Thesis Supervisor

Accepted by .....
Robert van der Hilst
Schlumberger Professor of Earth Sciences
Head, Department of Earth, Atmospheric and Planetary Sciences

Physical Mechanisms Controlling Self-Aggregation of Convection in Idealized Numerical Modeling Simulations

by

Allison A. Wing

Submitted to the Department of Earth, Atmospheric and Planetary Sciences
on March 14, 2014, in partial fulfillment of the
requirements for the degree of
Doctor of Philosophy

Abstract

The ubiquity of cloud clusters and their role in modulating radiative cooling and the moisture distribution underlines the importance of understanding how and why tropical convection organizes. In this work, the fundamental mechanism underlying the self-aggregation of convection is explored using a cloud resolving model. The objective is to identify and quantify the interactions between the environment and the convection that allow the convection to spontaneously organize into a single cluster. Specifically, the System for Atmospheric Modeling is used to perform 3-d cloud system resolving simulations of radiative-convective equilibrium in a non-rotating framework, with interactive radiation and surface fluxes and fixed sea surface temperature.

Self-aggregation only occurs at sea surface temperatures above a certain threshold. As the system evolves to an aggregated state, there are large changes to domain averaged quantities important to climate, such as radiative fluxes and moisture. Notably, self-aggregation begins as a dry patch that expands, eventually forcing all the convection into a single clump. Thus, when examining the initiation of self-aggregation, we focus on processes that can amplify this initial dry patch.

Sensitivity tests suggest that wind-dependent surface fluxes and interactive longwave radiative fluxes are important for permitting self-aggregation. A novel method is introduced to quantify the magnitudes of the various feedbacks that control self-aggregation within the framework of the budget for the spatial variance of column - integrated frozen moist static energy. The absorption of shortwave radiation by atmospheric water vapor is found to be a key positive feedback in the evolution of aggregation. In addition, there is a positive wind speed - surface flux feedback whose role is to counteract a negative air-sea enthalpy disequilibrium - surface flux feedback. The longwave radiation - water vapor feedback transitions from positive to negative in the early and intermediate stages of aggregation. The longwave radiation - cloud feedback is the dominant positive feedback that maintains the aggregated state once it develops. Importantly, the mechanisms that maintain the aggregated state are distinct from those that instigate the evolution of self-aggregation. These results and those of a companion study suggest that the temperature dependence of

self-aggregation enters through the longwave feedback term.

Thesis Supervisor: Kerry Emanuel
Title: Cecil & Ida Green Professor of Atmospheric Science

Acknowledgments

The five and a half years I have spent as a graduate student at MIT have been both rewarding and challenging, and I can't believe that they have gone by already. I am grateful to have been a part of such an incredible community in PAOC and EAPS.

First and foremost, I'd like to thank my advisor, Kerry Emanuel, for taking me on as a graduate student and providing invaluable guidance and support over the years. I remember the first time I met Kerry; he was participating in a book signing at the AMS Annual Meeting. After awkwardly hovering around the book signing table until the line had diminished, I worked up the courage to introduce myself to him. I told him I had applied to MIT and was very interested in working him. I was a bit starstruck meeting such a renowned hurricane expert, and couldn't think of anything else to say, so I bought his book and asked him to sign it (a worthwhile purchase, "Divine Wind" is an excellent book on hurricanes). Kerry, of course, was as gracious as ever, and a few weeks later I received my acceptance letter. If I have managed to absorb even a small fraction of his vast knowledge of tropical meteorology and atmospheric dynamics over the years, I am much wiser for it.

I'd also like to thank my thesis committee, Paul O'Gorman, Zhiming Kuang, and Adam Sobel, for their time and assistance, and for sharing many useful thoughts and suggestions regarding my research. I'd especially like to thank Adam for traveling up from New York to attend committee meetings, and for giving me my first experience in atmospheric science research while I was an undergraduate. I'd also like to thank Kerry, Lodovica Illari, and Raf Ferrari for giving me the opportunity to serve as a teaching assistant in their courses, which was an enjoyable, if time consuming, experience. Lodo, especially, has inspired me with her enthusiasm for teaching and meteorology and I am glad I had the chance to participate in DEAPS and WxChallenge with her.

My graduate school experience would have not been nearly as successful or enjoyable without the friendship and assistance of the other students in PAOC. I'd like to thank all my officemates over the years for making 54-1611 and 54-1815 such

pleasant places to work in every day. I have been lucky enough to make many close friends amongst my fellow grad students, and thank Mike Byrne, Morgan O'Neill, Dan Chavas, Marty Singh, Neil Zimmerman, Tim Cronin, and Malte Jansen for their friendship and support. Science-wise, I'm especially grateful to Tim for helping me figure out the peculiarities of the model named SAM and sharing his analysis scripts.

Finally, I'd like to thank my family: my parents, Peggy and Paul, and my sister, Jacki. They have been there for me through thick and thin and I truly would not be where I am today without their love and support. They have shared in my successes and believed in me even when I didn't believe in myself. I dedicate this thesis to them.

This work was supported by NSF grants 1032244, 1136480, and 0850639. For my first year as a graduate student, I was funded by an AMS Graduate Fellowship, sponsored by NASA's Earth Science Enterprise. I have also been funded by the MIT Joint Program on the Science and Policy of Global Change. I'd like to thank Marat Khairoutdinov for providing SAM, the cloud resolving model, and for many helpful conversations regarding its use. I'd also like to acknowledge high-performance computing support from Bluefire and Yellowstone provided by NCAR's Computational and Information Systems Laboratory, sponsored by the National Science Foundation. Much of this thesis was published as part of Wing, A.A., and K.A. Emanuel (2013), Physical mechanisms controlling self-aggregation of convection in idealized numerical modeling simulations, *J. Adv. Model. Earth. Syst., 5*, doi:10.1002/2013MS000269, and is reproduced here with permission and adapted in accordance with the Creative Commons Attribution License.

Contents

List of Figures

List of Tables

Chapter 1

Introduction

1.1 Motivation

Moist convection in the tropical atmosphere is often organized into clusters containing many individual convective cells. This organized convection spans a range of scales, from squall lines (∼10 km) (e.g., Houze, 1977), to mesoscale convective complexes (∼100 km) (e.g., Maddox, 1980), to tropical cyclones (∼1000 km) (e.g., Lee, 1989; Challa and Pfeffer, 1990; Simpson et al., 1997) to the Madden-Julian Oscillation (∼10,000 km)(e.g., Madden and Julian, 1971). Clusters of organized convection are ubiquitous in the tropics (Machado and Rossow, 1993; Mapes and Houze Jr., 1993; Nesbitt et al., 2000; Houze Jr., 2004; Futyan and Del Genio, 2007; Mapes et al., 2009) and have important impacts on weather and climate. For instance, convective cloud clusters are responsible for much of the rainfall and cloudiness over the tropics, with approximately 50% of tropical rainfall due to mesoscale convective systems (Nesbitt et al., 2000). Tropical cloud clusters modulate the radiative heating of the surface and atmosphere and influence the large-scale circulation and moisture distribution of the atmosphere. In idealized modeling studies (e.g., Bretherton et al., 2005), the development of large-scale convective organization alters the mean vertical profiles of temperature, moisture, and radiative fluxes, highlighting the potentially important effect of organized convection on variables important to climate. Tobin et al. (2012) found a systematic dependence of water vapor, turbulent surface fluxes, and radiation

on the degree of convective aggregation in observations. They found that aggregated convection is associated with lower free tropospheric humidity in the non-convecting environment, enhanced turbulent surface fluxes within and outside convective areas, and reduced low- to mid-level cloudiness in the environment. If the degree of aggregation changes as climate warms, these effects could have important consequences for the water vapor feedback and climate sensitivity.

The value of understanding how convection organizes cannot be overstated. First, investigating tropical convective organization has direct relevance to improving our knowledge of tropical cyclone genesis, which has implications both for operational forecasting and predictions of the response of tropical cyclones to climate change. Tropical cyclogenesis is one of the most intriguing yet poorly understood problems in tropical meteorology. The human and economic impacts of tropical cyclones give heightened significance to understanding and predicting their behavior. Second, understanding the mechanisms by which convection self-organizes may lead to insights into the Madden - Julian Oscillation, which can be considered convective organization on a large scale. The MJO has a direct impact on weather in the Indian and western Pacific Oceans, modulates tropical cyclone activity, and influences weather at extratropical latitudes through atmospheric teleconnections, yet, a complete theory for its existence and propagation characteristics remains elusive. Finally, tropical cloud clusters modulate the radiative balance and moisture distribution in the tropics and therefore influence the large-scale circulation, making them a potentially vital part of the climate system that is not well understood. Understanding how and why tropical convection organizes is important for understanding both tropical and global climate variability.

Tropical convection is often viewed as a quasi-equilibrium process in which convective clouds consume convective available potential energy at the same rate it is supplied by large-scale processes (Arakawa and Schubert, 1974). The simplest form of such an equilibrium is radiative-convective equilibrium (RCE), in which radiative cooling is balanced by convective heating. On large enough space and time scales, the tropics can be thought of as in RCE, although RCE is not observed locally due

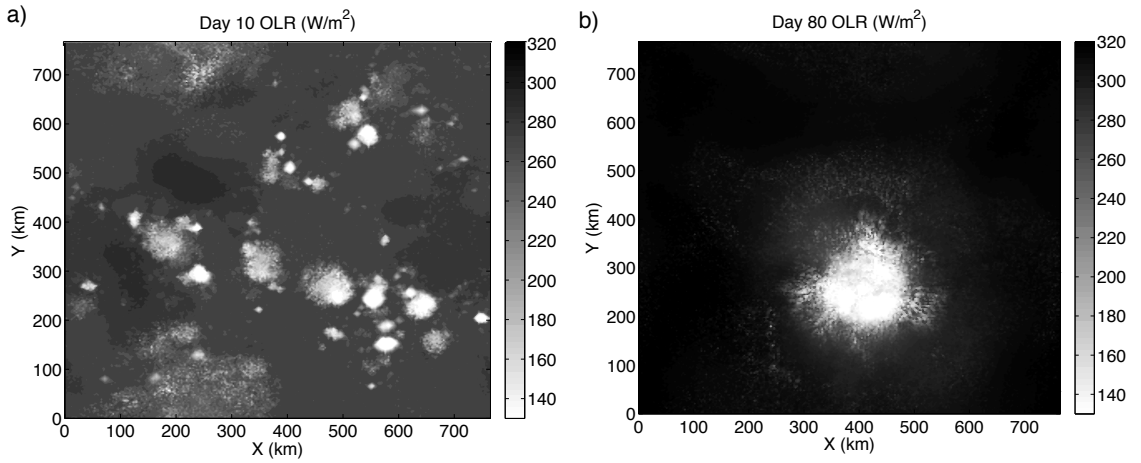

Figure 1-1: Snapshot of outgoing longwave radiation (OLR) at day 10 (panel a) and day 80 (panel b) of a radiative-convective equilibrium simulation at 305 K.

to the presence of large-scale atmospheric circulations. Nevertheless, RCE is a good starting point for understanding tropical dynamics. Simulations of convection in RCE using three-dimensional cloud system resolving models often produce distributions of convection that are nearly random in space and in time (Islam et al., 1993). However, when certain conditions are met, the convection becomes organized into a single, intensely convecting moist cluster surrounded by a broad region of dry subsiding air (e.g., Bretherton et al., 2005; Nolan et al., 2007). Figure 1-1 shows an example of a three-dimensional RCE simulation that transitions from disorganized convection in the beginning of the simulation (Figure 1-1a) to a single cluster (Figure 1-1b) 70 simulated days later. The details of that simulation will be given in Chapter 2.

Convection is often thought of as being organized by external influences such as large-scale sea surface temperature (SST) gradients or wind shears (e.g., Robe and Emanuel, 2001). However, in the case shown in Figure 1-1, there are no such external influences. Convection is instead self-organizing through interactions between the environment and the convection and radiation, which is referred to as "self-aggregation". Insights from previous work on tropical cloud clusters and self-aggregation are reviewed in the remainder of this chapter.

1.2 Review of Previous Work

1.2.1 Observational Studies

It has long been known that convection in nature sometimes organizes and that clusters of convection can possess a distinctive mesoscale structure (e.g., Houze, 1977; Maddox, 1980). In midlatitudes, cloud clusters with mesoscale organization are often called mesoscale convective systems (MCS). There is an extensive literature detailing the climatology and life cycles of these systems (as well as mesoscale convective complexes, or MCC's, which are a subset of MCS's). In the tropics, such systems are sometimes referred to as "cloud clusters" or "convective systems", but they exhibit similar characteristics to their midlatitude brethren (e.g., Machado et al., 1998). Many of the studies on cloud cluster observations focus on MCS's or MCC's, (the criteria for being classified as such will be reviewed later), (e.g., Miller and Fritsch, 1991; Laing and Fritsch, 1993a,b; Velasco and Fritsch, 1987; Laing and Fritsch, 1997), while comparatively fewer focus on cloud clusters/deep convective systems in general (Machado and Rossow, 1993; Mapes and Houze Jr., 1993; Futyan and Del Genio, 2007; Peters et al., 2009; Hennon et al., 2013).

Laing and Fritsch (1997) compiled a global population of mesoscale convective complexes characterized by a large ($10^5\,m^2$), long-lasting($6\,hr$), quasi-circular cold cloud shield. Figure 1-2 shows the global distribution of MCC's from their survey. As evident in the Figure 1-2, the vast majority of MCC's occur over land. Laing and Fritsch also determined that the global population of MCC's is primarily nocturnal, although oceanic MCC's end much later in the morning than land ones. The oceanic systems were also larger and longer lasting than other systems, and there was a general tendency for larger systems to persist longer. They also noted that the population shifts with the seasonal cycle and the size, location, and frequency of MCC's is sensitive to the larger scale pattern and its interannual variability, although the total number of MCC's occurring did not vary greatly from year to year. Velasco and Fritsch (1987), whose study on MCC's in the Americas was a member of the Laing and Fritsch survey, noted that the most active areas were ones in which warm

Figure 1-2: Global distribution of mesoscale convective complexes and regions of widespread frequent deep convection as inferred by OLR minima (light shading). OLR measurements obtained from Earth Radiation Budget Experiment for July (above the line) and January (below the line), 1985-1986. From Laing and Fritsch (1997), Copyright ©1997 Royal Meteorological Society.

water, orographic lifting, and large scale, low-level convergence combine to focus and enhance deep convection.

While the study of Laing and Fritsch focused on MCC's, Machado and Rossow (1993) examined the structural characteristics and radiative properties of, more generally, tropical cloud clusters, which they define as all tropical high cloud systems including both the small individual deep convective plumes and the larger MCS's. Like MCC's, they found that all convective systems are more numerous over land than ocean, but the oceanic systems are larger and longer-lived. Figure 1-3 shows the frequency of convective systems in the tropics, which is broadly consistent with Figure 1-2 [1]. Machado and Rossow (1993) also used a radiative transfer model to evaluate the local radiative effects of convective systems with average cloud properties, finding that they caused a decrease in radiative cooling, primarily through the effects of the mesoscale anvil cloud. There is also evidence that cloud clusters span a somewhat lognormal size distribution (Mapes and Houze Jr., 1993). Mapes and Houze Jr. (1993) noted that there is also a pronounced diurnal variation in the total number of and area covered by large clusters, peaking in the early morning. The overall diurnal

[1]It should be noted that the MCC's plotted in Figure 1-2 were defined by a strict size criterion, whereas Machado and Rossow did not have a size criterion, thus identifying many more small convective systems.

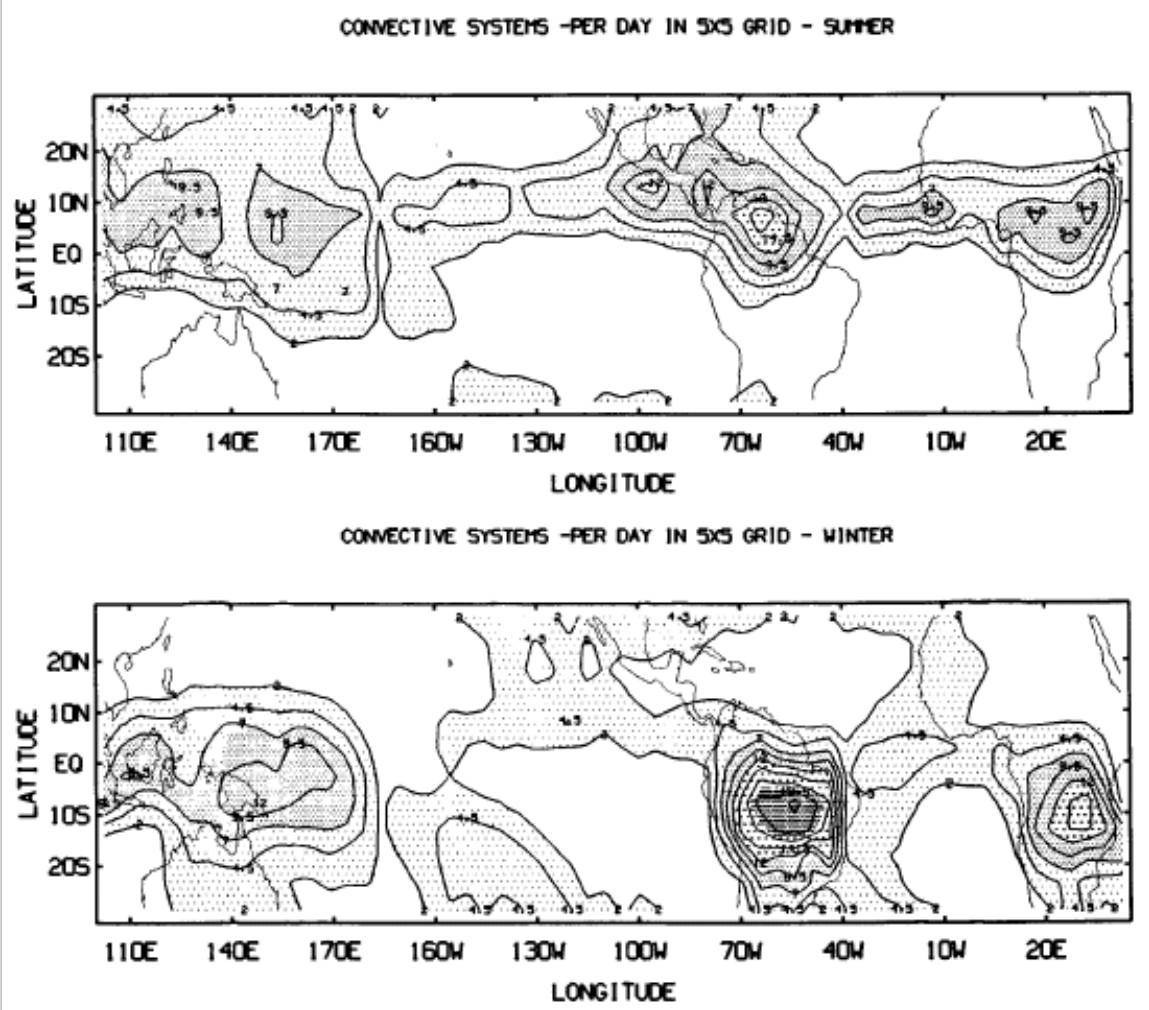

Figure 1-3: Maps of the average number per day of convection systems occuring in $5°x\,5°$ latitude-longitude regions in the tropics for summer (July-August 1987 and 1988) (top panel) and winter (January-February 1987 and 1988) (bottom panel). Lowest contour is 2 per day. From Machado and Rossow (1993) ©American Meteorological Society. Used with permission.

variation in very cold cloudiness is dominated by the large-cluster variation, but the moderately cold cloud area differs and has a peak in the afternoon. Mapes et al. (2009) examined the life cycles of maritime tropical mesoscale convective systems [2] in microwave and scatterometer satellite observations. They determined that the life cycle evolution is universal for all non-tropical cyclone convective cloud clusters. All the MCS populations (subdivided into dry, humid, moderately rotating, tropical cyclone) showed a similar evolution in vorticity, divergence, precipitable water, and IR brightness temperature (Figure 1-4). The peak in precipitation leads the minimum in brightness temperature by a few hours. Finally, Peters et al. (2009) emphasized the importance of water vapor in their study of precipitation clusters [3] identified from TRMM precipitation radar data. They found that the size distribution changes dramatically as a function of water vapor, with most large clusters occurring at or near critical water vapor values. They also noted that for values of water vapor near and above criticality, the cluster generally exists in a dryer environment.

The role of tropical cloud clusters as precursors to tropical cyclones motivated Hennon et al. (2011) to develop an objective algorithm for detecting and tracking tropical cloud clusters, including identifying whether a cluster has developed into a tropical cyclone. Figure 1-5 shows the density of global tropical cloud cluster activity from 1988 to 2007, indicating that the highest concentrations of tropical cloud clusters occur in the ITCZ, South Pacific Convergence Zone, in the eastern North Indian Ocean associated with the monsoon, and in the eastern Atlantic associated with African Easterly Waves. This figure, which includes only oceanic cloud clusters, is qualitatively similar to the spatial distribution of convective systems found by Machado and Rossow (1993) (Figure 1-3). Hennon et al. (2013) analyzed the interannual and interdecadal variability of tropical cloud clusters as well as genesis productivity in the Hennon et al. (2011) database. They found that globally, 6.4 % of tropical cloud clusters develop into tropical cyclones per year. The annual tropical cloud cluster frequency was strongly correlated to sea surface temperatures in some

[2] Although they use the term MCS, they include systems smaller than often considered a MCS; cloud systems with a time-mean size of two pixels (0.5 square degrees) or larger).

[3] Defined as any collection of adjacent radar pixels indicating precipitation (reflectivity $\geq 20 dBz$).

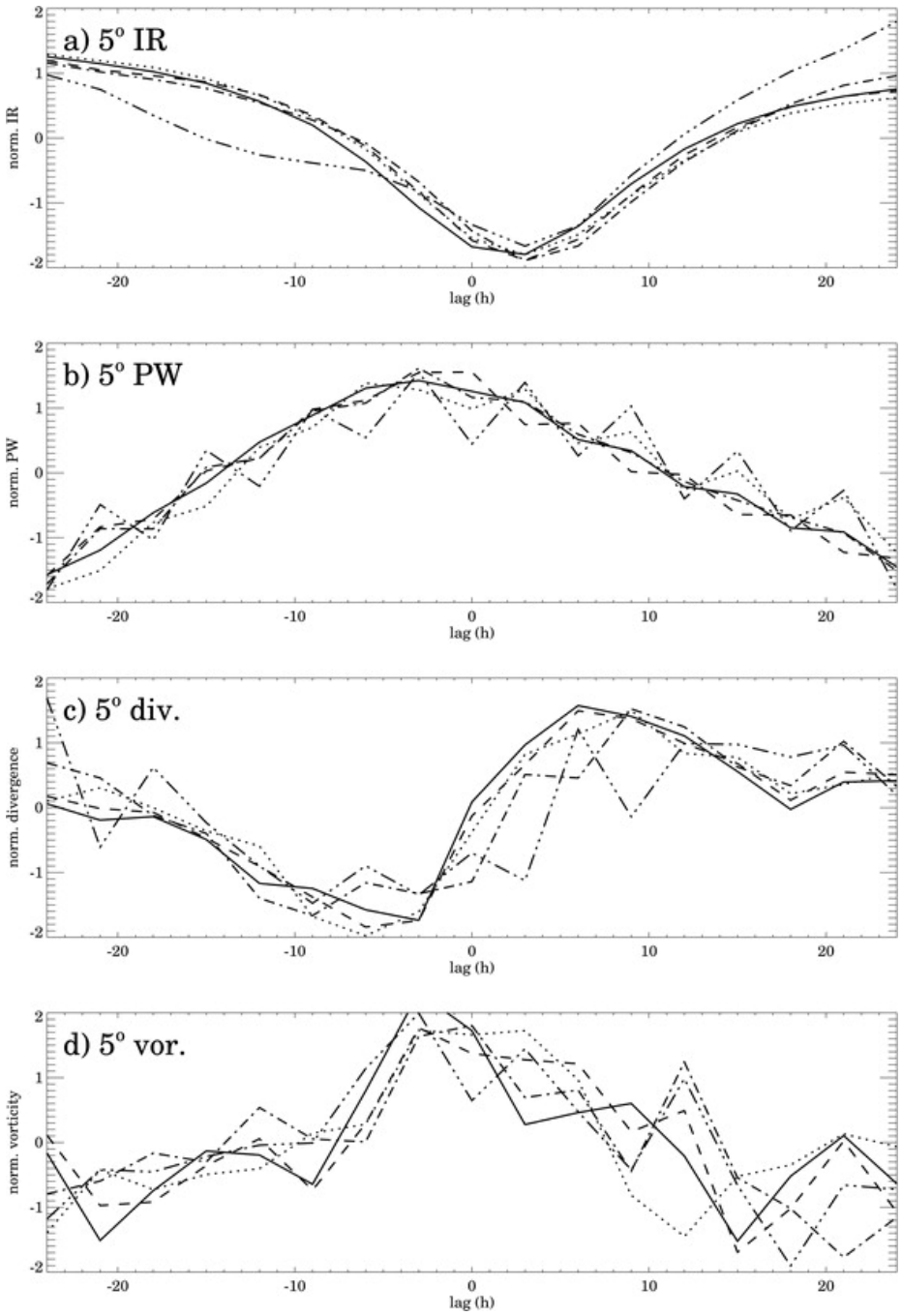

Figure 1-4: Normalized composite time series for centered 5° boxes. Solid: one pixel systems in weak rotation; dotted: dry; dashed: humid; dashed-dotted: moderate rotation; dashed-triple dotted: tropical cyclone. From Mapes et al. (2009) ©American Meteorological Society. Used with permission.

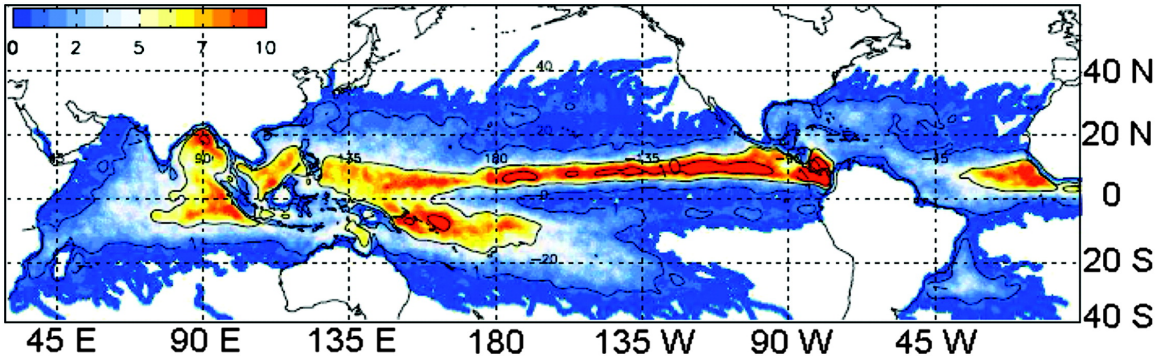

Figure 1-5: The number of tropical cloud clusters per year (for the 10-yr period of 1998-2007) that tracked within 55 km of a grid point. From Hennon et al. (2011) ©American Meteorological Society. Used with permission.

basins.

As alluded to in Section 1.1, there is observational evidence for a dependence of the climate state on the degree of clustering in convection (Tobin et al., 2012, 2013). Tobin et al. (2012) used several metrics of aggregation of convection on the synoptic scale, including the number of cloud clusters in a given area and the clumping of those clusters, to show that the area-averaged humidity is reduced. This was primarily because of the dryness in the non-convecting environment. They also found that when there were fewer clusters (a more aggregated state), there were enhanced surface fluxes both within and outside convecting areas. In areas with a higher degree of aggregation, the outgoing longwave radiation and reflected shortwave radiation were also reduced, primarily due to reduced deep convective cloudiness. Tobin et al. (2013) performed a similar analysis examining mesoscale convective aggregation and found consistent results, except regarding surface fluxes, which did not vary with the aggregation state.

Infrared and visible images from geostationary satellites are the primary source of data for these observation-based studies (e.g., Velasco and Fritsch, 1987; Miller and Fritsch, 1991; Laing and Fritsch, 1993a,b; Machado and Rossow, 1993; Mapes and Houze Jr., 1993; Machado et al., 1998; Tobin et al., 2012, 2013). The extensive database created by Hennon et al. (2011) used GridSat, a global, gridded, IR satellite dataset spanning 28 years. Other recent studies have used other types of satellite

data, such as rainfall data from the TRMM satellite (Futyan and Del Genio, 2007; Peters et al., 2009) , QuikScat scatterometer winds and microwave-based precipitable water estimates (Mapes et al., 2009; Tobin et al., 2012) to supplement traditional IR brightness temperature.

1.2.2 Modeling Studies

Numerous studies over the last two decades have investigated self-organization of convection in numerical models. In a two-dimensional simulation, Held et al. (1993) found a localization of convection in which convective moistening of the atmosphere made the same location favorable for future convection. Tompkins (2001b) also found that water vapor played an important role in the organization of convection in simulations with a three-dimensional channel domain. Specifically, a cluster of convection moistened its local environment while drying more distant regions, due to the different time scales associated with the moistening and drying of the atmosphere by convective activity.[4] Craig and Mack (2013) advocated that this moisture-convection feedback would inevitably produce organization on increasingly larger scales through a coarsening process. Their simple model of the tropospheric moisture budget exhibited self-organization which was qualitatively comparable to cloud-resolving model simulations, such as those by Bretherton et al. (2005). Bretherton et al. (2005) found that, in a 100-day radiative-convective equilibrium simulation with a three-dimensional cloud resolving model, convection self-aggregated into a single cluster. They interpreted this phenomenon as driven by convection-water vapor-radiation feedbacks which dry the drier air columns and moisten the moister air columns. The radiative part of the feedback is such that there is enhanced longwave cooling of the driest columns and decreased longwave cooling of the moistest columns. Other processes have also been suggested to play a role in convective organization, such as cold pools (e.g., Tompkins, 2001a) and gravity waves (e.g., Mapes, 1993; Stechmann and Majda, 2009). Self-aggregation is also observed in conditionally unstable moist Rayleigh-Bénard con-

[4]Drying is due to environmental subsidence which spreads out at the propagation speed of gravity waves, while moistening due to detrainment progresses at slower advection speeds (Tompkins, 2001b).

vection (Pauluis and Schumacher, 2011), suggesting that it is a fundamental property of moist convection.

While most of the studies of self-aggregation have been performed with no rotation, if sufficient rotation is added, the convective clusters in the aggregated state can take the form of tropical cyclones (Bretherton et al., 2005; Nolan et al., 2007; Held and Zhao, 2008; Khairoutdinov and Emanuel, 2012, 2013; Zhou et al., 2014). Bretherton et al. (2005) found that simulations with a larger Coriolis parameter aggregated more quickly into an intense tropical cyclone. Nolan et al. (2007) found that simulations initiated with random convection sometimes underwent spontaneous tropical cyclogenesis, caused by radiative-convective feedbacks that generate aggregation; the circulation associated with the self-aggregated state then intensifies and contracts into a tropical cyclone. Khairoutdinov and Emanuel (2013) studied the characteristics of RCE on an f-plane by increasing the Coriolis parameter; this allowed them to simulate multiple tropical cyclones in the same domain. They found that when the SST was increased, the intensity and size of the tropical cyclones and the spacing between them increased. Held and Zhao (2008) and Zhou et al. (2014) found qualitatively similar sensitivities in large domain simulations of rotating RCE with coarse resolution (between 25 and 220 km) and GCM column physics (including convective and cloud parameterizations). As the domain size is increased, the equilibrium state transitions from a weak tropical depression, to a single sustained storm, to a flow dominated by closely packed tropical cyclones (Zhou et al., 2014).

Held et al. (1993) and Nolan et al. (2007) noted that the localization of convection and spontaneous typical cyclogenesis, respectively, proceeded much more slowly when the SST was lowered. Similarly, it has been found that self-aggregation only occurs above a temperature threshold (Khairoutdinov and Emanuel, 2010; Wing and Emanuel, 2012). No explanation has been offered for the SST threshold of self-aggregation found in simulations. Nevertheless, it may have important consequences. For example, Khairoutdinov and Emanuel (2010) hypothesized that the temperature dependence of aggregation could lead to a self-organized critical state, in which the system is attracted to the transition between aggregated and disaggregated states.

There is some evidence that observed moist convection may exhibit self-organized critical behavior (Peters and Neelin, 2006; Muller et al., 2009; Yuan, 2011). However, aggregation in numerical models displays strong hysteresis, such that it remains aggregated even if the SST is reduced below the threshold (Khairoutdinov and Emanuel, 2010; Muller and Held, 2012).

Self-aggregation is sensitive to the domain size and horizontal resolution of the simulations, with aggregation being favored by large domains and relatively coarse resolution (Muller and Held, 2012; Jeevanjee and Romps, 2013). Regarding explanations for the domain size dependence of self-aggregation, there are conflicting results in the literature. Muller and Held (2012) explain this sensitivity by the dependence of low clouds on domain size, while Jeevanjee and Romps (2013) find that cold pools are responsible for the domain size threshold (in the absence of cold pools, self-aggregation occurs at all scales and only weakens as the domain size decreases). Jeevanjee and Romps (2013) found that in small domains, a shallow circulation that weakens aggregation dominates. Cold pools transport moisture to the dry patch boundary layer, which is followed by convection that moistens the free troposphere (Tompkins (2001a) found a similar mechanism by which cold pools trigger new convection). Jeevanjee and Romps postulate that cold pools are not able to homogenize moisture and convection in large domains because the boundary layer in the dry patch is drier and the cold pools must travel a further distance to get there. In contrast, Muller and Held (2012) argue that a shallow circulation driven by longwave cooling at the top of low clouds provides up-gradient energy transport that is important for aggregation. The role of circulation in providing up-gradient energy transport for aggregation was also highlighted by Bretherton et al. (2005). Muller and Held find that there are more low clouds in the dry regions for simulations with larger domains and/or coarser resolutions, allowing this circulation to form. It is not clear, however, why near surface relative humidity and cloudiness should increase with domain size.

Previous studies have investigated various feedback mechanisms for self-aggregation primarily by performing mechanism denial experiments in which they attempt to remove the various feedbacks by preventing certain interactions. Tompkins and Craig

(1998) found that using a wind-independent surface flux calculation destroyed the aggregation (which was characterized by an alignment of convection into a band structure) in their simulations. Bretherton et al. (2005) found that horizontally homogenizing the surface fluxes prevented self-aggregation, while Muller and Held (2012) found that it did not in all cases. Sensitivity studies performed to determine the conditions under which aggregation does or does not occur, have also indicated that if radiative heating rates are horizontally homogenized, self-aggregation does not occur (Tompkins and Craig, 1998; Bretherton et al., 2005). The importance of interactive radiation was also highlighted by Stephens et al. (2008), who found that the banded nature of convective organization in their simulations was established by gradients in radiative heating that are determined by differences in high clouds between wet and dry regions, which are in turn controlled by the convection. Muller and Held (2012) also found that radiation-cloud interactions were key by performing sensitivity experiments in which they successively turned off various mechanisms. They found that self-aggregation still occurred with homogenized surface fluxes and homogenized shortwave radiative heating, but did not occur with homogenized longwave radiative cooling. Specifically, they argued that the mechanism causing self-aggregation is the longwave radiative cooling from the top of low (liquid water) clouds in the dry regions.

1.3 Objectives of Thesis

While strides have been made identifying the physical mechanisms causing self-aggregation of convection, there has not been a systematic quantification of the various feedbacks essential to it. This study works towards closing this gap in our understanding of the physics of self-aggregation. To that end, a new analysis technique is applied to radiative-convective equilibrium simulations performed with a cloud resolving model; the details of these simulations are described in the next chapter. The overarching goal is to determine the underlying physics of self-aggregation and improve our understanding of mechanisms by which convection organizes.

Three key questions related to self-aggregation are addressed:

1. How does self-aggregation evolve?

2. What physical feedback mechanisms are important and what are their magnitudes?

3. How and why does self-aggregation depend on sea surface temperature?

Following this introductory chapter, Chapter 2 describes the evolution to a self-aggregated state, including the effect of aggregation on domain averaged quantities. In Chapter 3, the results of sensitivity tests are presented. These simulations were performed to test the robustness of self-aggregation and provide guidance as to the relevant physical mechanisms. In Chapter 4, the analysis framework for the quantification of self-aggregation feedbacks, which is a budget for the spatial variance of vertically integrated frozen moist static energy, is introduced. The results of that analysis and an explanation of the most important physical mechanisms are also discussed in Chapter 4. An overview of the mechanisms determining the temperature dependence of self-aggregation is provided; a more detailed exploration can be found in a companion paper (Emanuel et al., 2013). Chapter 5 concludes with a summary of the key findings of this work, a discussion of their implications, and suggestions for future work.

Chapter 2

Evolution of Self-Aggregation

2.1 Model Simulations

The model used is the System for Atmospheric Modeling, version 6.8.2, henceforth referred to as SAM (Khairoutdinov and Randall, 2003). SAM was used by Bretherton et al. (2005), Khairoutdinov and Emanuel (2010), Muller and Held (2012), and Wing and Emanuel (2012) for investigating self-aggregation. SAM is a three-dimensional cloud resolving model that employs the anelastic equations of motion. The prognostic thermodynamic variables are total non-precipitating water, total precipitating water, and the liquid water/ice static energy, h_L

$$h_L = c_p T + gz - L_v(q_c + q_r) - L_s(q_i + q_s + q_g), \tag{2.1}$$

where q_c is the cloud water mixing ratio, q_r is the rain mixing ratio, q_i is the cloud ice mixing ratio, q_s is the snow mixing ratio, q_g is the graupel mixing ratio, L_v is the latent heat of evaporation, and L_s is the latent heat of sublimation. The total non-precipitating water mixing ratio is the sum of the mixing ratios of water vapor,

[1] Section 2.1, portions of Sections 2.2 -2.3, Figure 2-1, Figures 2-9 and 2-10, and Table 2.1 were published as part of Wing and Emanuel (2013), in the *Journal of Advances in Modeling Earth Systems*. The published version of the text and figures have been adapted with a few additions for clarification, in accordance with the Creative Commons Attribution License.

cloud water, and cloud ice, while the total precipitating water mixing ratio is the sum of the mixing ratios of rain, snow, and graupel. The diagnosed cloud condensate and total precipitating water are partitioned into hydrometeor mixing ratios at every time step as a function of temperature. The subgrid-scale fluxes are computed using a Smagorinsky-type parameterization, as in Bretherton et al. (2005) and Muller and Held (2012). As in previous studies of self-aggregation with SAM, we use the 1-moment microphysics package. Further details about the model can be found in Khairoutdinov and Randall (2003).

Longwave and shortwave radiative fluxes are computed using the RRTM radiation scheme (Mlawer et al., 1997; Clough et al., 2005; Iacono et al., 2008) in which the radiative transfer is computed at each individual grid column using the instantaneous model temperature, water vapor, and cloud fields. The solar constant is set to 650.83 W/m^2 with a zenith angle of 50.5 degrees (following Bretherton et al. (2005)), resulting in a constant solar insolation of 413.98 W/m^2; there is no diurnal cycle. The surface sensible and latent heat fluxes are computed interactively, using an iterative procedure to compute the exchange coefficients. A minimum wind speed of 1 m/s is used to calculate the surface fluxes. The simulations discussed here are performed with a domain size of 768 $\times$ 768 km^2 with 64 vertical levels and rigid lid at 28 km, unless otherwise indicated. A doubly periodic lateral boundary condition is employed. The model grid is a fully staggered Arakawa C-type grid with a uniform horizontal resolution of 3 km and a stretched vertical grid. The lowest model level is at 37 m and the grid spacing is 75 m near the surface, increasing to 500 m above 3.5 km. Newtonian damping is applied to all prognostic variables in a sponge layer covering the upper third of the model domain to reduce gravity wave reflection and build-up. A standard simulation is run for 100 days, with a variable time step of 12 s or less (to satisfy the CFL condition). The model is initialized with a sounding from the domain average of a simulation of radiative-convective equilibrium on a 96 $\times$ 96 km^2 domain at the same sea surface temperature. There is no mean wind, no rotation, and no external forcing imposed. Motion is initialized by adding white noise to the initial h_L field at the five lowest grid levels, with an amplitude that is 0.1 K

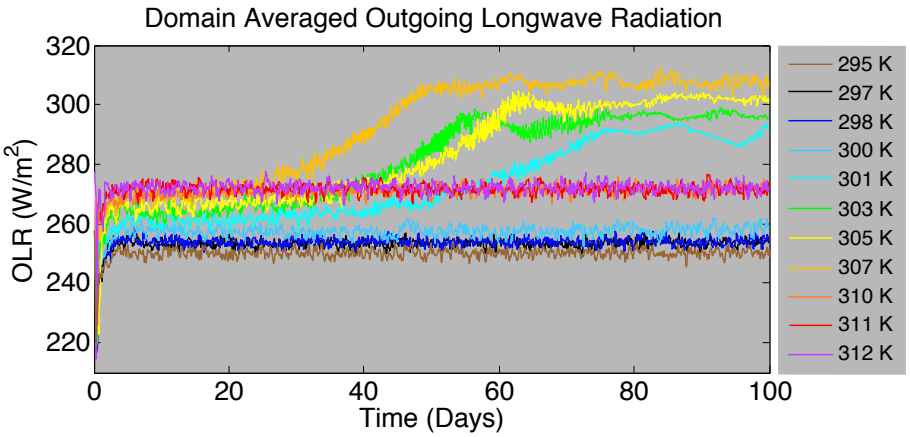

Figure 2-1: Evolution of the domain averaged outgoing longwave radiation (OLR). Each curve is a simulation performed at a different fixed SST. The data are hourly averages. The non monotonic dependence on SST is an artifact of limited domain size.

at the lowest model level and decreases linearly to 0.02 K at the fifth model level. The simulations are performed at fixed sea surface temperature (SST), with values between 295 K and 312 K; but most of the results shown in this thesis are for the 305 K case.

2.2 Evolution of Domain-Averaged Quantities

2.2.1 Radiative Fluxes and Moisture

We first compare the evolution of domain averaged outgoing longwave radiation (OLR) in each of the simulations performed at different values of SST (Figure 2-1). The simulations are identical except for the SST (and its corresponding initial sounding). An obvious feature in some of the simulations is a dramatic increase in the OLR, which marks the transition to self-aggregation. OLR increases when convection is aggregated because the domain mean free troposphere is significantly drier when convection is aggregated. Simulations at SST values of 301 K, 303 K , 305 K and 307 K self-aggregate between 50 and 70 days; simulations at colder and higher values of SST do not aggregate during the period of integration (Figure 2-1, Table

Table 2.1: Summary of domain average statistics at different fixed SSTs. OLR is outgoing longwave radiation, CRH is column relative humidity. The "i" subscript indicates an average from day 10 to 20, while the "f" subscript indicates an average from day 85 to 100. All quantities are horizontal means.

SST	Self-Aggregates?	OLR_i (W/m^2)	OLR_f (W/m^2)	CRH_i	CRH_f
295 K	No	248.68	248.60	0.6942	0.6936
297 K	No	253.37	253.54	0.6978	0.6961
298 K	No	253.93	253.86	0.7047	0.7018
300 K	No	257.38	258.36	0.7111	0.6964
301 K	Yes (circular)	259.90	286.57	0.6981	0.4102
303 K	Yes (band)	264.18	296.22	0.7064	0.3345
305 K	Yes (circular)	266.46	302.30	0.7165	0.3195
307 K	Yes (band-circular)	270.75	307.69	0.7073	0.3124
310 K	No	269.92	271.92	0.7582	0.7435
311 K	No	272.10	271.64	0.7521	0.7503
312 K	No	272.18	272.09	0.7528	0.7507

2.1). Table 2.1 provides additional information about the simulations shown in Figure 2-1. The table indicates, for each SST, a representative initial and final value for two domain average indicators of self aggregation: OLR and column relative humidity (CRH). The four simulations that self-aggregated all feature an increase of more than 30 W/m^2 in the OLR between the initial and final periods. There is a corresponding large decrease in the CRH.

Based on previous work (Khairoutdinov and Emanuel, 2010), we expected that self-aggregation would not occur at the coldest SST's (295 K - 300 K), but it is surprising that self-aggregation does not occur at the highest SST's (310 K - 312 K). Experiments extending the 310 K and 312 K runs by 40 days still fail to aggregate. The apparent non-monotonicity of self-aggregation with respect to SST turns out to be an artifact of limited domain size. Indeed, when the 310 K simulation was rerun with a domain size of 1536 x 1536 km^2 in the horizontal (four times the area of the original domain), self-aggregation occurred. The relationship between domain size and temperature will be discussed in more detail in Chapter 3. In this set of simulations, the critical SST necessary for self-aggregation is near 300 K; the mechanism behind this threshold will be explored in Chapter 4.

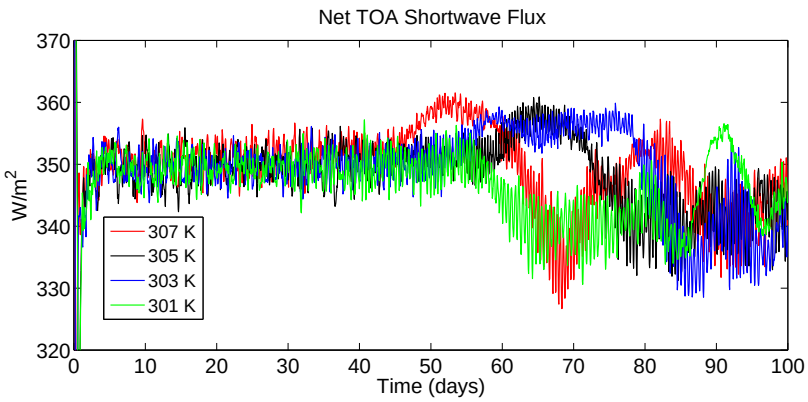

Figure 2-2: Evolution of domain averaged net top of atmosphere (TOA) shortwave radiative flux (W/m^2), for simulations at different SSTs. This flux is downward.

Tobin et al. (2013) found that the observed OLR was increased by 20 - 30 W/m^2 in more aggregated regimes, which is comparable to the increases in our simulations. However, they found that this effect was canceled by reduced reflected shortwave radiation at the top of the atmosphere (TOA), such that the net TOA radiative flux remained approximately the same. This is not the case in our simulations. The net TOA shortwave radiative flux, which is downward, decreases slightly with aggregation (Figure 2-2). The TOA downward shortwave flux is fixed (constant solar insolation), but the TOA upward shortwave flux increases. This change is of the wrong sign to offset the OLR changes, and is not nearly as large a magnitude. As a result, the net TOA radiative flux, which is downward, decreases in magnitude (becomes less negative) (Figure 2-3a). This disagreement with observations results from differences in the how cloud fraction changes with aggregation, which determines albedo. In our simulations, the cloud fraction increases with aggregation. For example, in the 305 K simulation, the high cloud fraction remained approximately constant, the middle cloud fraction decreased slightly from 0.07 to 0.03, but the low cloud fraction increased from 0.12 to 0.20. This is in contrast to the results of Tobin et al. (2013), who found a decrease in deep, middle, and shallow clouds in the environment under more aggregated conditions. While all the middle and high clouds are confined to the cluster in our simulations, there are low clouds that extend out from the cluster into the drier regions. It is these low clouds that are responsible for the small increase in

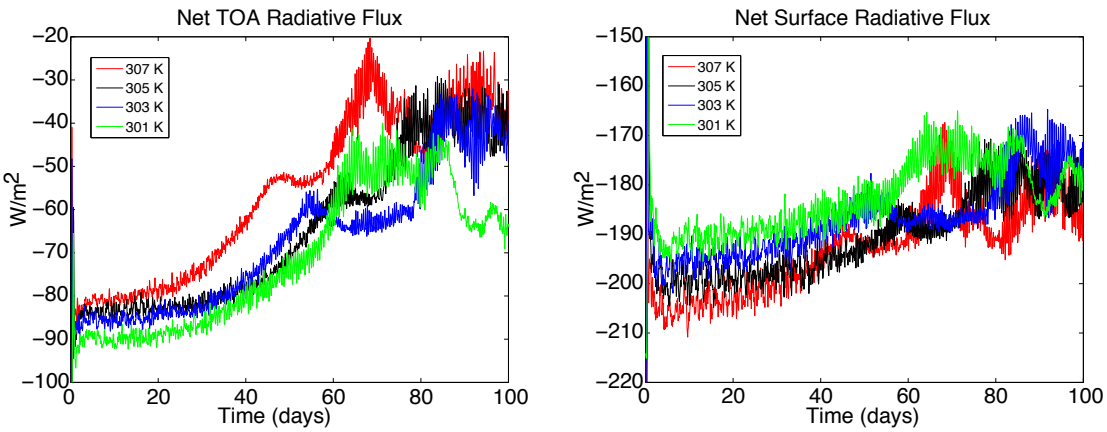

(a) TOA (b) Surface

Figure 2-3: Evolution of domain averaged net top of atmosphere (TOA) radiative flux (a) and net surface radiative flux (b), in W/m^2. A negative sign indicates a downward flux.

the TOA upward shortwave flux.

In addition to the changes in the TOA radiative fluxes with aggregation, there are dramatic changes in the domain averaged net surface radiative fluxes. The domain average net surface longwave flux increases with aggregation (Figure 2-4b). That is, the surface loses more energy to longwave radiation when the convection is aggregated. This is because the domain average downward longwave flux at the surface decreases, since the domain average is drier, while the upward longwave flux at the surface is fixed (constant SST). Tobin et al. (2013), on the other hand, found that the net longwave flux at the surface did not change with the degree of aggregation. The domain average net surface shortwave flux, which is downward, increases as the system evolves toward aggregation. However, for most of the simulations, it then decreases to near its original value (Figure 2-4a). As was the case with the TOA radiative fluxes, the change in the longwave fluxes dominates and the overall net surface radiative flux decreases in magnitude with aggregation (Figure 2-3b). The net surface radiative flux becomes less negative, thus, the surface gains less energy (in the domain mean). This disagrees with the results of Tobin et al. (2013), who found that the surface gained more energy when convection was more aggregated in observations. We speculate that the lack of agreement between our results and those of Tobin et al. (2013) stems from the cloud

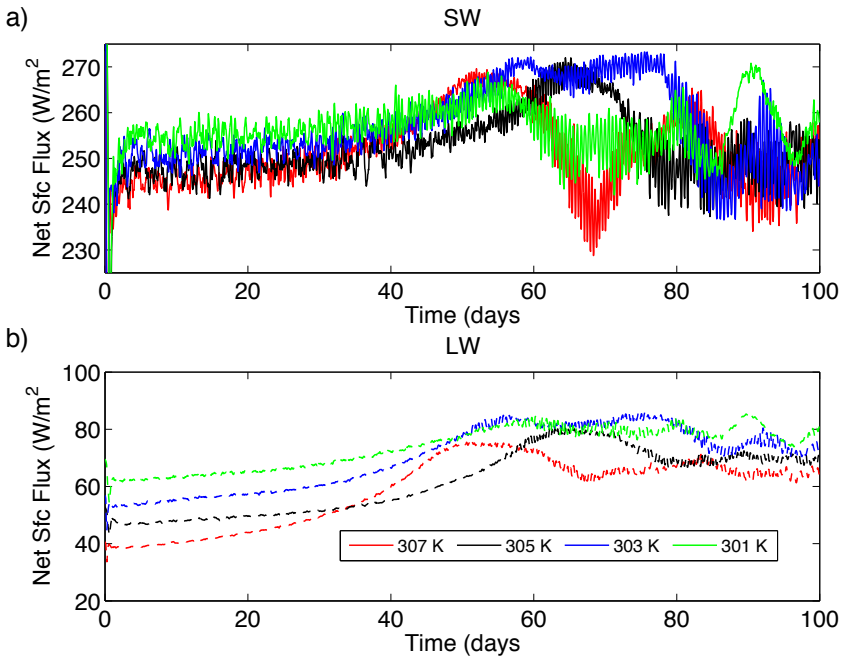

Figure 2-4: Evolution of domain average net surface shortwave (a) and longwave (b) fluxes (W/m^2), for simulations at different SSTs. Both are plotted as positive quants, but the net surface shortwave flux is downward while the net surface longwave flux is upward.

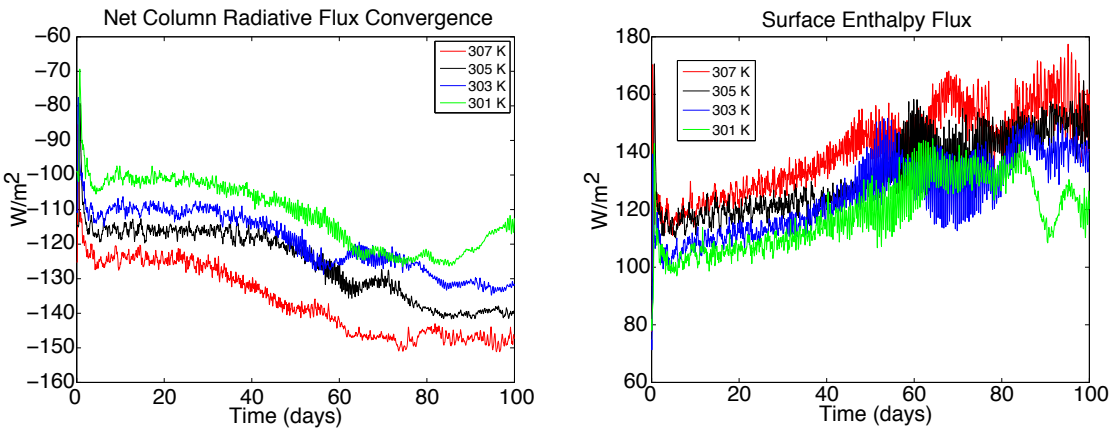

(a) NetRad (b) Surface Enthalpy Flux

Figure 2-5: Evolution of domain averaged net column radiative flux convergence (a) and surface enthalpy flux (b), in W/m^2, for simulations at different SSTs. A negative NetRad indicates the atmosphere is losing energy.

changes discussed above, as well as the fact that the sea surface temperature is fixed in our simulations, whereas in observations, it is free to evolve.

While Tobin et al. (2013) found that the TOA energy budget was not significantly affected by the degree of aggregation in observations of convection, they did note that there was a vertical redistribution of energy such that there was enhanced tropospheric radiative cooling. We calculate the net column radiative flux convergence according to Equation (2.2):

$$\text{NetRad} = \text{LW}_{\text{sfc}} - \text{LW}_{\text{TOA}} + \text{SW}_{\text{TOA}} - \text{SW}_{\text{sfc}}. \tag{2.2}$$

The longwave fluxes are defined to be positive upwards while the shortwave fluxes are defined to be positive downwards. We find that the domain averaged net column radiative flux convergence becomes more negative (Figure 2-5a). The atmosphere loses more energy when convection is aggregated, which is consistent with Tobin et al. (2013).

Finally, we examine the evolution of the domain average surface enthalpy fluxes. Since our simulations employ a fixed SST, the surface enthalpy fluxes only depend on the surface wind speed, the near-surface air temperature, and the near-surface water vapor mixing ratio. In the simulations that aggregate, the domain average

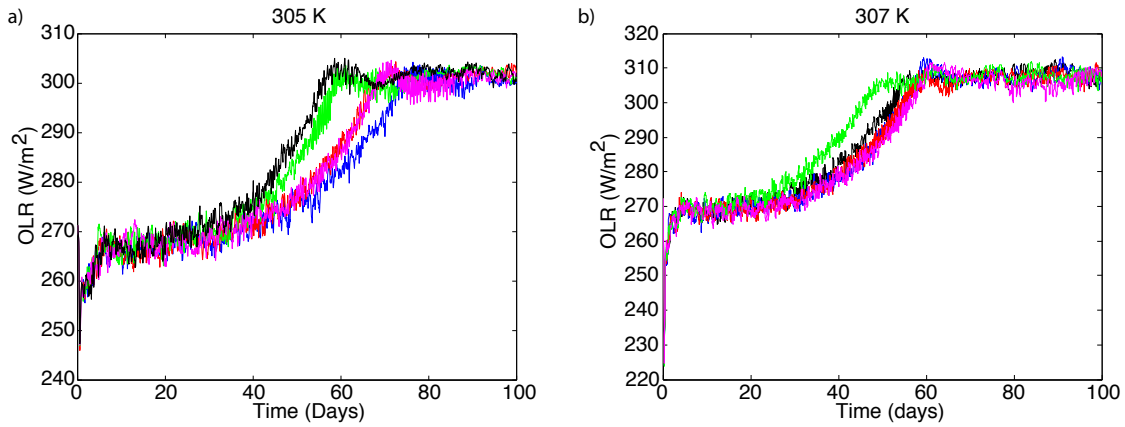

Figure 2-6: Domain average outgoing longwave radiation (OLR) for simulations in which the random noise used to initialize the model is varied, at 305 K (a) and 307 K (b). There are 5 ensemble members for each SST.

surface enthalpy fluxes increase with time (Figure 2-5b). This increase in surface flux with aggregation is also found in synoptic-scale observations by Tobin et al. (2012), who noted that surface fluxes were enhanced both within and outside convecting areas. Tobin et al. (2013), however, did not find any change in surface fluxes in their analysis of mesoscale convective aggregation. We speculate that the domain average surface fluxes increase with aggregation because the domain mean is dominated by the non-convecting area. Outside the convecting area, the boundary layer water vapor decreases, which increases the air-sea enthalpy disequilibrium and therefore the surface fluxes. We investigate the response of the surface enthalpy fluxes to aggregation in more detail in subsequent sections.

2.2.2 Time Scale of Aggregation

The time to aggregation, as approximated by when the domain average OLR stops increasing, does not vary monotonically with SST (Figure 2-1). This indicates a possibly large stochastic component of self-aggregation. Sensitivity tests in which, for a given SST, we vary the random noise used to initialize the simulations seem to confirm the stochastic nature of self-aggregation, with the time to aggregation varying by about twenty days (Figure 2-6). The location of the cluster and its spatial orientation (i.e. whether it is an elongated band or a circular cluster) also vary with

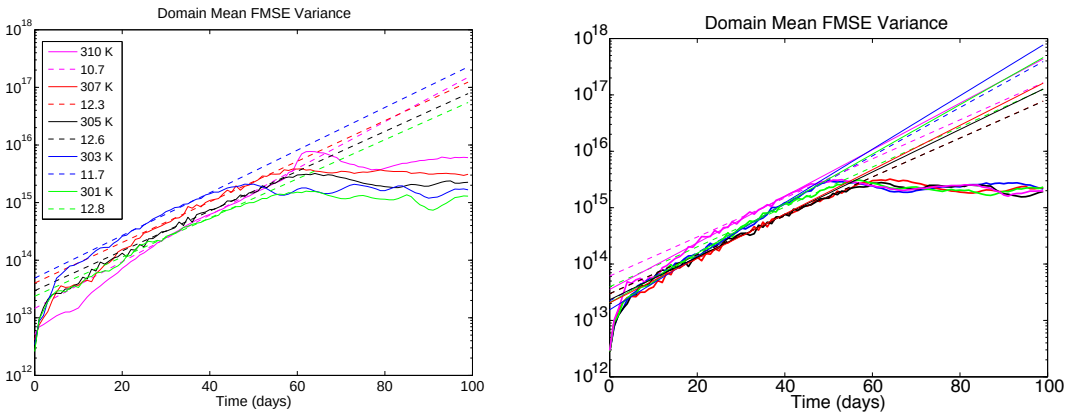

(a) Simulations at different SSTs. (b) Ensemble of simulations at 305 K.

Figure 2-7: Evolution of domain mean spatial variance of vertically integrated frozen moist static energy (FMSE) (J^2/m^4). The y-axis is on a logarithmic scale. (a) shows results from simulations at different SSTs (solid lines). Exponential fit with the coefficients given in Table 2.3 is shown in dashed lines, legend indicates e-folding time. (b) shows results from an ensemble of simulations at 305 K (bold solid lines). Exponential fit with the coefficients given in Table 2.3 is plotted in thin lines. The thin solid lines are a fit based on data from Day 1 - 40, while the thin dashed lines are a fit based on data from Day 2-50.

the initial random noise. In some of the simulations, the convection aggregates into an elongated band and stays in this state for 10s of days before collapsing further into a circular cluster. The evolution to aggregation is always characterized by the expansion of a dry patch (as we will examine in the next section), although there are sometimes several dry patches that then merge. The type of cluster obtained in the simulations that self-aggregate is indicated in Table 2.1.

Another signature of self-aggregation is an increase in the domain average of the spatial variance of vertically integrated frozen moist static energy (FMSE). In Chapter 4, we construct a budget for the spatial variance of the vertically integrated FMSE in order to quantify feedback mechanisms. Here, we simply use this quantity to characterize the time scale of aggregation. When plotted on a logarithmic scale, it is evident that the increase in the FMSE variance is exponential during the evolution to aggregation before reaching a quasi-steady state (Figure 2-7). By eye, the rate of increase appears to be similar between the simulations at different values of SST (Figure 2-7a). To confirm this, we fit a simple exponential (Equation (2.3)) over the

Table 2.2: Exponential fit of domain average FMSE variance for simulations at different SSTs. Day_i is the range of days used for the start of the fit, Day_f is the range of days used for the end of the fit. The amplitude (a) and exponent (b), and the r^2 value for the fit using those coefficients, are given from the calculation using the first day in each range for Day_i and Day_f. τ indicates the time scale calculated from the exponent coefficient ($1/b$).

SST	Day_i	Day_f	a_1 ($10^{13}\,J^2/m^4$)	b_1 (days^{-1})	τ_1 (days)	r^2
301 K	2:7	45:55	2.3697	0.0782	12.79	0.9933
303 K	2:7	50:50	4.8805	0.0853	11.73	0.9933
305 K	2:7	50:60	2.9572	0.0796	12.57	0.9917
307 K	3:8	50:60	4.0099	0.0811	12.33	0.9863
310 K	1:6	45:55	1.4535	0.0933	10.72	0.9938

first half of the simulation (shown by the dashed lines in Figure 2-7a):

$$f(t) = ae^{bt}. \tag{2.3}$$

The range of days used in the fit and the coefficients obtained are given in Table 2.2. All the simulations included in Figure 2-7 and Table 2.2 have a horizontal domain size of 768 x 768 km^2, except the one at 310 K, which has a horizontal domain size of 1536 x 1536 km^2. For the four simulations with a 768 x 768 km^2 domain size, the exponent for each curve is near 0.08 days^{-1}, which corresponds to a timescale (τ) of 12.5 days. This is roughly consistent with the 9 day time scale of aggregation calculated by Bretherton et al. (2005). There is some variation in this time scale with SST, but it is not systematic. The r^2 values indicate that the exponential fit is quite good. However, we find that the value of the exponent, b, is sensitive to the precise range of days used in the exponential fit. Figure 2-8 shows b as a function of the choice of initial and final day for the fit (Table 2.2). The value of the exponent coefficient varies more strongly with the choice of the final day of the fit than with the choice of initial day. Notably, the variation in the exponent coefficient in Figure 2-8 is larger than its variation with SST. For example, the exponent coefficient for the 303 K simulation varies between 0.065 and 0.084 days^{-1}, which corresponds to a time scale between 15.28 days and 11.90 days. Similarly, the time scale varies from

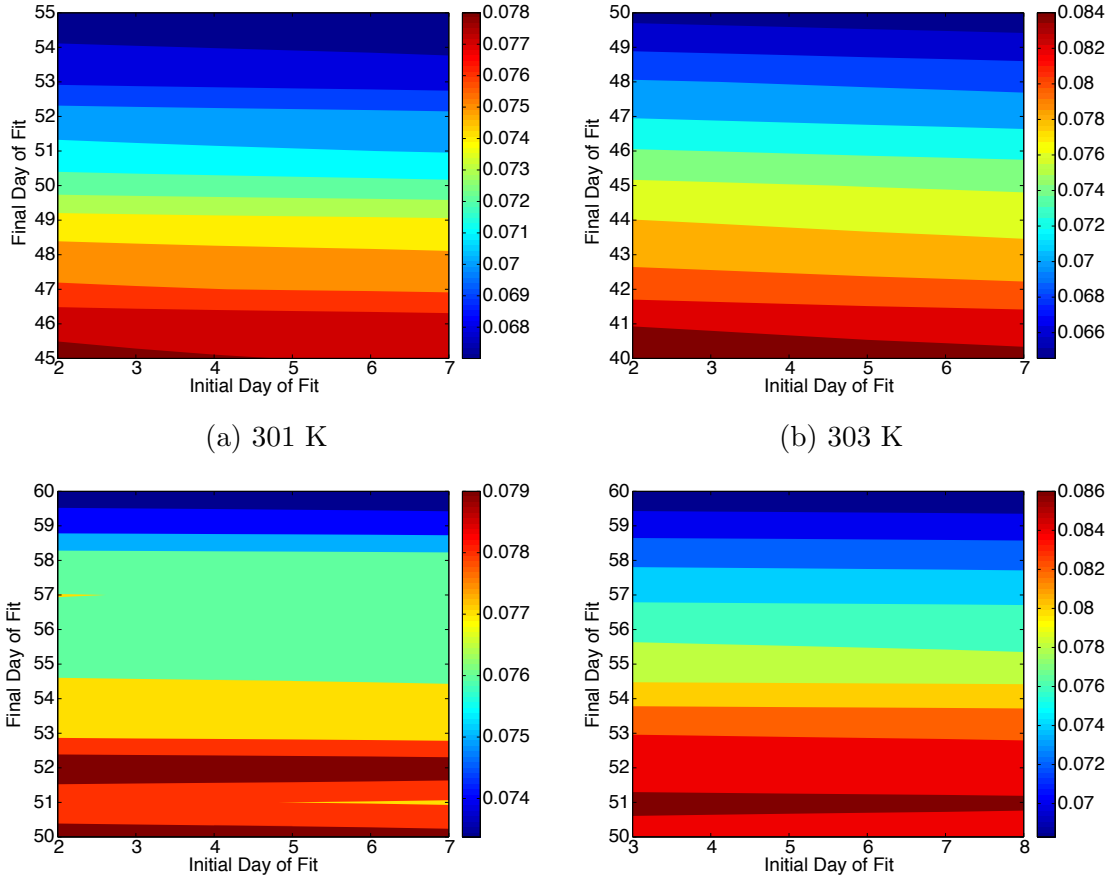

(a) 301 K (b) 303 K

(c) 305 K (d) 307 K

Figure 2-8: Exponent coefficient, b (days^{-1}), as a function of the initial and final days used in the fit of the domain average spatial variance of FMSE.

14.93 days to 12.82 days for the 301 K simulation, 13.42 days to 12.66 days for the 305 K simulation, and 14.71 to 11.62 days for the 307 K simulation. In addition to this sensitivity to the range of data used in the fit, the slope of the exponential also varies when we vary the random noise used to initialize the simulation. We fit a simple exponential to each of the ensemble members shown in Figure 2-6a. The variation in the exponential fit between ensemble members at a given SST is as large, if not larger, than the variation between simulations at different SSTs (Figure 2-7b, Table 2.3). This again highlights the stochastic component of self-aggregation and suggests that the differences in time scale to aggregation at different SSTs are not meaningful. Indeed, without the labels in Figure 2-7, it would be difficult to tell which panel featured simulations at different SSTs (Figure 2-7a) and which featured

Table 2.3: Exponential fit of domain average FMSE variance for ensemble of simulations at 305 K. The exponent of the fit is computed using two ranges of data: days 2:50 (b_1) and days 1:40 (b_2). τ indicates the time scale calculated from the exponent coefficient ($1/b$).

Ensemble Member	b_1 $\left(\text{days}^{-1}\right)$	τ_1 (days)	b_2 $\left(\text{days}^{-1}\right)$	τ_2 (days)
1	0.0796	12.56	0.0906	11.04
2	0.0986	10.14	0.1093	9.15
3	0.0797	12.55	0.0952	10.50
4	0.0793	12.61	0.0869	11.51
5	0.0815	12.17	0.1012	9.88

an ensemble of simulations at the same SST (Figure 2-7b).

The large domain (1536 x 1536 km^2) simulation at 310 K (pink curve in Figure 2-7a) has a rate of aggregation that is somewhat faster than in the smaller domain, lower SST simulations. The e-folding time of domain mean FMSE variance in the 310 K simulation is 10.72 days, while the e-folding times of the other simulations are near 12 days. This result points out the limitations of domain size. One might expect a faster approach to aggregation at higher temperatures, but as SST is increased, it is increasingly difficult for the cluster to fit in the prescribed domain (further discussed in Chapter 3). This might decrease the rate of aggregation as SST is increased with a fixed domain size. These two competing effects may explain why the time to aggregation does not vary systematically with SST in the 301 - 307 K simulations. The factors that set the scale of the cluster and therefore the necessary domain size for aggregation remain unknown.

Finally, we note that an exponential fit of the spatial variance of precipitable water compares well with that of the FMSE variance. Precipitable water is easier to obtain from observations than vertically integrated FMSE, so examining its spatial variance may be a way to diagnose and characterize the degree of aggregation in observations.

2.3 Development and Expansion of Dry Patch

In simulations in which self-aggregation occurs, the domain averaged OLR gradually increases over the first 50 to 70 days of the simulation (Figure 2-1). To further explore

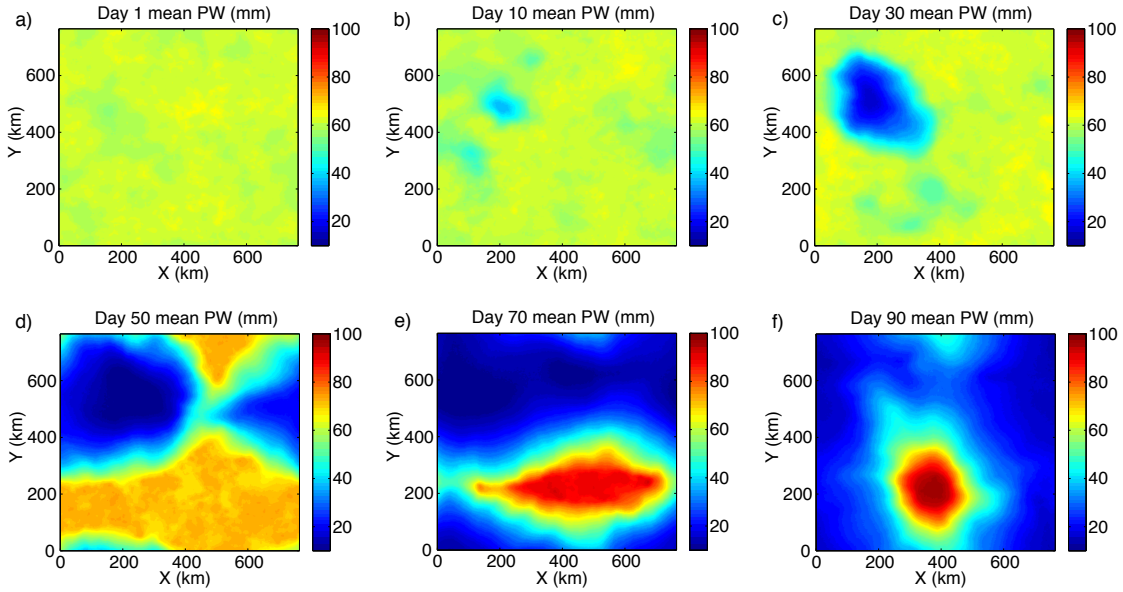

Figure 2-9: Daily average precipitable water (PW, in mm) for days 1 (panel a), 10 (panel b), 30 (panel c), 50 (panel d), 70 (panel e), and 90 (panel f). The data are from a simulation at 305 K.

what happens as self-aggregation evolves, we examine the simulation at 305 K as a case study. This temperature is firmly above the threshold for aggregation in our set of simulations but is not so warm that aggregation requires a larger domain. Plan views of daily mean precipitable water (PW) throughout the simulation at 305 K are shown in Figure 2-9.

The day 1 average precipitable water (PW) field in the 305 K simulation is fairly homogeneous (Figure 2-9a). By day 10 (Figure 2-9b), a small area near X = 200 km and Y = 500 km has become drier than the rest of the domain. Over the next 20 days, the small dry patch amplifies and expands and by day 30 (Figure 2-9c) it covers nearly a quarter of the domain. This process continues, and at day 50 (Figure 2-9d) the areas of the domain not in the dry patch have become moister than they were initially. At day 70 (Figure 2-9e), the expanding dry region has confined all the moist air (which is now much moister than anywhere earlier in the simulation) to one band. This band evolves into a single circular cluster in which high PW values are concentrated, as seen at day 90 (Figure 2-9f). Outside the moist cluster, the rest

of the domain has very low values of PW. These results show that self-aggregation begins as a dry patch that expands. Convection is suppressed in the dry patch and becomes increasingly localized into a single cluster. Our goal is to understand the feedback mechanisms that allow the dry patch to amplify and expand.

We further characterize the development of the dry patch by examining height-time cross sections of quantities averaged over the area in the domain that is the driest at day 10 (in the 305 K simulation). Figure 2-10 displays the relative humidity anomaly from the initial relative humidity and indicates that the upper troposphere dries out first. These anomalies are calculated as the difference between the current relative humidity in the dry patch and the initial relative humidity profile. By day 5, some degree of drying has occurred throughout the entire troposphere. Over the first thirty days of the simulation, this particular area in the domain continues to dry out (we only plot the first thirty days to focus on the initial development of the dry patch). By day thirty, the relative humidity through out the lower 10 km of the free troposphere is 20% of what it was initially. We also note that, although the largest magnitude of the relative humidity decrease is in the free troposphere, the boundary layer (lowest 1 km) also experiences drying.

Associated with the decrease in humidity, convection in the dry patch quickly shuts down. As a proxy for convective activity, we examine the mixing ratios of cloud condensate and precipitating water in the dry patch. Most of the clouds and precipitation dissipate by day 5 (Figure 2-11), and by day 10 the cloud condensate mixing ratio is zero at all levels. This leads us to speculate that cloud feedbacks are not important for the amplification and expansion of the dry patch, for the simple reason that the dry patch is very quickly devoid of clouds. We also note that persistent subsidence throughout the troposphere develops in the dry patch around day 5 (not shown). The combination of the subsidence and the decrease in humidity act to prevent convection from re-developing. As will be described in Chapter 4, as the dry patch forms, the radiative heating rates change in such a way as to amplify the drying. The co-evolution of humidity, convection, subsidence, and radiative heating in the dry patch hint at the nature of self-aggregation. As will be shown in the

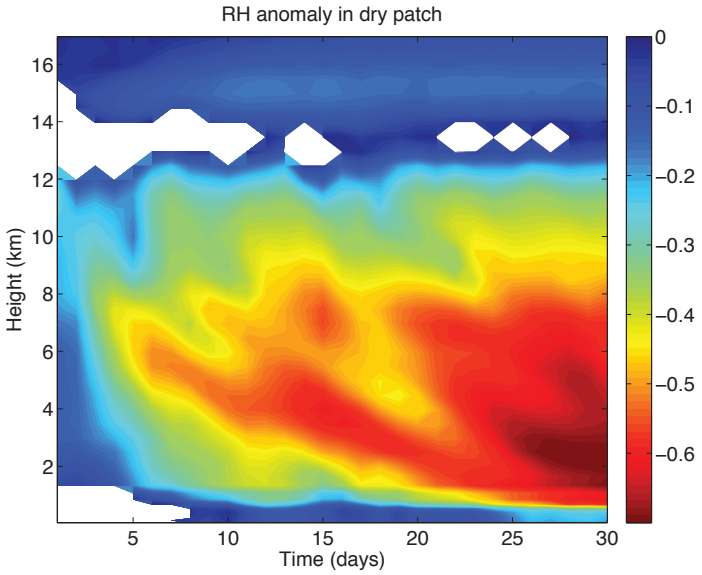

Figure 2-10: Height-time cross section of the relative humidity anomaly from the initial relative humidity profile over the first thirty days of the simulation at 305 K. The relative humidity anomaly plotted is from an average over the 48 $\times$ 48 km^2 block that is the driest (according to column relative humidity) at day 10. White shading indicates positive values.

subsequent sections and chapters, it truly depends on the interplay of radiation, convection, moisture, and circulation.

2.4 Moisture Sorted Fields

2.4.1 Moisture Sorting Procedure

Self-aggregation is characterized by an increasing gradient between the moist and dry regions. Therefore, we employ a moisture-sorting procedure, following Bretherton et al. (2005), in our analysis. For each variable we examine, we take a daily average, and then a horizontal average over 48 x 48 km^2 blocks to focus on the mesoscale organization. An example of a daily and block averaged field is shown in Figure 2-12a, where the cloud cluster is easily identifiable as the region of high column relative humidity. Here, column relative humidity (CRH) is defined as the precipitable water

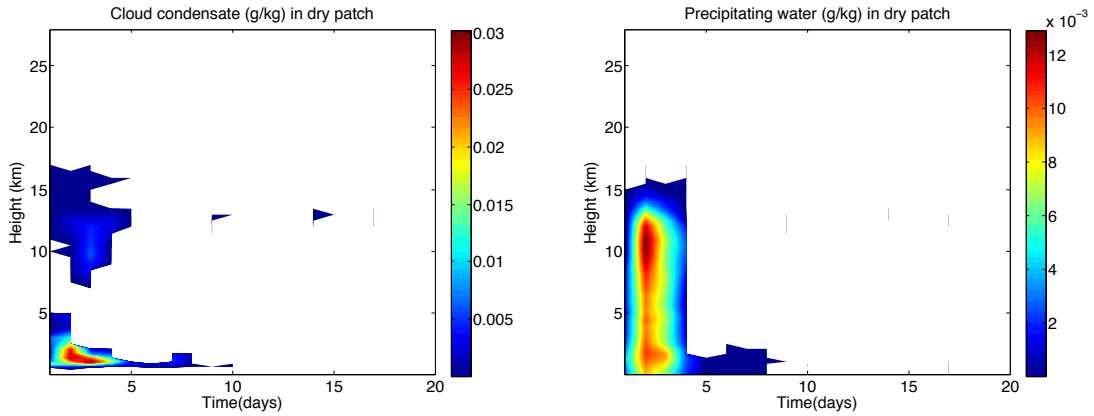

(a) q_n (b) q_p

Figure 2-11: Height-time cross section of cloud condensate q_n (a) and precipitating water q_p (b) over the first thirty days of the simulation at 305 K. q_n and q_p are averaged over the 48 $\times$ 48 km^2 block that is the driest (according to column relative humidity) at day 10. White shading indicates a value of 0

(PW) divided by the saturated water vapor path (SWP).[2] We then sort the blocks according to their column relative humidity, from driest to moistest (Figure 2-12b). The lowest ranks represent the driest blocks. We recalculate the sorting function every day, so the CRH of any given block, and the ordering of the blocks, may change in time. Once we have calculated the sorting function, we can apply it to other fields, such as the daily averaged vertical velocity, temperature, water vapor mixing ratio, and radiative heating rates. When there is a mature cluster, moisture space is analogous to actual distance from the center of the cluster. Using moisture sorting enables an examination of contrasts between dry and moist regions at all times, not just when there is a mature cluster.

There are several features of note in Figure 2-12b, which shows the actual CRH values corresponding to ranks at each time. Initially, there is not much gradient in CRH between the driest block and the moistest block; this gradient increases with time. As expected, the lowest ranked columns get drier, while the highest ranks get moister (a new "dry get drier, moist get moister" paradigm). The moist columns (higher ranks) do not get moister until the second half of the simulation, however.

[2] PW $= \int_0^{z_{top}} q_v \rho_{air} / \rho_{H_2O_{(l)}} dz$ and SWP $= \int_0^{z_{top}} q^* \rho_{air} / \rho_{H_2O_{(l)}} dz$, where q^* is the saturation water vapor mixing ratio.

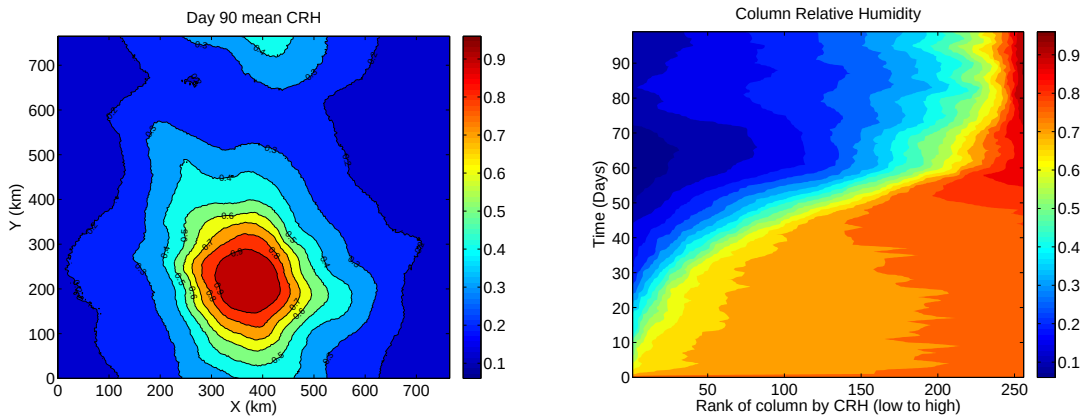

(a) Day 90 (b) Sorted CRH

Figure 2-12: Block averaged daily mean column relative humidity (CRH) for simulation at 305 K.

This reinforces our characterization of self-aggregation as a dry patch that amplifies and expands.

2.4.2 Streamfunction and FMSE

We calculate a streamfunction using the CRH-sorted vertical velocity by integrating from the dry to moist columns (following Bretherton et al. (2005)):

$$\psi_i(z) = \psi_{i-1}(z) + \Sigma_i \rho(z) w_{i-1}(z). \tag{2.4}$$

The streamfunction represents the vertical mass flux accumulated over the i driest columns. Negative values represent circulations in a counterclockwise sense, positive values represent circulations in a clockwise sense. In addition, we sort the block-averaged frozen moist static energy and cloud condensates by column relative humidity, and display those fields, along with the streamfunction, as a function of height and moisture space. The frozen moist static energy is given by

$$h = c_p T + gz + L_v q_v - L_f q_{ice}, \tag{2.5}$$

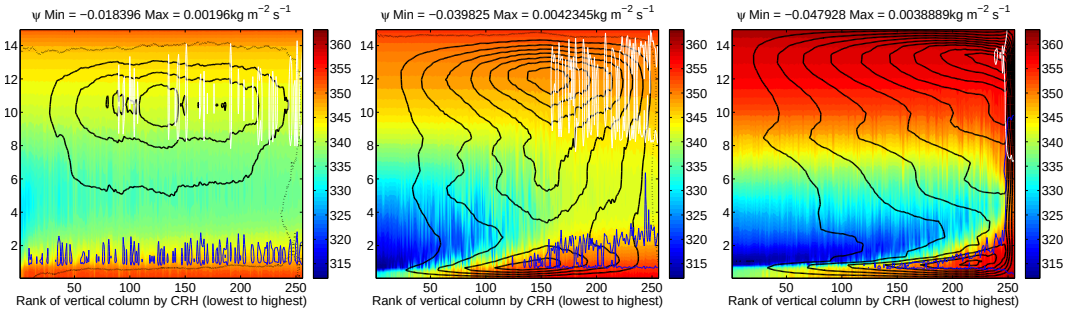

(a) Day 10 (b) Day 50 (c) Day 80

Figure 2-13: Frozen moist static energy ($kJ\,kg^{-1}$, shading), negative values of the streamfunction ($kg\,m^{-2}\,s^{-1}$, solid black contours), positive values of the streamfunction ($kg\,m^{-2}\,s^{-1}$, dotted black contours), 0.01 g/kg ice cloud condensate contour (white contours), and 0.01 g/kg liquid cloud condensate contour (blue contours). All quantities are averaged over each day and over 48 x 48 km^2 blocks, from the simulation at 305 K. On the x-axis, dry regions are on the left and moist regions are on the right.

where L_f is the latent heat of fusion, q_v is the water vapor mixing ratio, and q_{ice} represents all ice phase condensates. It is exactly conserved by the model's governing equations following moist adiabatic displacements. The moisture sorted streamfunction for the simulation at 305 K is shown in Figure 2-13. Again, these plots should be interpreted as going from dry areas (on the left) to moist areas (on the right), and all fields are daily averages. At day 10, the frozen moist static energy is fairly homogeneous and there are clouds throughout the domain. There is a counterclockwise circulation, indicated by the streamfunction, in the mid to upper troposphere. By day 50, the circulation has strengthened and extended to the surface, with a secondary circulation in the low levels. The circulation transports frozen moist static energy up gradient from the dry to moist regions (consistent with previous studies, and will be discussed in more detail in Chapter 4). In concert with this, the gradient of frozen moist static energy between the dry and moist regions has strengthened, including at the lowest levels. At day 80, the cluster is mature with the ascent and clouds confined to the moistest regions and a strong gradient in frozen moist static energy between the moist and dry regions. In simulations that do not aggregate (not shown), a circulation in the middle-upper troposphere may develop, but it never extends all

the way to the surface and there is no development of a frozen moist static energy gradient that enables the circulation to persist and self-amplify.

2.4.3 Temperature and Humidity

We briefly examine the temperature and humidity distribution at day 90 of the 305 K simulation, (a time at which there is a mature cluster), sorted according to CRH. The temperature does not vary much in the free troposphere (not shown) between moist and dry regions. It is, however, cooler in the boundary layer in the moist convecting regions, which is associated with downdraft-driven cold pools. Despite this, the virtual temperature is actual higher in the boundary layer in the moist region (Figure 2-14a), due to the large positive moisture anomalies there. Elsewhere, the virtual temperature is less than the domain mean, again reflecting moisture anomalies. The moisture anomalies are shown in Figure 2-14b, for the simulation at 305 K. There is a massive drying of the dry regions and moistening of the moist regions. The largest anomalies are in the lower troposphere, although the very moistest columns are quite a bit moister throughout a substantial portion of the column. These are huge anomalies, with the dry regions losing nearly all their water vapor (anomalies of -15 g/kg). The development of these moisture anomalies suggests a role for the moisture-convection feedback; since moist regions favor convection and convection causes local moistening, it is a positive feedback that would favor self-aggregation.

2.4.4 Radiative Heating

One of the mechanisms often proposed as important for self-aggregation is a radiative feedback. We address this more fully in Chapter 4, but briefly examine the moisture-sorted radiative heating rates here. Figure 2-15 shows an example of how radiative heating rates vary between moist and dry regions during the intermediate stage of aggregation (day 50 in the simulation at 305 K). The vertically averaged radiative heating rate is smaller in magnitude (less cooling) in the moist regions than in the dry regions (bottom panel of Figure 2-15a). Shortwave heating is enhanced in the

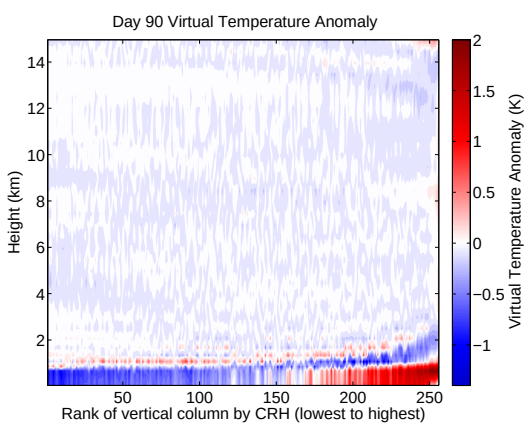

(a) T_v anomaly from domain mean.

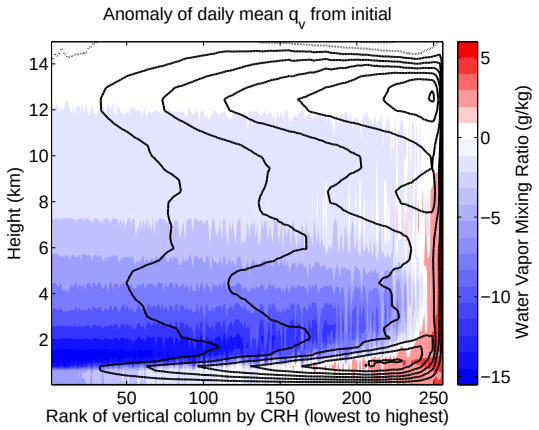

(b) q_v anomaly from initial (shading). Contours are moisture-sorted stream function.

Figure 2-14: Day 90 mean virtual temperature anomaly anomaly from domain mean (a) and water vapor mixing ratio anomaly from initial (b), from simulation at 305 K.

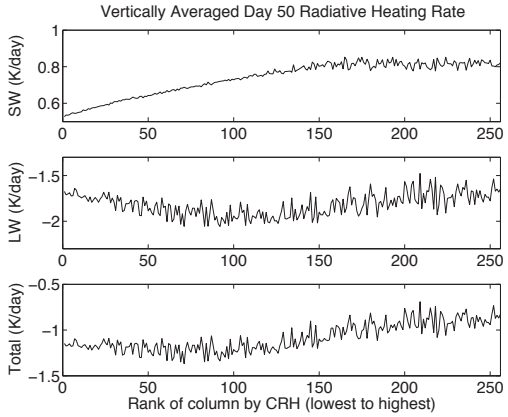

(a) Vertically Averaged

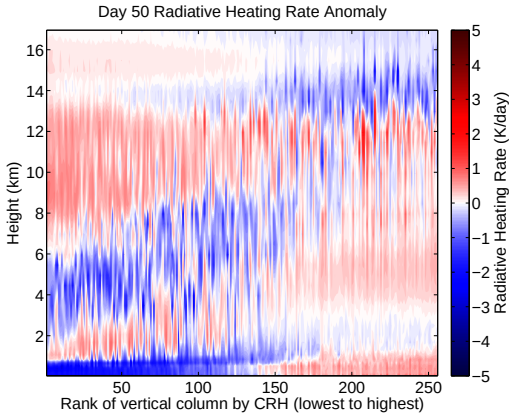

(b) Anomaly from Day 10 Mean

Figure 2-15: Moisture-sorted vertically averaged radiative heating rate (a) and radiative heating rate anomaly from the day 10 domain mean (b), at day 50 of the simulation at 305 K. Top panel of (a) is shortwave, middle is longwave, bottom is total radiative heating rate - note the different axes.

moist regions (top panel of Figure 2-15a) while longwave cooling is reduced (although not compared with the driest regions) (middle panel of Figure 2-15a). Both of these effects contribute towards a less negative vertically averaged total radiative heating rate in the moist regions. This gradient in radiative heating between the dry and moist regions increases as the simulation progresses. In fact, during the time there is a mature cluster, the vertically averaged radiative heating rate is nearly zero in the moistest columns where the clouds are concentrated, but there is strong radiative cooling over the rest of the domain (not shown). We can also examine the radiative heating rates as a function of both height and moisture-rank (Figure 2-15b). In this case, rather than examining the actual radiative heating rates at day 50, we examine their anomaly from the day 10 domain mean to determine which areas are cooling more or less than the spatial average. In the moist regions, there are positive anomalies throughout most of the troposphere, which indicates less radiative cooling (or more radiative heating). In the dry regions, there is less radiative cooling in the upper troposphere (positive anomalies), but more radiative cooling throughout most of the lower troposphere and boundary layer (negative anomalies). The fact that there are opposite signed radiative heating rate anomalies at different heights in the dry regions turns out to be important for determining the sign of the longwave radiative feedback and explaining the temperature dependence of self-aggregation (see Chapter 4).

2.5 Size/Strength of Cluster

2.5.1 Strength of Cluster

We examine how the strength of the self-aggregated cluster depends on the SST of the simulation. Figure 2-16 shows the evolution of the strength of the cluster with time, for the four runs that self-aggregated. In Figure 2-16a the strength of the cluster is defined as the difference between the 95th and 25th percentiles of column relative humidity. Two things are notable from this figure. First, there is a huge increase in the

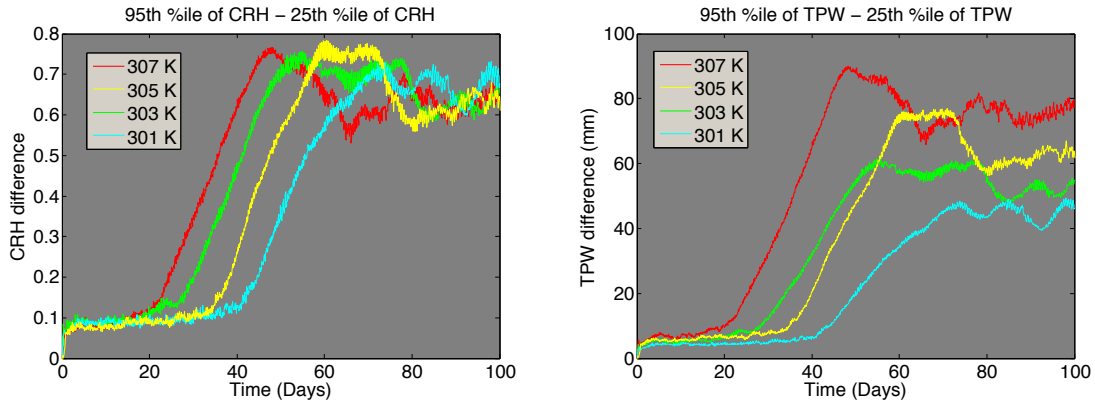

(a) CRH metric

(b) TPW metric

Figure 2-16: Evolution of the strength of the cloud cluster for the runs that self-aggregated.

column relative humidity difference as aggregation occurs. In the aggregated state, there is a much larger gap in the column relative humidity of the moister and dryer areas. Second, the CRH difference in the aggregated state is roughly independent of temperature, with all four runs converging.

This is not the case if an absolute metric of cluster strength is used, such as the difference between the 95th and 25th percentiles of total precipitable water. In that case (Figure 2-16b), the strength of the cluster appears to be stronger at higher SSTs, presumably due to the exponential increase of water vapor with temperature following the Clausius-Clapeyron relation. The 95th percentile of TPW increases much more with higher SST than the 25th percentile does. However, when we normalize by the saturated water vapor path and use column relative humidity as our metric, this normalized strength metric does not vary much with temperature, as shown by Figure 2-16a. Another absolute metric of the strength of the aggregation is the domain mean spatial variance of the vertically integrated frozen moist static energy. This also increases with SST (Figure 2-7a), confirming that the gradient between moist and dry regions is larger at higher temperatures.

While the system achieves a quasi-steady state once it has aggregated into a single cluster, there are some interesting high frequency oscillations in the strength of the cluster. These regular pulsations are most prominent when viewing animations of the

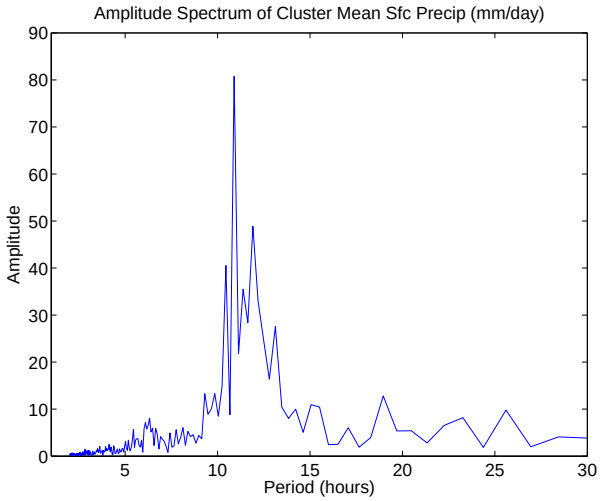

Figure 2-17: Amplitude spectrum of surface precipitation rate (mm/day) averaged over the cluster area (from x = 300 km to x = 429 km and y = 150 km to y = 276 km.

cluster; for example, plotting brightness temperature or an isosurface of cloud condensate. This variability also appears as oscillations in various cluster-average quantities, such as surface precipitation rate, surface enthalpy flux, or outgoing longwave radiation. To characterize the time scale of this variability, we calculate the amplitude spectrum of the cluster mean surface precipitation rate for the simulation at 305 K (Figure 2-17). We review how we define the "cluster area" in the next section. The peak in amplitude occurs at a period of 10.9 hours. We find the same spectral peak when considering cluster mean OLR or surface enthalpy fluxes. We speculate that this variability results from gravity waves excited by the convection propagating back around through the doubly periodic domain, reinforcing the convection at regular intervals. To test this hypothesis, we calculate a rough estimate of the gravity wave speed in our simulation.

The horizontal phase speed for a gravity wave in a continuously stratified nonrotating fluid is

$$c_x = \frac{N}{m}, \tag{2.6}$$

where N is the Brunt-Väisälä frequency (Equation (3.4)) and m is the vertical wavenumber. However, if we assume the tropopause behaves like a rigid lid, then the vertical

wavelength must be an integer (n) fraction of twice the tropospause height (z_T), and Equation (2.6) becomes

$$c_x = \frac{N z_T}{n\pi}. \tag{2.7}$$

We estimate that the tropopause is at a height of 15.5 km and that 0.0105 s^{-1} is a characteristic value for N (Table 3.2) in our simulation at 305 K. Using Equation (2.7), we find values of 52 m/s, 26 m/s, and 17 m/s for the phase speeds of the first three gravity wave modes. Given a domain size of 768 km, these phase speeds correspond to time scales of approximately 4 hours, 8 hours, and 12 hours. The latter two are on the same order of magnitude as our observed period of 10.9 hours. An analysis of the amplitude spectrum of the cluster mean surface enthalpy flux for the large domain (1536 x 1536 km^2) simulation at 310 K indicates a peak at a period of 16.0 hours. This is very close to the time scale of 15.8 hours that would be expected from the third gravity wave mode in that simulation. While this analysis suggests that gravity waves are a plausible explanation for the pulsations, the evidence is far from conclusive. [3]

2.5.2 Size of Cluster

An unresolved question regarding self-aggregation is what sets the size of the cluster. Regardless of the SST or the domain size, there is only ever one cluster. This suggests that the size of the domain constrains the size of the cluster. Muller and Held (2012) did not find any correlation between the area of the aggregated region and the domain size or resolution. Defining the area of the aggregated region is somewhat subjective, as it may vary somewhat with time and requires the choice of a threshold value. Here, we define the size of the cluster as the region contained by a surface

[3]There are numerous assumptions in our calculation; it is only meant as a rough estimate. We estimated the tropopause height using the cold point; a different definition may be more suitable. We calculated N from the domain mean of the small domain simulations at 305 K and 310 K; to be more accurate we should have calculated it for the non-cluster area in the self-aggregating simulation. The assumption that the tropopause behaves like a rigid lid and the use of Equation (2.7) may not be valid. Finally, it may be necessary to take the size of the cluster into account when calculating how long it will take a gravity wave of a given phase speed to propagate through the domain back to the cluster.

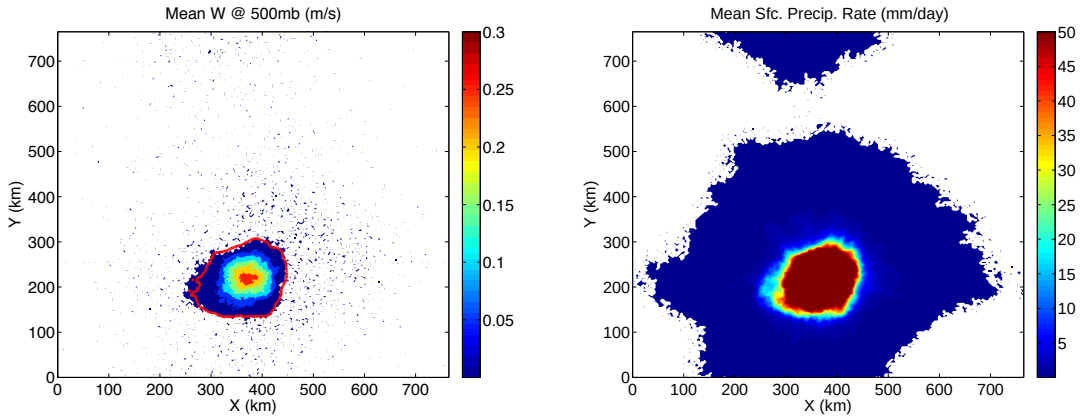

(a) Vertical Velocity (m/s) (b) Surface Precipitation Rate (mm/day)

Figure 2-18: Metrics to define the size of the cluster. Averaged over the last 15 days of the simulation at 305 K. (a) shows the mean vertical velocity at 500 mb (color shading, white represents $w \leq 0$) and the 50 mm/day mean surface precipitation rate contour (red contour). (b) shows the mean surface precipitation rate, where the color scale saturates at 50 mm/day.

precipitation rate contour that encloses the area of time-mean ascent. We choose the appropriate precipitation rate value by subjectively determining which contour best encloses a contiguous area of time-mean ascent. We define time-mean ascent as the positive values of the vertical velocity at 500 mb averaged over the last 15 days of the simulation (an example for the 305 K simulation is shown in Figure 2-18). We average the surface precipitation rate over the same time period. This metric is meant to contain the core of the cluster; there may be light precipitation or cloud cover that extends further. The results of this analysis are shown in Figure 2-19. Note that the locations of the clusters have been shifted such that they all can be viewed on the same plot. We do not find a correlation between the size of the cluster and the SST. This is also true for other definitions of the size of the cluster, such as a threshold value of precipitable water. In Table 2.4, the cluster size is defined as the area where the precipitable water is greater than one standard deviation above the domain mean value. Using this definition, the cluster covers 15-17 % of the horizontal area of the domain. It is likely that the domain size is constraining the size of the cluster, which is discussed further in Chapter 3.

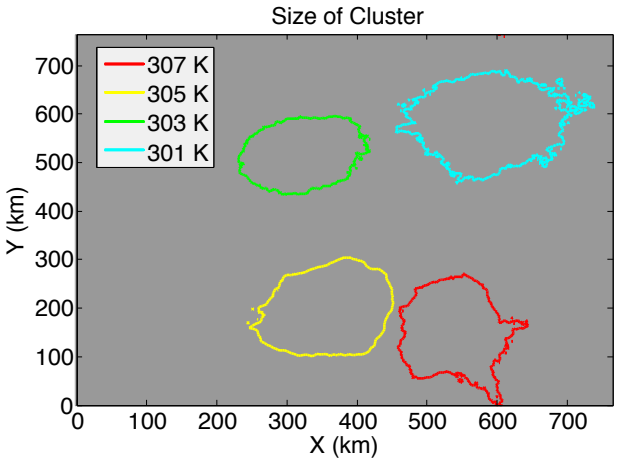

Figure 2-19: Size of cluster at different SSTs. The contour of mean surface precipitation rate that contains the region of mean ascent is plotted, based on an average over the last 15 days of simulation.

Table 2.4: Cluster size, defined as area where $PW > PW_{\text{mean}} + PW_{1\sigma}$, for simulations at different SSTs. The 310 K simulation has horizontal dimensions of 1536 x 1536 km^2; the other simulations have dimensions of 768 x 768 km^2. The values shown are averages over the final 10 days of the simulation.

SST	Cluster Area	Fraction of Total Area
301 K	10.4 x 10^4 km^2	17.6 %
303 K	9.2 x 10^4 km^2	15.6 %
305 K	9.3 x 10^4 km^2	15.7 %
307 K	8.9 x 10^4 km^2	15.2 %
310 K	38.2 x 10^4 km^2	16.2 %

Chapter 3

Sensitivity Tests

3.1 Experiment Design

The results of the moisture sorted analysis in Chapter 2 as well as insights from previous studies, as reviewed in Chapter 1, have identified several feedbacks that may control self-aggregation. Previous work has indicated that cloud-water vapor-radiation feedbacks that dry the drier air columns and moisten the moister air columns are essential to the self-aggregation process (Tompkins, 2001b; Bretherton et al., 2005; Muller and Held, 2012). Deep convection can more easily develop where the middle-troposphere is already moist and then tends to keep the middle and upper troposphere moist where it is convecting. This moisture-convection feedback has also long been recognized as important for convective organization (Held et al., 1993; Tompkins, 2001b). Surface flux feedbacks are a third contender, although there are somewhat conflicting results in the literature as to their necessity for self-aggregation (Bretherton et al., 2005; Muller and Held, 2012). As a first step towards identifying the mechanisms of aggregation in our simulations, we perform a series of sensitivity tests. These tests are designed to test the robustness of self-aggregation. They will also be used to put our set of simulations in the context of previous studies. It is possible that the dominant mechanism at play depends on the precise model parameters, therefore, it is important to confirm that the mechanisms suggested by previous studies are also the relevant ones in our set of simulations. The results of the

sensitivity tests will inform our analysis of the physical mechanisms of self-aggregation in Chapter 4, as well as suggest candidates for explaining the temperature dependence of aggregation.

We first test the sensitivity of self-aggregation to aspects of the radiation calculation, including the radiation scheme used and the presence of a diurnal cycle. We perform a series of mechanism denial experiments in which the longwave and shortwave radiation feedbacks are successively removed. Next, we examine the importance of surface flux feedbacks in both simulations that do and do not aggregate. We also test the robustness of self-aggregation to the microphysics scheme. In the penultimate section, we investigate the role of cold pools by eliminating the low-level evaporation of precipitation. Finally, we examine how domain size modulates the temperature dependence of self-aggregation. The primary set of mechanism denial experiments, carried out for the simulation at 305 K (which, as shown in Chapter 2, aggregates), is summarized in Table 3.1.

3.2 Radiation

3.2.1 Radiation Scheme

Interactive radiation, that is, a calculation of radiative fluxes that depends on the temporal and spatial distribution of temperature, water vapor, and cloud condensate calculated by the model, has been viewed as essential to self-aggregation (Tompkins and Craig, 1998; Bretherton et al., 2005; Stephens et al., 2008; Muller and Held, 2012). Therefore, it is possible that self-aggregation is sensitive to the precise formulation of the radiative calculation. We test the robustness of self-aggregation to the radiation scheme used (Figure 3-1).

As mentioned in Chapter 2, we use the RRTM radiation scheme to compute the longwave and shortwave radiative fluxes. Muller and Held (2012), however, used the radiation code from the National Center for Atmospheric Research (NCAR) Community Atmosphere Model version 3 (CAM3) (Collins et al., 2006). Therefore, we test

Table 3.1: Summary of mechanism denial experiments at 305K.

Experiment	Aggregates?	Run Description
Rad-Homog	No	Radiative heating rate homogenized horizontally at each time step and height
Rad-Fix	No	Radiative heating rate prescribed as a profile that is fixed horizontally and in time
LWRad-Fix	No	Longwave radiative heating rate prescribed as a profile that is fixed in space and time
SWRad-Fix	Yes	Shortwave radiative heating rate prescribed as a profile that is fixed in space and time
LWqv-Fix	No	Water vapor used in longwave radiation calculation prescribed as a profile that is fixed in space and time
SWqv-Fix	Yes	Water vapor used in shortwave radiation calculation prescribed as a profile that is fixed in space and time
SfcFlux-Homog	No	Surface fluxes homogenized horizontally at each time step
Wind-Homog	No	Wind speed that enters surface flux calculation homogenized horizontally at each time step
Disequil-Homog	Yes	Air-sea enthalpy disequilibrium that enters surface flux calculation homogenized horizontally at each time step

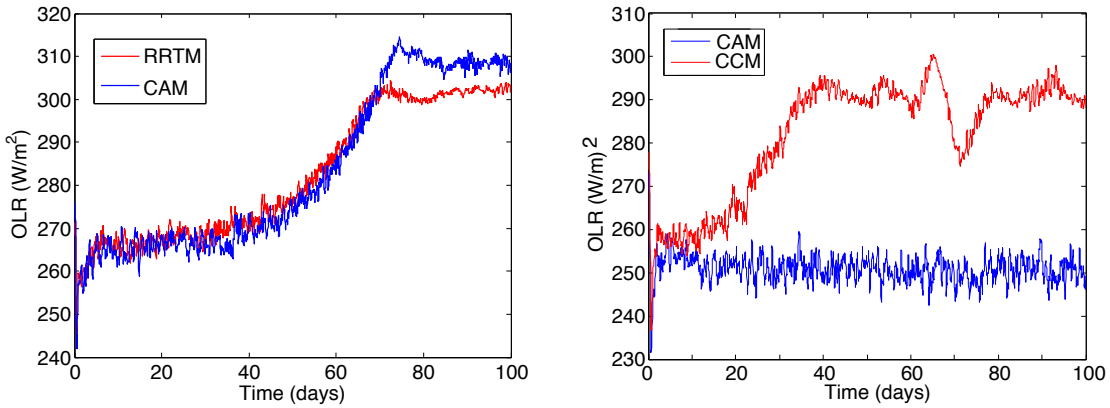

(a) RRTM vs. CAM3

(b) CAM3 vs. CCM3

Figure 3-1: Domain averaged outgoing longwave radiation (OLR, W/m^2), with different radiation schemes. (a) Simulations with SAM Version 6.8.2 at 305 K, 768 x 768 km^2 domain. (b) Simulations with SAM Version 6.7.5 at 301 K, 576 x 576 km^2 domain.

the sensitivity of our "standard run" to this choice of radiation scheme (Figure 3-1a). The results indicate that, at least in terms of the evolution of the domain averaged OLR, this simulation is not particularly sensitive to the radiation scheme. Both simulations aggregate, although the domain average OLR in equilibrium is several W/m^2 higher with CAM3 radiation than with RRTM.

Our first attempt at simulating self-aggregation was modeled after Bretherton et al. (2005), who used the radiation code from the NCAR Community Climate Model version 3 (CCM3) (Kiehl et al., 1998) in an earlier version of SAM. Their simulation was performed at 301 K with a 576 x 576 km^2 doubly periodic domain. The results of our attempt to replicate their simulation, using version 6.7.5 of SAM, are shown in Figure 3-1b. Self-aggregation occured when CCM3 radiation was used, and it occurred much more quickly than in our other simulations (see Chapter 2). However, when we repeated the same experiment with CAM3 radiation, aggregation did not occur. We speculate that the sensitivity to radiation scheme in this case is due to the simulation being performed near the temperature threshold for aggregation, as well as on a smaller domain than in Figure 3-1a. Indeed, simulations of self-aggregation near the critical SST have proven very sensitive to physical and numerical details (Muller and Held, 2012) so it is not surprising that the choice of radiation scheme matters. However, it is somewhat reassuring that self-aggregation in the particular simulation we focus much of our analysis on (768 x 768 km^2, 305 K) is robust to the choice of radiation scheme (Figure 3-1a).

3.2.2 Radiation Mechanism Denial

We perform a series of experiments that test the sensitivity of self-aggregation to radiation feedbacks. All are performed at an SST of 305 K. The results are summarized in Table 3.1. First, we remove local radiation feedbacks by horizontally homogenizing the radiative heating rate at each time step before it is applied as a temperature tendency (Rad-Homog). We use the term "homogenize" to mean uniformly applying the horizontal mean radiative heating profile to all grid columns. As indicated by Figure 3-2a, this prevents self-aggregation, which is consistent with previous studies

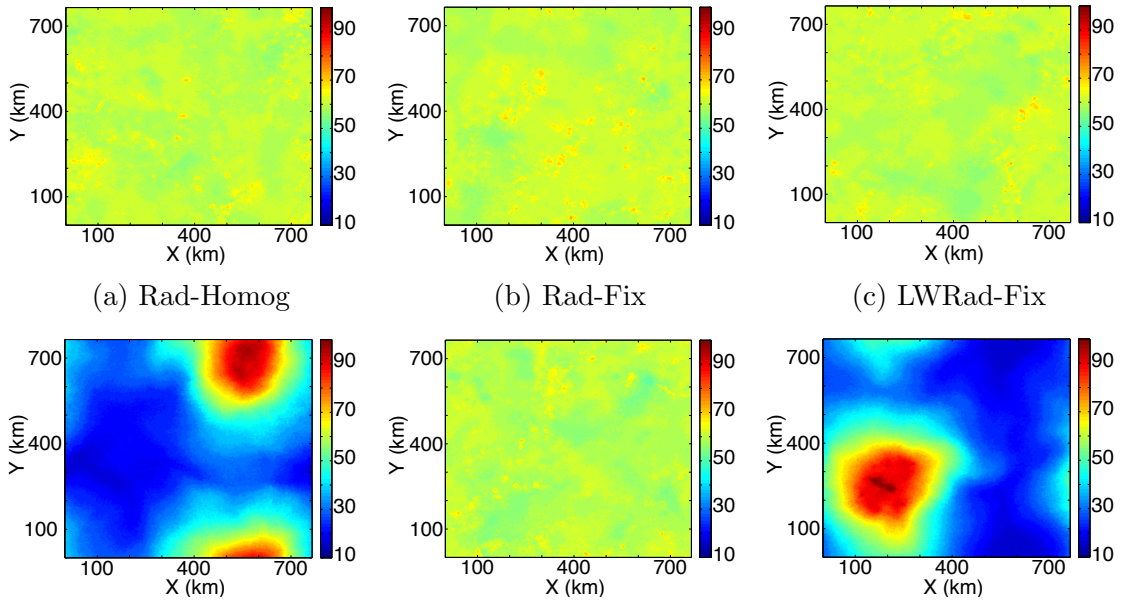

(a) Rad-Homog (b) Rad-Fix (c) LWRad-Fix

(d) SWRad-Fix (e) LWqv-Fix (f) SWqv-Fix

Figure 3-2: Hourly average precipitable water (mm) at day 83.3 for radiation mechanism denial experiments. The color bar is between 10 mm and 100 mm.

(Bretherton et al., 2005). This experiment does allow for the possibility of feedbacks associated with the time tendency of the horizontal mean radiative heating, so to completely eliminate feedbacks associated with interactive radiation, we perform a second test in which the radiative heating rate is externally prescribed (Rad-Fix). In Rad-Fix, the interactive radiation scheme is replaced with horizontally uniform non-interactive radiative heating rates that are fixed in time. We derive this profile from the horizontal and time mean over the first five days of the control simulation at 305 K (that is, before it aggregates) (Figure 3-3). Figure 3-2b shows that aggregation does not occur with fixed radiative heating. We perform two additional sensitivity tests, one in which the longwave is fixed but the shortwave is still calculated interactively (LWRad-Fix) and one in which the shortwave is fixed but the longwave is calculated interactively (SWRad-Fix). LWRad-Fix does not aggregate, but SWRad-Fix does (Figure 3-2c,d). This indicates that interactive longwave radiation is essential for the initiation of self-aggregation, while interactive shortwave radiation is not. This does not mean that shortwave feedbacks are negligible, but any role they play would be of secondary importance. These results are consistent with the sensitivity experiments

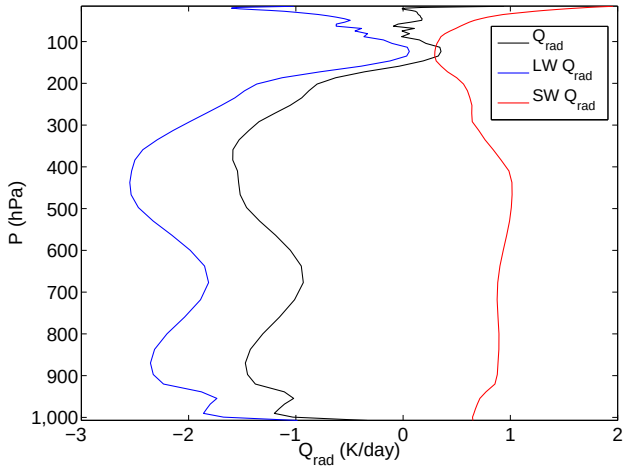

Figure 3-3: Horizontal mean and day 1-5 mean radiative heating rate profile from control 305 K simulation. Total radiative heating rate (black), longwave radiative heating rate (blue) and shortwave radiative heating rate (red), used in Rad-Fix, LWRad-Fix, and SWRad-Fix, respectively.

performed by Muller and Held (2012), although they uniformly applied the horizontal mean longwave and shortwave radiative heating rates at each time step, rather than fixing them at a profile that was constant in both space and time.

Radiative feedbacks are thought to be important for self-aggregation because of the dependence of radiative heating on water vapor and clouds. Water vapor is a strong absorber of both longwave and shortwave radiation; therefore, the radiative heating rates are modulated by spatial variations in the water vapor profile. Here we test the importance of water vapor-radiation interactions for self-aggregation by prescribing the water vapor profile that is used in the radiation calculation. This water vapor profile is fixed in space and time, and is derived from the horizontal mean over the first five days of the control simulation at 305 K (Figure 3-4). In the LWqv-Fix experiment, we prescribe the water vapor profile used in the longwave calculation, but allow the shortwave calculation to use the actual water vapor values calculated by the model. We note that in this experiment, both the longwave and shortwave radiation calculations still use the model-calculated cloud water and ice concentrations. Fixing the water vapor used by the longwave calculation prevents self-aggregation (Figure 3-2e). Conversely, aggregation still occurs when we fix the

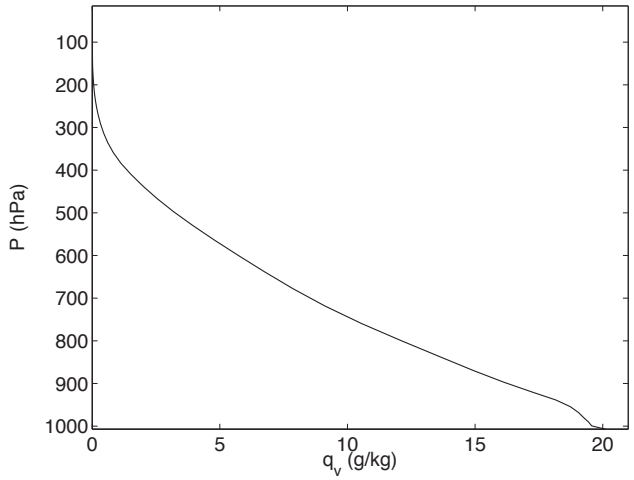

Figure 3-4: Horizontal mean and day 1-5 mean water vapor profile from control 305 K simulation. Used in LWqv-Fix and SWqv-Fix.

water vapor used by the shortwave calculation (and allow the longwave to use the actual water vapor from the model) (Figure 3-2f). This result provides additional evidence that feedbacks resulting from the shortwave radiation are not essential for self-aggregation. Longwave radiation that depends on the variable water vapor is necessary, however. Retaining the cloud-radiation interactions is apparently not sufficient for the instigation of aggregation, although they may be important for maintaining the cluster once it has formed. Our finding contradicts the results of Muller and Held (2012); in their study, aggregation still occurred when the water vapor that entered the longwave calculation was homogenized. Their experiment was not quite the same as ours, as they homogenized the water vapor at each time step instead of prescribing a fixed profile and additionally homogenized the shortwave radiative heating and surface fluxes. Muller and Held (2012) also used a lower SST for their mechanism denial experiments. The only actions that prevented aggregation in their simulations were zeroing or homogenizing the amount of liquid condensates entering the computation of longwave radiation, leading to their conclusion that radiative cooling from low clouds was responsible for aggregation. Our radiation mechanism denial experiments instead suggest that it is the water vapor - longwave radiation interaction that is essential for the initial aggregation.

3.2.3 Diurnal Cycle

The previous investigations of self-aggregation have all used simulations with constant solar insolation. For example, Bretherton et al. (2005) removed the diurnal cycle by reducing the solar constant to 650.83 W/m^2 and fixing the solar zenith angle at 50.5 °. This results in a solar insolation of 413.9766 W/m^2. It is not obvious how diurnally varying solar insolation would affect self-aggregation. With a fixed surface temperature, the impacts of shortwave radiation are limited to atmospheric absorption and reflection from clouds. Furthermore, the sensitivity tests in the previous section suggest that feedbacks involving shortwave radiation are not essential for self-aggregation. However, with a diurnal cycle, at night there is no shortwave heating to partially offset longwave cooling. There would be enhanced radiative cooling of the atmosphere across the entire domain at night (compared to the case with no diurnal cycle), which could disrupt the longwave radiation feedbacks.

We test the sensitivity of self-aggregation to diurnally varying solar insolation by repeating the simulation at 305 K and calculating the solar insolation, rather than externally prescribing it. We use a latitude of 19.45 ° and begin the simulation at day 80.5, enforcing a perpetual equinox. These specifications result in a time mean solar insolation of 413.5924 W/m^2, which is nearly the same as the value of 413.9766 W/m^2 in the fixed insolation case. We find that the diurnal cycle simulation does self-aggregate. In fact, the evolution of the domain average OLR is very similar between the diurnal cycle simulation and the fixed insolation simulation (Figure 3-5). The process of self-aggregation, which takes tens of days, is seemingly unaffected by the higher frequency diurnal variability. Also, just as in the fixed insolation case, varying the white noise that initializes motion varies the spatial orientation of the cluster. Of the two diurnal cycle simulations we performed, one achieved a band structure (Figure 3-6) while one aggregated into circular cluster.

It is difficult to observe a diurnal signature in the convection in animations because of additional, higher frequency pulsations (that also occur in simulations with fixed insolation). Figure 3-7 shows the amplitude of the Fourier transformed cluster mean

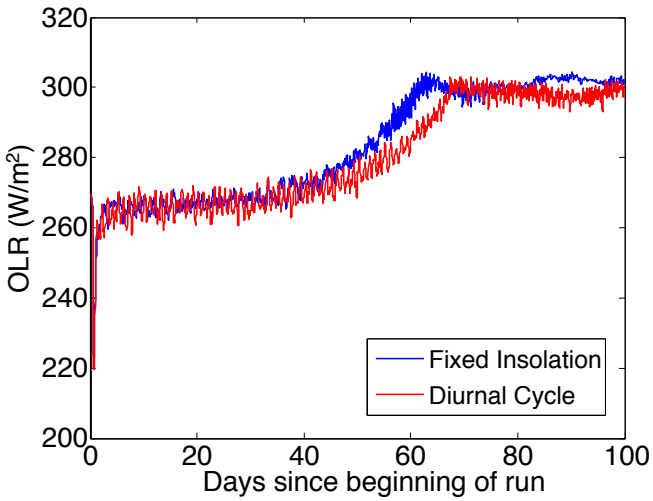

Figure 3-5: Domain averaged outgoing longwave radiation (OLR, W/m^2) for simulations with (red) and without (blue) a diurnal cycle of solar insolation. Each simulation has the nearly the same mean solar insolation and sea surface temperature (305 K).

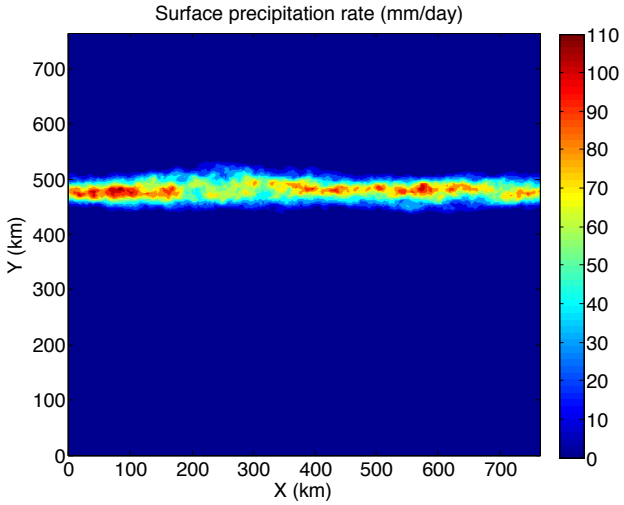

Figure 3-6: Surface precipitation rate (mm/day) averaged over the last 16 days of the diurnal cycle simulation at 305 K (red curve in Figure 3-5).

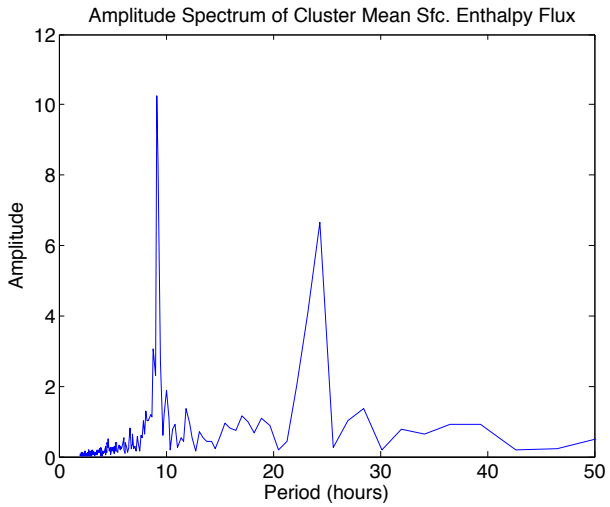

Figure 3-7: Amplitude spectrum of surface enthalpy flux averaged over the cluster area (from x = 0 km to x = 768 km and y = 450 km to y = 504 km, see Figure 3-6).

surface enthalpy flux, as an example. The largest spectral peak occurs at a period of 9.1 hours, while the second peak is a result of the diurnal cycle and has a period of 24.4 hours. The 9 hour peak also occurs in simulations with fixed insolation. In Chapter 2, we speculated that these pulsations of the cluster result from gravity waves excited by the convection propagating back around through doubly periodic domain.

We perform diurnal composites of cluster mean quantities to objectively determine the modulation of the cluster by the diurnal cycle of solar radiation (Figure 3-8). The cluster mean precipitation peaks just before sunrise and has a minimum near noon (Figure 3-8a). This is broadly consistent with the observed diurnal variation in tropical oceanic precipitation, although the observed precipitation has its minimum later in the afternoon (Liu and Zipser, 2008). We will show in Chapter 4 that, while the column shortwave flux convergence is overall enhanced in the moist regions, in the center of the cluster it is reduced due to the reflection by clouds. This reduction of shortwave heating is not favorable for maintaining convection in the center of the cluster. One possible explanation for the diurnal variation in the cluster mean precipitation is that, at nighttime, this negative feedback is no longer present and convection is able to intensify. We also note that the 9 hour peak in power from Figure 3-7 is not apparent in the diurnal composite, providing additional evidence

that those pulsations are not a harmonic of the diurnal cycle. The diurnal composite of the cluster mean surface enthalpy fluxes is similar to that of the precipitation, but phase lagged such that they peak just after sunrise and have a minimum in the late afternoon (Figure 3-8b). Note that the cluster mean enthalpy fluxes are less than those in the rest of the domain. This is because the air-sea disequilibrium is reduced because the boundary layer in the cluster region is so moist, thereby suppressing the surface enthalpy fluxes (this will be reviewed in more detail in Chapter 4). There is only a slight diurnal variation in the cloud fraction of the cluster (not shown).

3.3 Surface Fluxes

3.3.1 Gust Factor

We indirectly test the importance of turbulent surface enthalpy fluxes in self-aggregation by varying the minimum wind speed in the surface flux calculation. The surface sensible and latent heat fluxes are computed according to the bulk aerodynamic formulae. The wind speed that enters this formulation in the model calculation is given by

$$U = \max\left(U_{min}, \sqrt{u_{bot}^2 + v_{bot}^2}\right), \tag{3.1}$$

where u_{bot} and v_{bot} are the winds at the lowest model level. U_{min} is the minimum wind speed, which we refer to as the gust factor. We find that a smaller gust factor in the surface flux calculation favors self aggregation. As an example, we consider the 301K run. With a gust factor of $1\,m/s$, the model self-aggregates and a cluster forms, as indicated by the blue line in Figure 3-9 and the left panel of Figure 3-10. However, when the gust factor is increased to $4\,m/s$, which is represented by the cyan line in Figure 3-9, self-aggregation does not occur.

We note that increasing the gust factor does not completely prevent self-aggregation, as the right panel of Figure 3-10 indicates a dry patch forming, but causes it to proceed much slower. If run for longer than 100 days, perhaps that simulation would eventually self-aggregate. The mechanism at play is two-fold. With a lower gust factor,

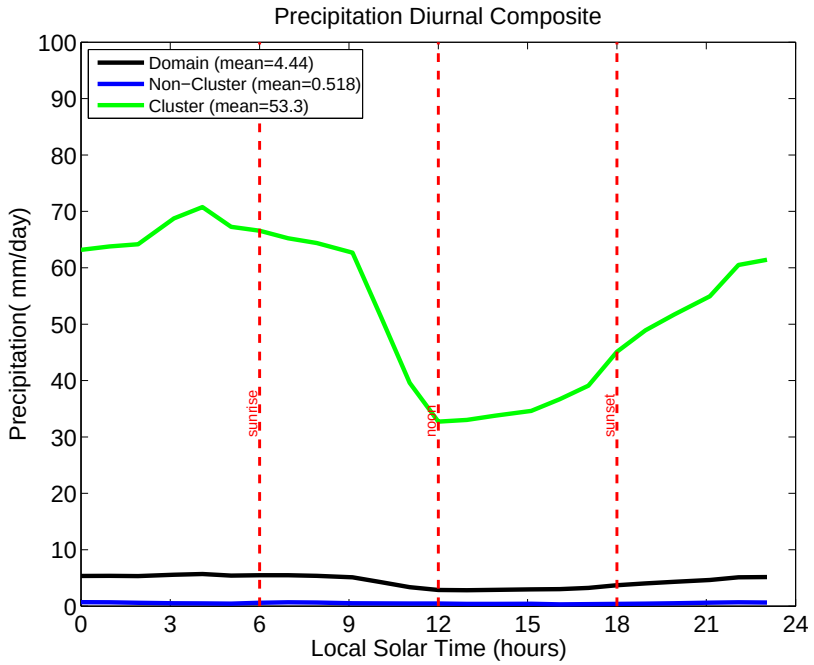

(a) Precipitation rate

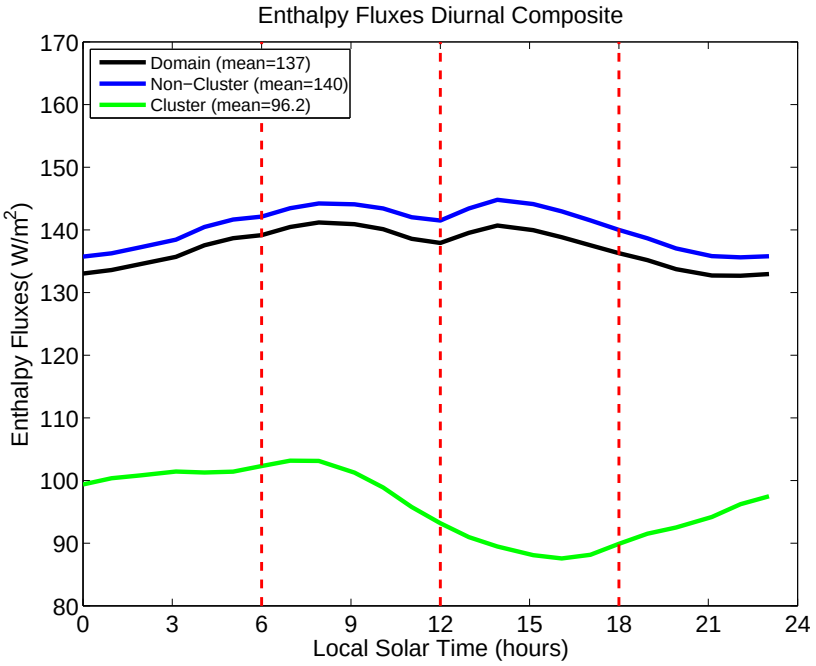

(b) Surface enthalpy fluxes

Figure 3-8: Diurnal composites of the precipitation rate (a) and surface enthalpy fluxes (b), over the last 16 days of the diurnal cycle simulation at 305 K (red curve in Figure 3-5). The cluster area is defined as from x = 0 km to x = 768 km and y = 450 km to y = 504 km (see Figure 3-6).

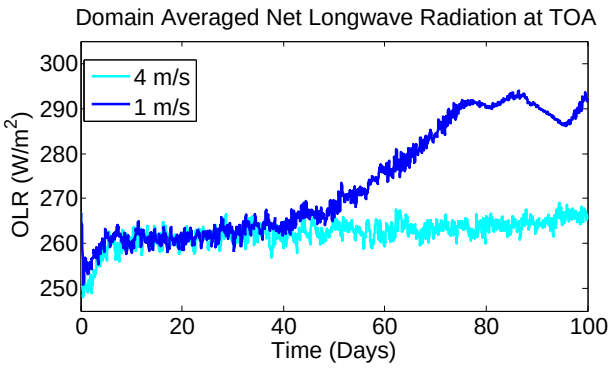

Figure 3-9: Evolution of domain averaged outgoing longwave radiation at an SST of 301K, for a simulation with a $4\,m/s$ gust factor (cyan) and a simulation with a $1\,m/s$ gust factor (blue).

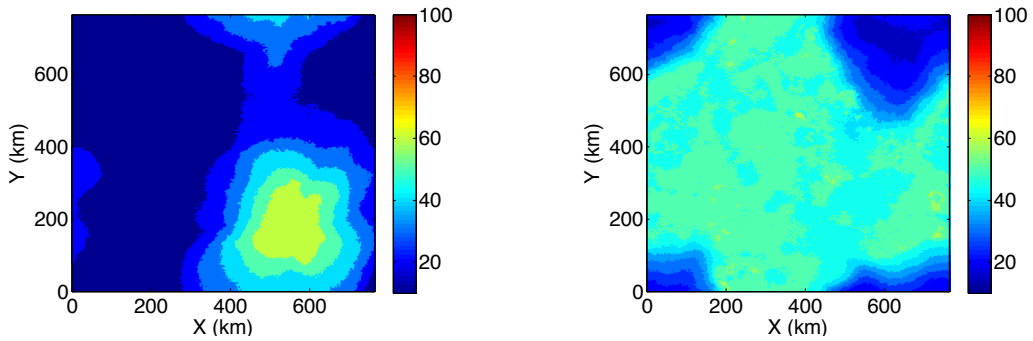

(a) $U_{min} = 1\,m/s$ (b) $U_{min} = 4\,m/s$

Figure 3-10: Day 100 precipitable water (mm) at SST of 301K.

one needs a larger air-sea enthalpy disequilibrium to get a strong surface flux, making wind-related surface flux feedbacks more active. Second, with a lower gust factor, it takes less real gustiness to differentiate between convecting and non-convecting regions. The gusts are thus more effective at amplifying the surface fluxes in the convective regions.

We interpret these results as suggesting that surface flux feedbacks are favorable, but perhaps not necessary, for self-aggregation. This is consistent with the conclusion of Muller and Held (2012), who found that homogenizing the surface fluxes prevented aggregation in some, but not all, of their simulations. These results also suggest that applying a mean surface wind would suppress aggregation, since the addition of a constant background wind everywhere would make it more difficult for real gustiness

to differentiate between convective and non-convecting regions.

3.3.2 Mean Wind

Most of our simulations have no mean wind; that is, there is no background wind and no nudging of the domain mean wind. To test the sensitivity of self-aggregation to the presence of a mean wind, we perform three simulations at 305 K with mean background winds of 2.5 m/s, 5 m/s, and 10 m/s. In each case the domain mean wind is nudged, with a time scale of 2 hours, to a westerly wind constant with height. This background wind is also added to the modeled surface wind in the surface flux calculation. We find that the simulation with a mean wind of 2.5 m/s still aggregates, but the cluster is slightly elongated in the x-direction, and drifts from west to east with time. The time to aggregation is greater than in the control simulation, but given the large degree of variability in the time to aggregation (Chapter 2), it is difficult to attribute this the presence of the mean wind. The simulation with a mean wind of 5 m/s does not fully aggregate, but the domain average OLR does gradually increase, as if it is tending towards aggregation. Plan views of precipitable water indicate that it evolves into a broad, moist band, but the contrast between the moist and dry areas is not as large as is found in a fully aggregated simulation. Finally, a mean wind of 10 m/s completely suppresses aggregation during the time period of the simulation. The presence of a mean wind suppresses aggregation due to its effect on the surface fluxes (the same mechanism by which the gust factor affects the surface fluxes, as described in Section 3.3.1). The sensitivity of self-aggregation to the presence of a mean wind suggests that aggregation is unlikely to occur in nature (where there can be significant mean winds) exactly as it occurs in these idealized model simulations.

3.3.3 Homogenize Surface Flux Feedbacks

To ascertain the importance of surface flux feedbacks for our particular self-aggregation simulation, we perform a series of mechanism denial experiments at 305 K. The results are summarized in Table 3.1. First, as has been done in previous studies (Bretherton

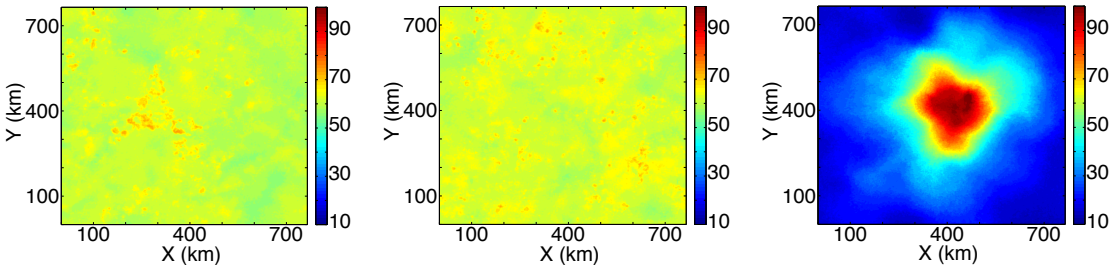

(a) SfcFlux-Homog (b) Wind-Homog (c) Disequil-Homog

Figure 3-11: Hourly average precipitable water (mm) at day 83.3 for surface flux mechanism denial experiments. The color bar is between 10 mm and 100 mm.

et al., 2005; Muller and Held, 2012), we horizontally homogenize the surface fluxes of sensible and latent heat at each time step (SfcFlux-Homog). This simulation fails to aggregate, which is consistent with Bretherton et al. (2005) (Figure 3-11a). We do two additional experiments to determine which part of the surface flux feedback is necessary for self-aggregation. The surface latent and sensible heat fluxes are given by the standard bulk formulae:

$$\text{LHF} = \rho c_E L_v U \left(q^*_{T_s} - q_{bot}\right) \tag{3.2}$$

$$\text{SHF} = \rho c_H c_p U \left(T_s - T_{bot}\right). \tag{3.3}$$

Spatial variations in the surface fluxes therefore arise from variations in the surface wind speed, U, or the air-sea disequilibria, $\Delta q = q^*_{T_s} - q_{bot}$ and $\Delta T = T_s - T_{bot}$ [1]. The surface flux feedback is made up of a wind speed - surface flux feedback (often referred to as WISHE) and an air-sea disequilibrium surface flux feedback. There is also a part of the surface flux feedback that is due to the product of wind and disequilibrium variations; we do not address this here but do so in our feedback analysis in Chapter 4. We remove the WISHE feedback by horizontally homogenizing the wind speed, U, that enters the surface flux calculation at each time step (Wind-Homog). We remove the air-sea disequilibrium feedback by horizontally homogenizing Δq and ΔT at each time step before using them in the surface flux calculation (Disequil-Homog). Wind-

[1] U is given by Equation (3.1). q_{bot} and T_{bot} are the water vapor and temperature at the lowest model level, respectively.

Homog fails to aggregate, but Disequil-Homog does (Figure 3-11b,c). Therefore, it is the removal of the wind part of the surface flux feedback that prevents aggregation in SfcFlux-Homog. We repeat Wind-Homog at 303 K and find that the removal of the WISHE feedback prevents aggregation in that simulation as well (not shown). This result is consistent with Tompkins and Craig (1998), who found that using a wind-independent surface flux calculation destroyed aggregation in their simulations. They tested the importance of wind-sensitive fluxes by calculating the surface fluxes as a Newtonian relaxation towards the sea surface state, rather than horizontally homogenizing the wind speed entering the surface flux calculation as was done here.

The fact that Disequil-Homog still aggregates could indicate that the effect of variations in the air-sea disequilibrium on surface fluxes is not relevant to self-aggregation. It could also indicate that air-sea disequilibrium variations cause a negative feedback on self-aggregation. Removal of this negative feedback by homogenizing the air-sea disequilibrium could allow a simulation to aggregate that otherwise would not. To test this hypothesis, we repeat Disequil-Homog at 300 K, which is just below the SST threshold of aggregation in our simulations (Figure 2-1). However, the simulation still fails to aggregate. This does not necessarily mean that the disequilibrium - surface flux feedback is not negative, just that its removal is not sufficient for aggregation to occur at 300 K. Indeed, the analysis in Chapter 4 does indicate that the air-sea disequilibrium - surface flux feedback is negative, so we use this as an example of how mechanism denial experiments can be misleading, or at least may not tell the entire story. In actuality, all the 300 K simulation needs to aggregate is more time; when extended for an additional 40 days, a cluster forms. This is likely because the 300 K simulation is very close to the critical SST for aggregation. Restarting the 300 K simulation and also homogenizing the air-sea disequilibrium allows the cluster to form sooner than if it was restarted normally, but given the variation in time to aggregation that occurs randomly (see Chapter 2), it is difficult to draw a conclusion from this result. We performed a final sensitivity test in which the 297 K simulation was extended for an additional 40 days, with the air-sea disequilibrium homogenized, and it still failed to aggregate.

In sum, the results of the sensitivity tests in which various aspects of the surface flux feedback are homogenized indicate that, at least in our simulations, interactive surface fluxes are necessary for aggregation to occur. In particular, the dependence of the surface fluxes on a spatially varying surface wind is the key interaction.

3.4 Microphysics

Bretherton et al. (2005) found that self-aggregation was profoundly affected by changes in the microphysics scheme. Specifically, they found that changing the threshold mixing ratio for auto conversion from cloud ice to snow from 0 to 0.1 g/kg, slowed down self-aggregation by enhancing the radiative impact and longevity of cirrus clouds in the dry regions. This result shows the potential for self-aggregation to be sensitive to the details of the microphysics parameterization. As stated in Chapter 2, we use a one-moment bulk microphysics package described in Khairoutdinov and Randall (2003). In this scheme, there are two prognostic microphysical variables: total non-precipitating water and total precipitating water, which are then partitioned into five classes of hydrometeors as a function of temperature. We perform one sensitivity test in which we replace this scheme with the Morrison et al. (2005) two-moment, five-class bulk microphysics scheme. In the Morrison et al. (2005) scheme, the five classes are total water (vapor plus cloud liquid), cloud ice, rain, snow, and graupel. For each, there are two prognostic variables; a mass mixing ratio and a number concentration. We find that the 305 K simulation with this scheme aggregates in a qualitatively similar manner to our control simulation with the default one-moment microphysics. One difference is that the domain average OLR in the final, aggregated state is lower than with the one-moment microphysics (285 W/m^2 versus 302 W/m^2), although the domain average column relative humidity is comparable. A detailed investigation of the effect of changed microphysics is deferred to future work; we only wish to point out that self-aggregation still occurs when a more complex microphysics scheme is used.

3.5 Cold Pools

Cold pools generated by convective downdrafts have long been associated with the triggering of new convection (e.g., Emanuel, 1994). Tompkins (2001a) found that the mechanism by which cold pools organized tropical deep convection was thermodynamic; new convection was generated from the moist, high θ_e air just inside the boundary of the spreading cold pools. However, the role of cold pools in generating new convective events may be different than their role in self-aggregation. Indeed, Jeevanjee and Romps (2013) found that cold pools inhibited self-aggregation in small domains. They speculated that in small domains, cold pools are effective in homogenizing moisture and inhibiting self-aggregation because they don't need to travel far to transport moisture into the dry patch. When they eliminated cold pools, self-aggregation occurred at all domain sizes.

These findings motivate us to investigate whether the elimination of cold pools allows self-aggregation to occur at temperatures below the threshold for spontaneous self-aggregation (see Chapter 2). We perform a simulation at 300 K in which cold pools are prevented from developing by turning off the evaporation of precipitation below 1 km. Jeevanjee and Romps (2013) found that this cutoff height was sufficiently high to prevent cold pools. This modification allows the simulation to quickly self-aggregate (Figure 3-12). The evolution of precipitable water is characterized by the merger of moist blobs into progressively larger patches, until there is a single cluster. This is in contrast to the usual evolution of self-aggregation, in which a dry patch amplifies and expands until it forces all the convection to a single area (Figure 2-9). The response to moist and dry anomalies must be equivalent in the linear instability phase of aggregation; the fact that development via a dry patch is favored suggests nonlinear effects are important. Although Jeevanjee and Romps (2013) hypothesized that the underlying physics of self-aggregation was the same with or without cold pools, the preference for moist instead of dry anomalies with no cold pools may reflect a fundamentally different instability. The evolution to a single cluster in the simulation without cold pools (Figure 3-12) resembles the coarsening process described by Craig

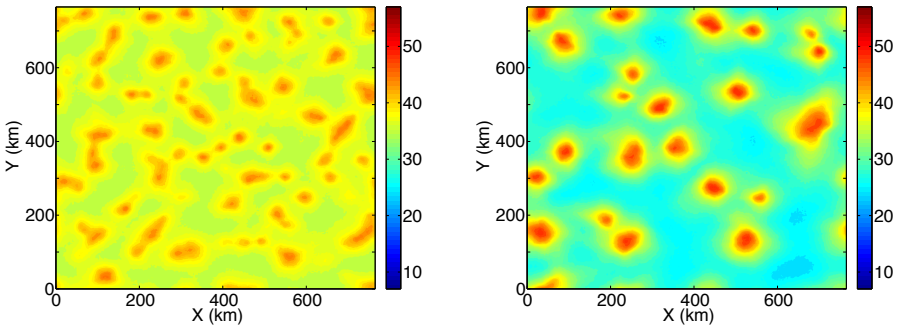

(a) Day 1

(b) Day 4

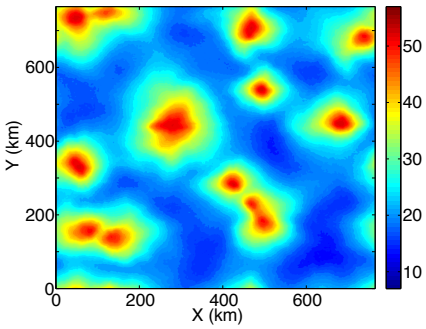

(c) Day 7

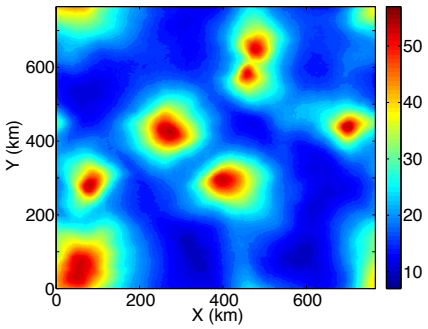

(d) Day 11

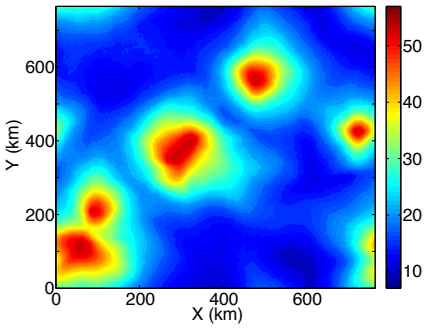

(e) Day 14

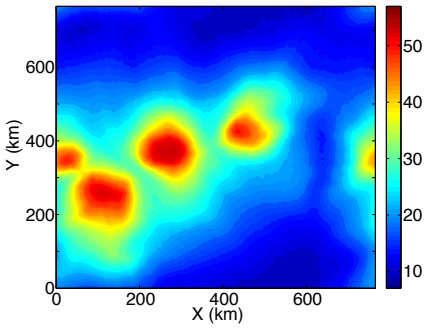

(f) Day 17

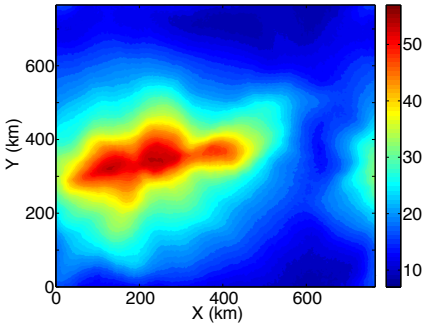

(g) Day 18

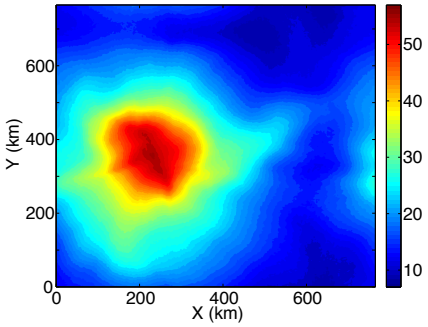

(h) Day 19

Figure 3-12: Daily average precipitable water (PW, in mm). The data are from the simulation at 305 K in which cold pools have been suppressed by eliminating evaporation of precipitation below 1 km.

and Mack (2013), which was driven by the moisture-convection feedback. However, the moisture-convection feedback pays a secondary role in the instability of the simple model developed by Emanuel et al. (2013) to describe self-aggregation.

Under normal circumstances, downdrafts driven by the evaporation of precipitation reduce the entropy of the sub-cloud layer and, assuming convective neutrality, the free tropospheric temperature. Without downdrafts, there is nothing to cool the sub-cloud layer and free troposphere, thereby reducing the effective static stability. There is therefore no resistance to large scale ascent, favoring aggregation. We propose that self-aggregation occurs quickly when cold pools are eliminated, even at a temperature below the threshold for aggregation, because we have removed the stabilizing effect of downdrafts. Furthermore, prohibiting the evaporation of precipitation in the low levels increases the precipitation efficiency. As we will review in Chapter 4, in a simple model representing the physics of aggregation, instability is favored by high precipitation efficiency (i.e., low evaporation of precipitation) (Emanuel et al., 2013).

3.6 Domain Size and Temperature

In Chapter 2, we showed that simulations at values of SST colder than 301 K and higher than 307 K did not aggregate during the period of integration (Figure 2-1, Table 2.1).[2] Experiments extending the 310 K and 312 K SST runs by 40 days still fail to aggregate (Figure 3-13). It has been shown that self-aggregation requires a large domain (Muller and Held, 2012), so one explanation for the apparent failure to aggregate at very high temperatures is that the domain size of 768 x 768 km^2 is not large enough at those temperatures. We speculate that the high SST simulations require a larger domain size, perhaps because of the large values of dry static stability that occur at high temperature. In the tropical troposphere, the temperature profile is approximately given by a moist adiabiat (Xu and Emanuel, 1989) and a moist adiabat

[2]Preliminary analysis of a simulation at 298 K with a large domain (1536 x 1536 km^2) suggests that it may aggregate. Therefore, the critical SST for aggregation may itself depend on domain size. An explanation for this is deferred to future work.

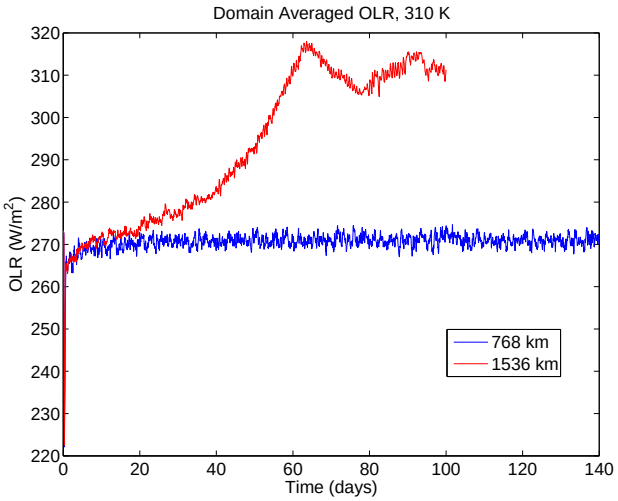

Figure 3-13: Domain averaged outgoing longwave radiation (OLR, W/m^2) for two simulations at 310 K, one with a horizontal domain size of 768 x 768 km^2 (blue), one with a horizontal domain size of 1536 x 1536 km^2.

is more stable at higher surface temperatures. We characterize the increase in the dry static stability with temperature in our simulations by computing the Brunt-Väisälä frequency, N (Equation (3.4)), from small domain (non-aggregating) simulations in radiative-convective equilibrium (Table 3.2).

$$N = \sqrt{\frac{g}{\theta_v}\frac{\partial \theta_v}{\partial z}} \tag{3.4}$$

In a self-aggregated state, ascent in the cluster is balanced by subsidence throughout the rest of the domain. With a larger static stability at higher temperatures, the compensating subsidence is weaker (in spite of enhanced radiative cooling), and thus requires a proportionally larger area to balance the same updraft. This mechanism is speculative and would obviously require rigorous analysis to be persuasive (such as a determination of how the mass flux in the cluster area changes with temperature). Nevertheless, when we reran the 310 K simulation with a domain size of 1536 $\times$ 1536 km^2 in the horizontal (4 times the area of our original domain), self-aggregation occurred (Figure 3-13). This indicates that there is a lower bound on the domain size required for aggregation that is temperature dependent. A plan view of the mature cluster in this large simulation is shown in Figure 3-14. Despite the large

Table 3.2: Dry static stability at different SSTs. Computed from the day 60 - 100 mean of small domain (96 x 96 km^2, 1 km horizontal resolution) simulations, averaged over the troposphere.

SST	N
295 K	0.0094 s^{-1}
297 K	0.0095 s^{-1}
298 K	0.0095 s^{-1}
300 K	0.0096 s^{-1}
301 K	0.0099 s^{-1}
305 K	0.0105 s^{-1}
307 K	0.0113 s^{-1}
310 K	0.0130 s^{-1}
311 K	0.0131 s^{-1}
312 K	0.0132 s^{-1}

domain size, there is still only one cluster and its size relative to the domain size is comparable to the relative size of the cluster in the lower temperature, smaller domain simulations. We note in passing that aggregation did not occur at 312 K in a 1536 $\times$ 1536 km^2 domain; evidently, an even larger domain is necessary at that high temperature (or perhaps a higher model top). One potential way of getting around the limiting domain size issue would be to replace the doubly periodic lateral boundaries with open boundaries, but that is left for future work.

The question of what determines the limiting domain size for aggregation, or, equivalently, what sets the scale of the cluster, remains unanswered. In rotating fluid dynamics, the Rossy deformation radius is a natural length scale that arises from geostrophic adjustment theory. In rotating radiative-convective equilibrium, the aggregated cluster may take the form of a tropical cyclone. Chavas and Emanuel (2014) found that, at equilibrium in axisymmetric RCE, the overall size of a tropical cyclone scales nearly linearly with V_p/f, which is the theoretical scaling for the upper bound on tropical cyclone size from Emanuel (1986). Chavas (2013) and Khairoutdinov and Emanuel (2013) noted that the size of spontaneously generated tropical cyclones in three-dimensional rotating RCE followed the same scaling reasonably well. Khairoutdinov and Emanuel (2013) additionally found that the spacing between the cyclones scaled with the deformation radius. However, in non-rotating RCE, as is

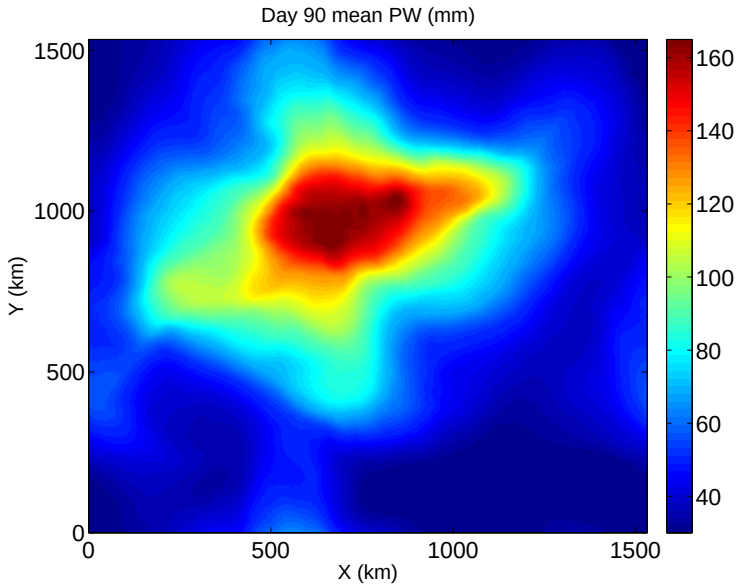

Figure 3-14: Day 90 mean precipitable water (PW, mm) for the large domain simulation at 310 K.

being examined here, there is no known natural length scale other than the size of the domain itself. Khairoutdinov and Emanuel (2012) compared self-aggregation in domains of 600 km and 1500 km (at the same SST) and found that the size of the cluster relative to the domain size was comparable, suggesting that self-aggregation does not have a limiting horizontal scale. Over a range of domain sizes and horizontal resolutions, the area of the cluster[3] is found to increase with domain size such that it is generally about 20 % of the total domain area (Caroline Muller, 2014, personal communication).

[3]Defined as the region where precipitable water is greater than one standard deviation above the domain mean value. The precise area is likely to be sensitive to this definition.

Chapter 4

Physical Mechanisms of Self-Aggregation

4.1 Analysis Framework

4.1.1 Budget for Spatial Variance of FMSE

As shown in Chapter 2, the evolution of self-aggregation is characterized by the development of a dry patch that amplifies and expands to isolate convection in a single, moist cluster. In this chapter,the physical mechanisms that are responsible for that evolution will be determined. The results of the sensitivity tests described in Chapter 3 indicated that the water vapor - longwave radiation and wind speed - surface flux feedbacks were the most important for the initiation of self-aggregation. An analysis of the various feedback terms is now performed to determine the importance of each throughout the difference stages of aggregation, as well as quantify their magnitudes.

The analysis is framed in terms of the budget of the spatial variance of vertically integrated frozen moist static energy. The frozen moist static energy (FMSE) is

[1]Sections 4.1-4.3, Figure 4-1a, and Figures 4-4 to 4-10 were published as part of Wing and Emanuel (2013), in the *Journal of Advances in Modeling Earth Systems*. The published version of the text has been adapted with a few additions for clarification, in accordance with the Creative Commons Attribution License.

conserved during moist adiabatic processes in the model, including the freezing and melting of precipitation, and is given by

$$h = c_p T + gz + L_v q_v - L_f q_{ice}, \tag{4.1}$$

where L_f is the latent heat of fusion, q_v is the water vapor mixing ratio, and q_{ice} represents all ice phase condensates. The FMSE is a desirable diagnostic of self-aggregation because its variance increases as aggregation progresses, and because its mass-weighted vertical integral can only be changed by radiation, surface fluxes, and advection. Convection redistributes FMSE but cannot change its mass-weighted vertical integral. This is useful because it would be difficult to explicitly calculate anomalies in convective heating, but we can compute the other sources and sinks of vertically integrated FMSE. We begin with the budget equation for vertically integrated frozen moist static energy, $\hat{h}$:

$$\frac{\partial \hat{h}}{\partial t} = \text{SEF} + \text{NetSW} + \text{NetLW} - \nabla_h \cdot \widehat{\vec{u}h}, \tag{4.2}$$

where SEF is the surface enthalpy flux and NetSW and NetLW are the column shortwave and longwave radiative flux convergences, respectively. The " $\widehat{\ }$ " notation indicates a density-weighted vertical integral, $\int_0^{z_{top}} [\ ] \rho dz$. The surface enthalpy flux, SEF, is defined as the sum of the latent and sensible heat fluxes, (LHF and SHF, respectively), which are given by the standard bulk formulae:

$$\text{LHF} = \rho c_E L_v U \left(q^*_{T_s} - q_v \right) \tag{4.3}$$

$$\text{SHF} = \rho c_H c_p U \left(T_s - T_a \right) \tag{4.4}$$

$$\text{SEF} = \text{LHF} + \text{SHF}. \tag{4.5}$$

In Equations (4.3) - (4.4), ρ is the air density at the lowest model level, c_E is the latent heat exchange coefficient, U is the surface wind speed, $q^*_{T_s}$ is the saturation water vapor mixing ratio at the surface temperature, q_v is the water vapor mixing ratio at the lowest model level, c_H is the sensible heat exchange coefficient, T_s is

the surface temperature, and T_a is the air temperature at the lowest model level. Hereafter, we will refer to $q^*_{T_s} - q_v$ as Δq and $T_s - T_a$ as ΔT. The column longwave radiative flux convergence is defined as

$$\text{NetLW} = \text{LW}_{\text{sfc}} - \text{LW}_{\text{top}}, \tag{4.6}$$

where LW_{sfc} and LW_{top} are the net longwave fluxes at the surface and top of atmosphere, respectively, where a positive flux is defined to be upward. In the results shown here, the column longwave flux convergence is negative everywhere, indicating that more longwave radiation is exiting the column at the top than entering it at the bottom. The column shortwave radiative flux convergence is defined as

$$\text{NetSW} = \text{SW}_{\text{top}} - \text{SW}_{\text{sfc}}, \tag{4.7}$$

where SW_{top} and SW_{sfc} are the net shortwave fluxes at the top of the atmosphere and surface, respectively, where a positive flux is defined to be downward. The column shortwave flux convergence is positive everywhere, indicating that more shortwave radiation is entering the column at the top than is exiting it from the bottom.

For an arbitrary variable A, we denote the horizontal mean as $\{A\}$ and the anomaly from the horizontal mean as A'. We subtract the horizontal mean of Equation (4.2) from the full form of the equation to obtain an equation for the time rate of change of the anomaly of vertically integrated FMSE, $\hat{h}'$. Finally, multiplying that result by $\hat{h}'$ results in a budget equation for the spatial variance of vertically integrated frozen moist static energy:

$$\frac{1}{2}\frac{\partial \hat{h}'^2}{\partial t} = \hat{h}'\text{SEF}' + \hat{h}'\text{NetSW}' + \hat{h}'\text{NetLW}' - \hat{h}'\nabla_h \cdot \widehat{\vec{u}h}, \tag{4.8}$$

in which $\hat{h}'$ indicates the anomaly of the density weighted vertical integral of FMSE and $\nabla_h \cdot \widehat{\vec{u}h}$ is the horizontal divergence of the density weighted vertical integral of the flux of FMSE. $\hat{h}'\text{SEF}'$, $\hat{h}'\text{NetSW}'$, and $\hat{h}'\text{NetLW}'$ represent the correlations of $\hat{h}'$ with anomalies in the three diabatic sources and sinks of FMSE: surface enthalpy fluxes,

column shortwave convergence, and column longwave convergence, respectively.

4.1.2 Partitioning of Surface Enthalpy Flux Anomalies

Surface enthalpy fluxes are affected primarily by variations in surface wind speed and by the thermodynamic disequilibrium between the ocean and the overlying atmosphere. We can formally decompose SEF′ into a part due solely to variations in the surface wind speed, a part due solely to variations in the air-sea enthalpy disequilibrium, and an eddy term representing variations due to the product of the two. In the model's surface flux calculation, the exchange coefficients, c_E and c_H, are calculated iteratively and vary in both space and time. An offline calculation using the surface flux code over the range of surface air temperatures, water vapor mixing ratios, and wind speeds observed in the simulations indicated that the exchange coefficients vary strongly with the surface wind speed but only weakly with the air-sea disequilibrium over the range explored. Therefore, the exchange coefficients are combined with the surface wind speed when calculating horizontal means and anomalies from those means. Each of the four variables in Equations (4.3) - (4.5), ($c_E U$, $c_H U$, Δq, ΔT), are separated into a mean and an anomaly. Substituting these definitions into Equations (4.3) - (4.5) and solving for SEF′, we find that the surface enthalpy flux anomaly can be written as

$$\begin{aligned} SEF' \;=\; & \overbrace{\rho L_v \left(c_E U\right)' \{\Delta q\} + \rho c_p \left(c_H U\right)' \{\Delta T\}}^{\text{(i)}} \\ & + \overbrace{\rho L_v \{c_E U\} \Delta q' + \rho c_p \{c_H U\} \Delta T'}^{\text{(ii)}} \\ & + \overbrace{\rho L_v \left(c_E U\right)' \Delta q' + \rho c_p \left(c_H U\right)' \Delta T' - \rho L_v \{\left(c_E U\right)' \Delta q'\} - \rho c_p \{\left(c_H U\right)' \Delta T'\}}^{\text{(iii)}} . \end{aligned} \tag{4.9}$$

Term (i) in Equation 4.9 represents the part of the SEF anomaly due solely to variations in the surface wind speed. Term (ii) represents the part of the SEF anomaly due solely to variations in the air-sea enthalpy disequilibrium. Term (iii) represents

the part of the SEF anomaly due to the product of variations in the surface wind speed and variations in the air-sea enthalpy disequilibrium, which we refer to as the "eddy term".

4.1.3 Application to Self-Aggregation

Because self-aggregation is associated with an increase in the variance of vertically integrated FMSE, processes that increase $\hat{h}'^2$ favor self-aggregation. It is then clear from Equation (4.8) that if the correlation between the anomaly of a diabatic term and $\hat{h}'$ is positive, there is either an anomalous source of FMSE in a region of already high FMSE, or an anomalous sink of FMSE in a region of low FMSE. Both of these processes represent a positive feedback on self-aggregation. The four diabatic terms in Equation (4.8), including the decomposition of SEF$'$ according to Equation (4.9), are calculated explicitly in the model at each time step and output as hourly averages, as is $\hat{h}'^2$. We calculate the horizontal convergence term, the last term in Equation (4.8), as a residual from the rest of the budget (as was done for FMSE budget calculations in Bretherton et al. (2005) and Muller and Held (2012)). We then average each term over a day and over 48×48 km^2 blocks to focus on the mesoscale organization. We sort the blocks according to their column relative humidity (from low to high), allowing us to examine how the terms evolve in moisture-time space. Because of weak temperature gradients in the free troposphere, this is essentially equivalent to ranking blocks according to $\hat{h}'$.

This analysis framework allows us to quantify and compare the feedbacks that play a role in self-aggregation. Examining each term in Equation (4.8) as a function of time and column humidity allows us to investigate both the evolution to a self-aggregated state and its maintenance. We can also explain the anomalies of each diabatic term and thereby give a physical description of each relevant mechanism. Additionally, partitioning the surface flux anomalies allows us to isolate the wind surface flux feedback from the air-sea enthalpy disequilbrium surface flux feedback. We will then be able to clearly delineate the role of surface flux feedbacks in self-aggregation. One limitation of this analysis framework is that, in calculating the

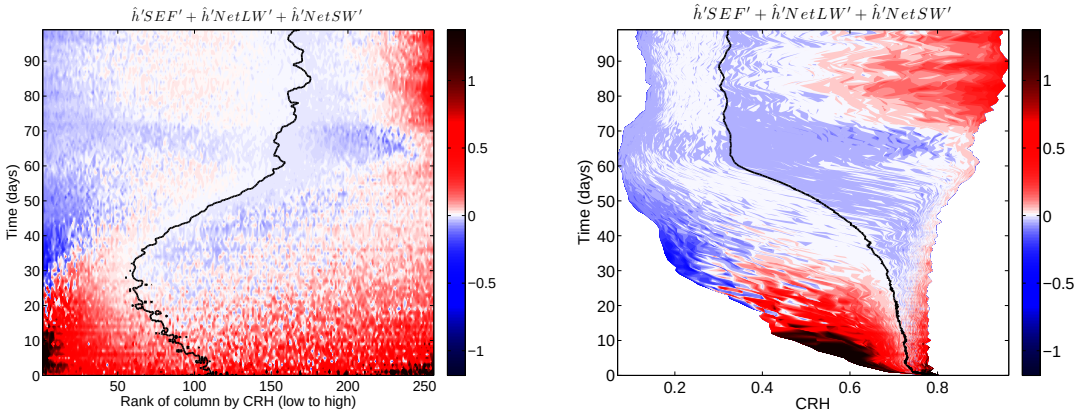

(a) (b)

Figure 4-1: Sum of all diabatic correlation terms in vertically integrated FMSE spatial variance budget, normalized at each time by $\{\hat{h}'^2\}$. Plotted as a function of time (y-axis) and moisture space (x-axis), where each term has been averaged over a day and a 48 $\times$ 48 km^2 block, has units of days^{-1}, and has been sorted according to block-averaged column relative humidity (CRH). On the x-axis, dry regions are on the left and moist regions are on the right, displayed as rank by CRH value from low to high (a) or the CRH value itself (b). Results are from the simulation at 305 K. The black line is the $\hat{h}' = 0$ contour. Note that the color bar saturates.

horizontal convergence term as a residual, we are not able to separate vertical from horizontal advection. Additionally, this framework does not explicitly quantify the moisture-convection feedback.

4.2 Results

4.2.1 Feedback Terms

In order to determine which physical mechanisms are important for both the evolution and maintenance of self-aggregation, we investigate the evolution of the various feedback terms of Equation (4.8) in both moisture and time space. First, we examine a Hovmuller plot of the sum of all the diabatic correlation terms, $\hat{h}'\text{SEF}' + \hat{h}'\text{NetSW}' + \hat{h}'\text{NetLW}'$, for the simulation at 305 K (Figure 4-1). For each day, we have normalized the diabatic correlation terms by the horizontal mean of the vertically integrated FMSE variance ($\{\hat{h}'^2\}$). Because $\hat{h}'^2$ increases with time, normalizing in this manner

makes it easier to interpret what is happening in the early stage of aggregation, when both the vertically integrated FMSE anomalies and forcing terms are small. Note that the color bar in Figure 4-1 saturates; the maximum value in the dry regions at the beginning of the simulation is 2.3 days^{-1}. The sum of all the diabatic correlation terms is positive during the first twenty days of the simulation. The strongest positive values occur in the driest regions over the first ten days. With time, these positive values diminish and propagate toward moister regions, expanding the dry patch. This evolution is consistent with our earlier observation that the dry regions expand and eventually force all the convection into one cluster. In the moist regions, positive correlations persist through the simulation.

As an aside, we point out that there are two options for displaying moisture-sorted data: as a function of the rank of the column by column relative humidity (CRH) value from low to high (Figure 4-1a) or as a function of the CRH value itself (Figure 4-1b). When plotted against CRH itself, it is obvious that the range of humidity values found in the domain increases with time. During the first half of the simulation, this is dominated by the dry regions getting drier; it so only after day 50 that the moistest regions (right edge of the Figure 4-1b) shift to higher values of CRH. For the remainder of our analysis, we display moisture-sorted data as a function of the rank of the column, as it is easier to asses what is going on at the beginning of the simulation when the range in CRH is small. Hovmuller plots of the individual terms in the $\hat{h}'^2$ budget in terms of CRH itself may be found in Appendix B.

We also note from Figure 4-1 that the sum of all the diabatic correlation terms is negative at times and places throughout the simulation; competition between positive and negative feedbacks may explain why it takes so long for the cluster to fully form. In particular, the diabatic feedback terms are negative in the dry regions from day 30 to 50, but $\hat{h}'^2$ is still increasing in those regions over that time period (Figure 4-2). This indicates that the kinematic term, involving the horizontal convergence of the vertically integrated flux of FMSE, must be playing a role. Currently, we calculate this term as a residual from the rest of the $\hat{h}'^2$ budget due to the difficulties of calculating it directly from infrequent output. The evolution of the convergence

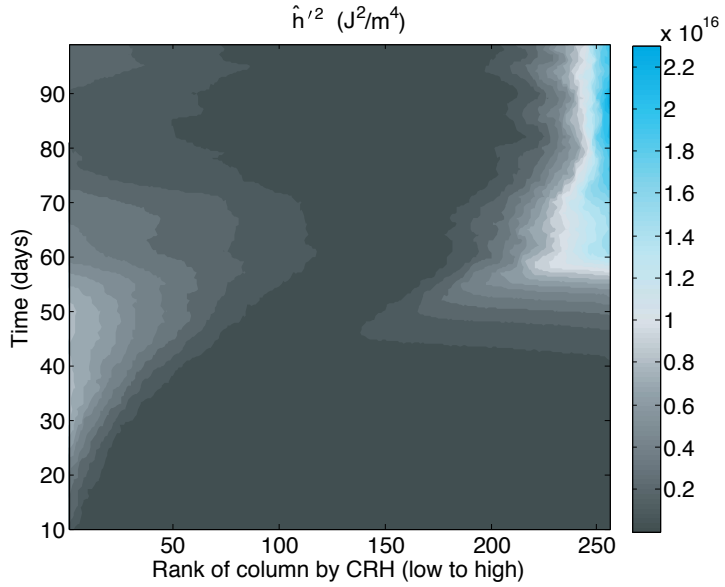

Figure 4-2: Vertically integrated FMSE spatial variance, $\hat{h}'^2$, with units of J^2/m^4. Plotted as a function of time (y-axis) and moisture space (x-axis), where it has been averaged over a day and a 48 x 48 km^2 block. On the x-axis, dry regions are on the left and moist regions are on the right, sorted according to block-averaged column relative humidity (CRH). Results are from the simulation at 305 K.

term in moisture space is shown in Figure 4-3, where it has been normalized by the horizontal mean FMSE variance ($\{\hat{h}'^2\}$). A 5-day smoother has been applied, as this term is quite noisy. The convergence feedback term is comparable in magnitude to the sum of the diabatic terms (Figure 4-1) in the $\hat{h}'^2$ budget. It is positive in the dry regions from day 20 to 50 and in the moist regions from 45 to 60. The FMSE flux convergence by the circulation thus acts as an important positive feedback in the intermediate stages of aggregation, once the dry patch has developed, by transporting FMSE from the dry regions to the moist regions. The overturning circulation between dry and moist regions is represented by the moisture-sorted streamfunction in Figure 2-13. The convergence feedback term is noisy in the moist regions during the time that there is a mature cluster (day 70-100), but it does appear to be negative in the very moistest columns (Figure 4-3). This indicates that the circulation is transporting FMSE out of the moistest columns when there is a mature cluster. The finding that the convergence term plays an important role is consistent with Bretherton et al. (2005) and Muller and Held (2012), who found that mesoscale circulations intensify

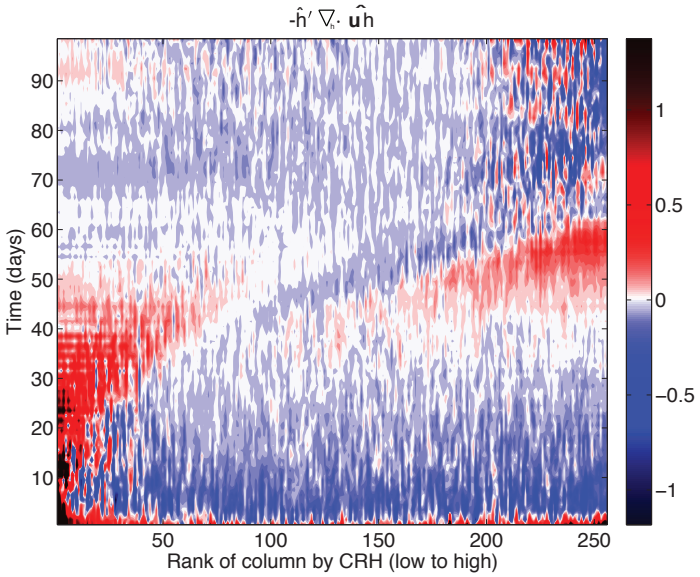

Figure 4-3: $-\hat{h}'\nabla_h \cdot \widehat{\vec{u}h}$, the term in the $\hat{h}'^2$ budget involving the convergence of the vertically integrated flux of FMSE. Calculated as a residual from the rest of the budget, this term has been normalized by $\{\hat{h}'^2\}$ and smoothed with a 5-day running mean. Plotted as a function of time (y-axis) and moisture space (x-axis), where it has been averaged over a day and a 48 x 48 km^2 block. On the x-axis, dry regions are on the left and moist regions are on the right, sorted according to block-averaged column relative humidity (CRH). Results are from the simulation at 305 K.

the later stages of self-aggregation via an up gradient transfer of moist static energy, and will not be explored further here.

The individual terms on the right side of Equation (4.8), with the surface enthalpy flux broken down into wind- and disequilbrium - dependent parts according to Equation (4.9), are shown in Figure 4-4. We have again normalized each term by $\{\hat{h}'^2\}$. The color bar in each of the plots is the same (between -1.18 days $^{-1}$ and 1.37 days $^{-1}$) to allow for easy comparison, but note that the color scale saturates in a few places. Figures 4-4a-b reinforce the notion of competition between positive and negative feedbacks, as the correlations of vertically integrated FMSE anomalies with the column radiative flux convergence anomalies are mostly positive during the first sixty days of the simulation (when the cluster is developing), while the correlations with the surface enthalpy flux anomalies are predominantly negative from day 20 to day 60. The total surface flux feedback (Figure 4-4b) is positive during the first

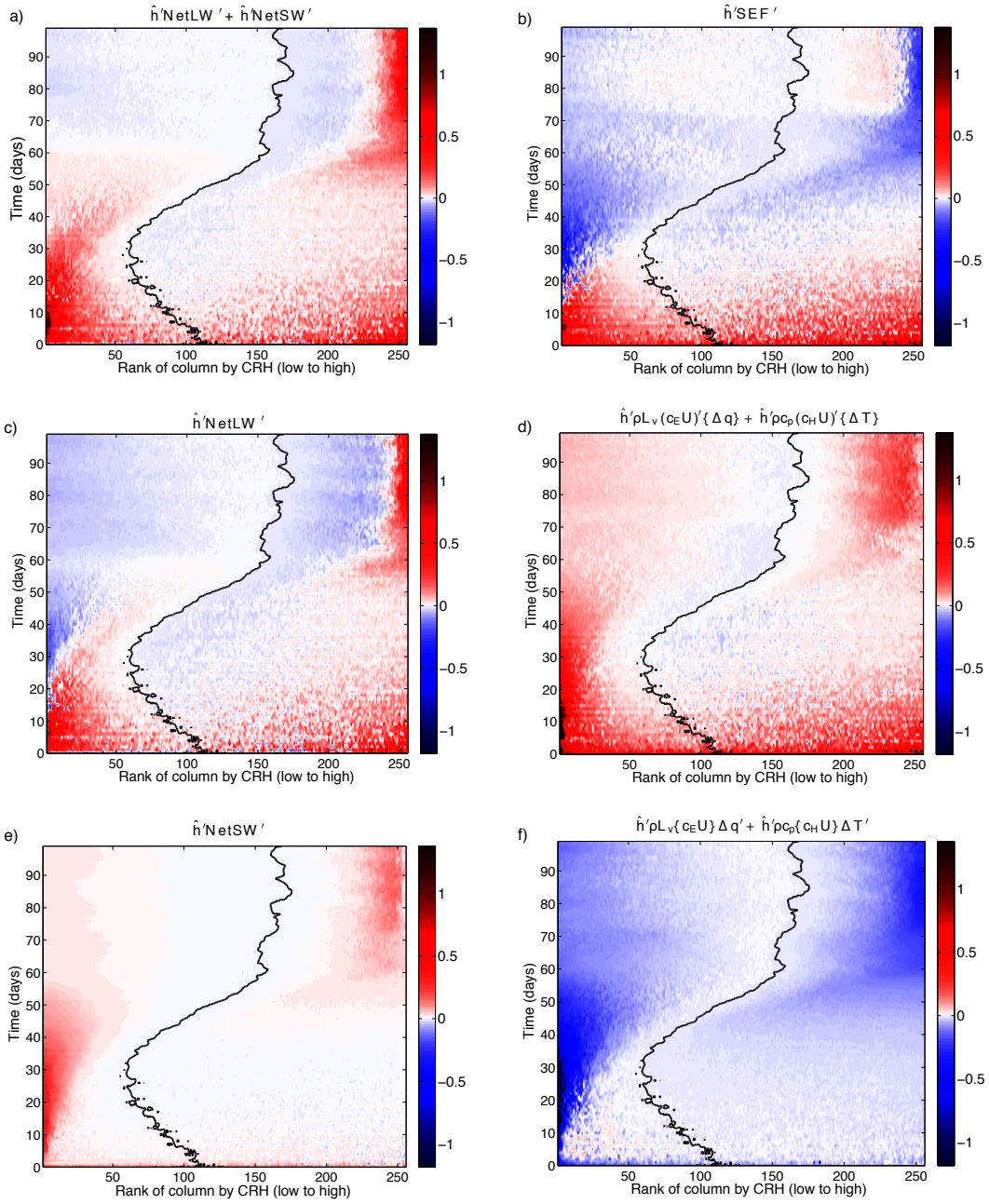

Figure 4-4: Left column: correlation between vertically integrated FMSE anomalies and column radiative flux convergence anomalies (a: column radiative flux convergence, c: column longwave convergence, e: column shortwave convergence). Right column: correlation between vertically integrated FMSE anomalies and surface enthalpy flux anomalies (b: total surface enthalpy flux anomaly, d: anomaly due to surface wind speed anomalies, f: anomaly due to air-sea enthalpy disequilibrium anomalies). All terms have been averaged over each day and over 48 $\times$ 48 km^2 blocks, normalized by $\{\hat{h}'^2\}$, are from the simulation at 305 K, and have units of days^{-1}. On the x-axis, dry regions are on the left and moist regions are on the right, sorted according to block-averaged column relative humidity (CRH). The black line is the $\hat{h}' = 0$ contour, plotted as a reference. Note that the color bar saturates in a few places.

twenty days of the simulation and is largest in the driest regions. One unexplained feature is the relatively abrupt transition around days 60 to 70.

In Figures 4-4c-f, the correlations are further decomposed. First, we examine the correlation between the vertically integrated FMSE anomalies and the column shortwave flux convergence anomalies (Figure 4-4e). This term is positive nearly everywhere, reflecting negative anomalies in NetSW in the dry regions (where $\hat{h}' < 0$) and positive anomalies in NetSW in the moist regions (where $\hat{h}' > 0$). This occurs simply because water vapor is, after ozone, the most important shortwave absorber in the atmosphere.

The sign of the correlation term involving column longwave flux convergence anomalies (Figure 4-4c) varies. In the first twenty days, the longwave term is positive, helping to amplify the developing dry patch. The column longwave flux convergence therefore must be more negative (more of a sink of energy) in the driest regions than elsewhere during that time period. Later, the longwave term is negative in the dry regions, indicating that at that time, the column longwave flux convergence must be less negative than average (less of a sink of energy) in the dry regions. Conversely, once the cluster is established (day 60 onward), the longwave term is a strong positive feedback in the moistest regions, and is the dominant contributor to the overall positive radiative feedback (Figure 4-4a) there. The physical mechanisms causing the longwave term to be a positive or negative feedback will be discussed in more detail in Section 4.3.2.

In regard to the surface flux term, we note that the correlation between vertically integrated FSME anomalies and the portion of the surface enthalpy flux anomalies that are due to wind speed anomalies (Figure 4-4d) is mostly positive. However, while the surface flux-wind feedback is a positive feedback for aggregation in our simulations, it is strongly counteracted by a negative surface flux feedback due to variations in the air-sea enthalpy disequilibrium (Figure 4-4f). Finally, while not shown here, the "eddy term" involving the correlation between vertically integrated FMSE anomalies and the product of wind speed and air-sea disequilibrium anomalies reflects that the wind speed and disequilibrium anomalies are anti-correlated. It is

Table 4.1: Dominant positive feedbacks at each stage of aggregation

Stage	Day	Feedback Term(s)
Early	0-20	Longwave Radiation, Surface Fluxes
Intermediate	20-30	Shortwave Radiation
Intermediate	30-60	Shortwave Radiation, Horizontal Convergence
Mature	60-100	Longwave Radiation

overall a negative feedback in the moist regions (where $\hat{h}' > 0$) and a positive feedback in the dry regions (where $\hat{h}' < 0$), and is the same order of magnitude but weaker than the other terms. Summing these components yields a total surface flux feedback that is positive in the early stages of aggregation, but negative most of the remainder of the simulation (Figure 4-4b).

Finally, we note that all of these components of the diabatic terms have comparable magnitude, indicating that each physical process discussed above is important for self-aggregation. Analyzing these mechanisms in the framework of an $\hat{h}'^2$ budget allows us to quantify each process throughout the entire evolution of self-aggregation. Notably, the mechanisms that amplify the initial dry patch and control the evolution to an aggregated state are not necessarily the same as those that maintain the cluster once it is established, as was also suggested by Muller and Held (2012). For example, the longwave radiative feedback is the strongest positive feedback from day 60 to 100, when there is a mature cluster. Shortwave radiation is the dominant positive diabatic feedback throughout the intermediate stage of aggregation, while longwave radiation and surface fluxes are the strongest positive feedbacks in the earliest stage (Figure 4-4). The strongest positive feedbacks in each stage of aggregation are summarized in Table 4.1.

4.2.2 Domain Mean FMSE Variance Budget

The analysis in the previous section indicated which feedbacks were amplifying or damping anomalies in a given part of the domain. In addition to examining the terms in the $\hat{h}'^2$ budget as a function of moisture space, we can also examine the domain mean budget (Figure 4-5). This allows us to determine which processes are

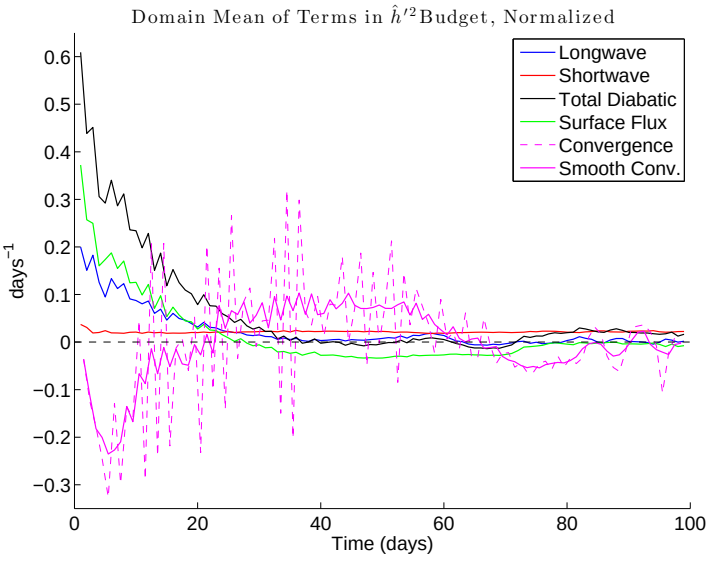

Figure 4-5: Time evolution of domain mean of terms in the $\hat{h}'^2$ budget, each normalized by $\{\hat{h}'^2\}$, with units of days^{-1}. Plotted is the sum of all diabatic correlation terms (black) and correlation between vertically integrated column FMSE anomalies and column longwave flux convergence (blue), column shortwave flux convergence (red), surface enthalpy flux (green), and horizontal convergence of flux of FMSE (pink dashed). A 5-day running average is applied to the horizontal convergence term to provide a smoothed version (solid pink). The black dashed line is the zero line, plotted as a reference.

contributing to the overall increase in domain mean FMSE variance as the system evolves to a self-aggregated state. During the instigation of self-aggregation (days 0-20), the surface flux term (green curve in Figure 4-5) contributes the largest positive tendency. It transitions to a relatively constant negative tendency in the intermediate stages before remaining close to zero during the final 20 days of simulation. Like the surface flux term, the longwave radiation term (blue curve in Figure 4-5) is large and positive in the early part of the simulation. Its magnitude decreases with time before oscillating about zero during the second half of the simulation. This is an interesting contrast to the results of the previous section, in which the longwave term was clearly the largest positive term in the moist regions when there was a mature cluster. Here, it is instead the shortwave radiation term that contributes a positive tendency to the domain mean $\hat{h}'^2$. In fact, the shortwave term is remarkably constant through out the entire simulation (red curve in Figure 4-5). The sum of the diabatic terms

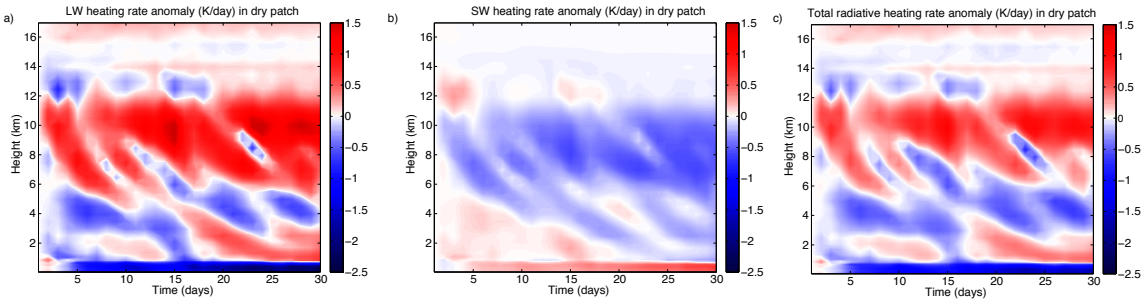

Figure 4-6: Height-time cross section of the longwave (panel a), shortwave (panel b), and total radiative heating (panel c) anomalies (K/day) over the first thirty days of the simulation at 305 K. The anomalies plotted are from an average over the 48 × 48 km^2 block that is the driest (according to column relative humidity) at day 10, and are anomalies from the profiles of longwave (a), shortwave (b), and total (c) radiative heating rates, respectively, in that block at day one.

is given by the black curve, while the contribution of the convergence term to the domain averaged $\hat{h}'^2$ budget is shown by the pink curves in Figure 4-5. The term involving the convergence of the vertically integrated flux of FMSE by the circulation is comparable in magnitude to the diabatic terms in the $\hat{h}'^2$ budget. In particular, the convergence term is positive from day 25 to 60, in the intermediate stages of self-aggregation. During this time, it amplifies vertically integrated FMSE anomalies, whereas in the early and late stages of aggregation it acts as a damping term.

4.3 Discussion of Physical Mechanisms

4.3.1 Shortwave Radiation

To focus on processes that amplify the initial dry patch, we examine time-height cross sections of the evolution of the driest block. It was shown in the previous section that the diabatic contribution to the intermediate stages of aggregation is dominated by the shortwave radiation term in the vertically integrated FMSE variance budget (Equation (4.8)), due to reduced atmospheric absorption of shortwave radiation by water vapor in the dry regions compared to the moist regions. The evolution of the shortwave heating rates in the developing dry patch is shown in Figure 4-6b. Recall that the upper troposphere dries out first (Figure 2-10). The shortwave heating rate

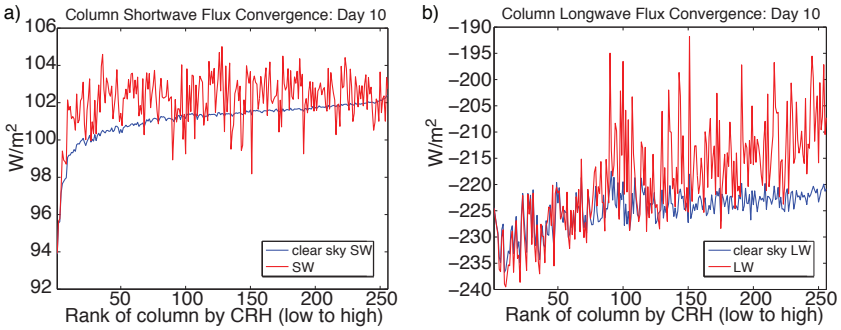

Figure 4-7: The total column shortwave(a)/longwave (b) radiative flux convergence (red) and clear sky shortwave (a)/longwave (b) column radiative flux convergence (blue). The quantities plotted have been block-averaged and sorted according to column relative humidity. The results shown here are from the day 10 mean of a simulation at an SST of 305 K.

is clearly reduced in the developing dry patch compared to its value at day one. Note that the shortwave heating rate is increased in the lower levels; this is because the reduced shortwave absorption aloft allows more of the shortwave radiative flux to reach the lower atmosphere.

Clouds are capable of modulating the response of the shortwave heating rate to the development of the dry patch. However, the clear sky column shortwave flux convergence increases nearly as much as the total column shortwave flux convergence between dry and moist regions (Figure 4-7a), which indicates that the positive shortwave feedback is mostly a clear sky effect. The same is true in the mature phase of aggregation (Figure 4-8a). In the regions where there are low clouds at day 90 (Figure 4-9), the clouds act to increase the column shortwave flux convergence, as indicated by the locations in Figure 4-8a where the value of the red curve exceeds that of the blue curve. This is likely due to atmospheric absorption of reflected shortwave radiation. In contrast, the deep clouds in the very moistest regions block solar radiation from passing through much of the atmosphere, decreasing the column shortwave flux convergence. A calculation of the shortwave feedback term, $\hat{h}'\text{NetSW}'$, using the clear sky shortwave fluxes explicitly shows that the shortwave feedback is dominated by clear sky effects throughout the evolution of aggregation (Figure 4-10a). The clear sky shortwave feedback monotonically increases towards the moister regions in the

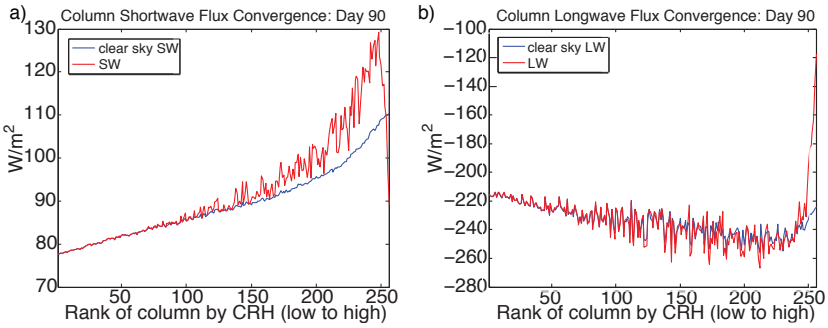

Figure 4-8: The total column shortwave (a)/longwave (b) radiative flux convergence (red) and clear sky shortwave (a)/longwave (b) column radiative flux convergence (blue). The quantities plotted have been block-averaged and sorted according to column relative humidity. The results shown here are from the day 90 mean of a simulation at an SST of 305 K.

mature phase, so the decrease in the shortwave feedback in the moistest regions in Figure 4-4e is due to clouds.

4.3.2 Longwave Radiation

The physical mechanisms controlling the longwave radiative feedback are less intuitive. Ignoring clouds for the moment, the column longwave flux convergence varies between dry and moist regions because variations in atmospheric water vapor determine variations in the longwave emissivity. To demonstrate the effect of decreasing the water vapor content of the atmosphere, we consider the behavior of the longwave radiative fluxes in a simple two-layer representation of the atmosphere (Figure 4-11a). We assume that convection maintains a constant lapse rate of 6 K/km; this, combined with a fixed surface temperature, fixes the temperatures of the two atmospheric layers. The lower layer has an emissivity ϵ_1, which we take to be larger than that of the upper layer (ϵ_2) because water vapor decreases exponentially with altitude. The net upward longwave flux at the top of the atmosphere in this representation is

$$\mathrm{LW_{TOA}} = \epsilon_2 \sigma \mathrm{T}_2^4 + (1-\epsilon_2)\,\epsilon_1 \sigma \mathrm{T}_1^4 + (1-\epsilon_2)\,(1-\epsilon_1)\,\sigma \mathrm{T}_\mathrm{s}^4, \tag{4.10}$$

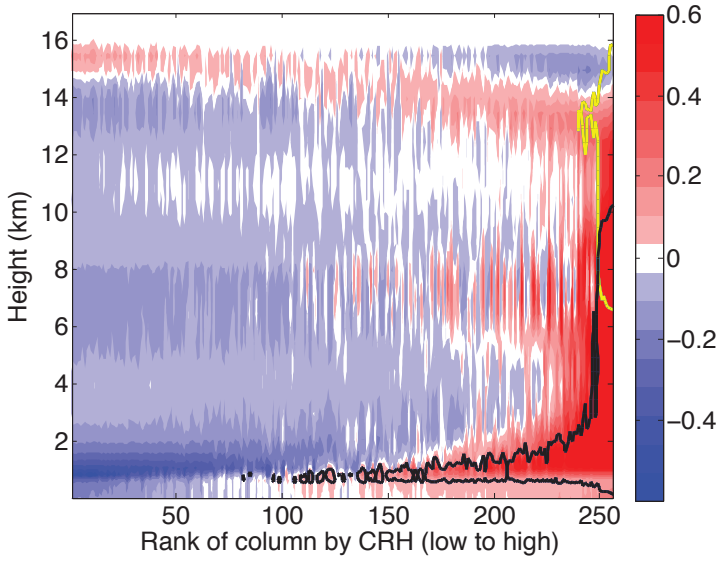

Figure 4-9: Anomalies from horizontal mean of relative humidity (shading) as a function of height and rank of column by CRH (low to high). Also plotted are the 0.01 g/kg contours of cloud ice condensate (yellow) and the 0.01 g/kg contours of cloud water condensate (black). The quantities plotted have been block-averaged and sorted according to column relative humidity. The results shown here are from the day 90 mean of a simulation at an SST of 305 K.

where σ is the Stefan-Boltzmann constant, T_s is the surface temperature, T_1 is the temperature at which the lower layer emits longwave radiation, and T_2 is the temperature at which the upper layer emits longwave radiation. The first term in Equation (4.10) is the flux upward from the second atmosphere layer. The second term is the flux upward from the first layer that is not absorbed by the second layer. The third term is the flux upward from the surface that is not absorbed by the first and second layers. The net upward longwave flux at surface is

$$\mathrm{LW_{sfc}} = \sigma \mathrm{T_s^4} - \epsilon_1 \sigma \mathrm{T_1^4} - (1 - \epsilon_1)\, \epsilon_2 \sigma \mathrm{T_2^4}. \tag{4.11}$$

The first term in Equation (4.11) is the flux upward from the surface. The second term is the flux downward from the first atmosphere layer. The third term is the flux downward from the second layer that is not absorbed by the first layer. Subtracting Equation (4.10) from Equation (4.11) gives the equation for the column longwave flux

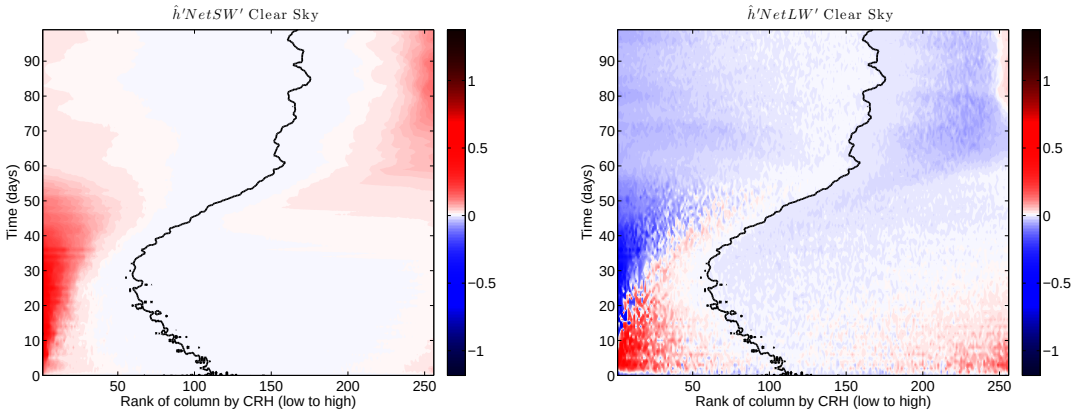

(a) Clear Sky SW Feedback (b) Clear Sky LW Feedback

Figure 4-10: Same as Figure 4-4c and Figure 4-4e, but for clear sky shortwave (a) and longwave (b) radiative feedbacks.

convergence:

$$\text{NetLW} = \sigma \text{T}_1^4 \left(\epsilon_1 \epsilon_2 - 2\epsilon_1\right) + \sigma \text{T}_2^4 \left(\epsilon_1 \epsilon_2 - 2\epsilon_2\right) + \sigma \text{T}_\text{s}^4 \left(\epsilon_1 + \epsilon_2 - \epsilon_1 \epsilon_2\right). \tag{4.12}$$

Figure 4-11b shows the dependence of Equation (4.12) on the emissivities of the upper and lower layers. The temperatures used in the calculation are 305 K, 275 K, and 245 K, for T_s, T_1, and T_2, respectively. The arrow from point A to point B is an example of a reduction in ϵ_1 and ϵ_2 that results in a decrease in the magnitude of column longwave cooling. The arrow from point C to point D also indicates a reduction in ϵ_1 and ϵ_2, but in this case, it results in an *increase* in the magnitude of column longwave cooling. Even in this very simple model the column longwave cooling is sensitive to how ϵ_1 and ϵ_2 are changed and what their value was initially. To understand the physical reason for this behavior, consider the opposing effects of decreasing the water vapor content of the upper troposphere. One effect is that decreasing the water vapor decreases the concentration of longwave emitters in the upper troposphere, which is a tendency towards less column longwave cooling. However, a decrease in the longwave emissivity of the upper troposphere also has a remote effect on the lower tropospheric longwave cooling. There is a decrease in the downward longwave flux to the lower troposphere, which reduces a source of energy for the lower troposphere and is thus a

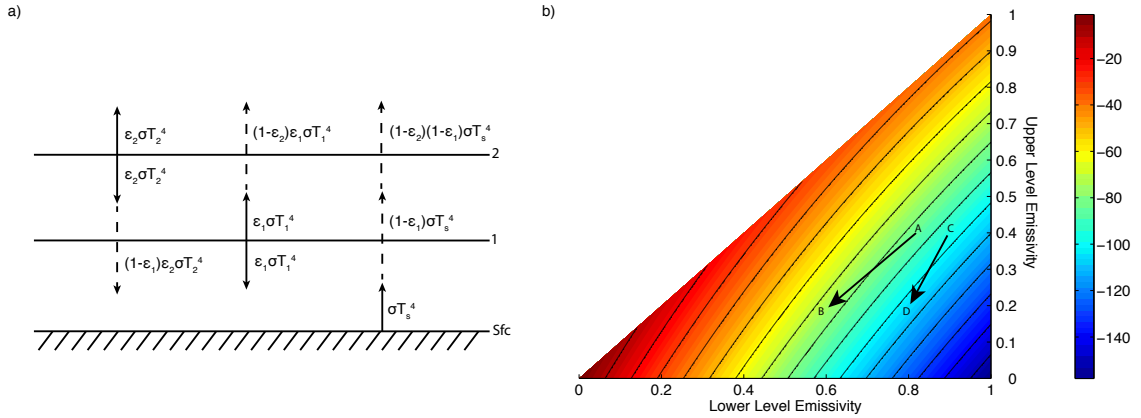

Figure 4-11: Panel a is a schematic representation of the longwave fluxes in a simple two-layer model of the atmosphere. Solid arrows represent fluxes from the indicated layer, dashed arrows represent the part of those fluxes that is transmitted through the adjacent layer(s). Panel b shows the column longwave radiative flux convergence (color contours, in W/m^2) calculated based on the schematic in panel a, as a function of the lower level and upper level emissivities. The area of the graph where the upper level emissivity is larger than the lower level emissivity is omitted because it is unphysical. The black contours also indicate the column longwave convergence, but are plotted only every 10 W/m^2 to aid in visual interpretation. The points indicated by "A", "B", "C", and "D" and the arrows connecting them show the response to a hypothetical perturbation of the emissivities.

tendency toward more longwave cooling. Additionally, more of the longwave radiation emitted by the surface and lower troposphere can escape to space through the more transparent upper troposphere, contributing to increased column longwave cooling. The balance of these opposing effects in the column integral as both the lower and upper layer emissivities change determines whether the longwave term is a positive or a negative feedback (Figure 4-4c).

During the initial stages of aggregation, the longwave feedback is positive in the driest regions. Figure 4-6a shows that there is anomalous longwave heating in the middle and upper troposphere in the dry patch compared to its value at day one, which corresponds to decreased upper tropospheric water vapor (Figure 2-10). This response is opposed by anomalous longwave cooling in the lower troposphere which is evidently large enough to cause the longwave feedback to be slightly positive initially (analogous to path C $\rightarrow$ D in Figure 4.12). Note that a positive anomaly indicates

an *decrease* in the magnitude of longwave cooling because the longwave heating rate has a negative value. The longwave heating rate anomalies in the dry patch (Figure 4-6a) are larger in magnitude than the shortwave heating rate anomalies (Figure 4-6b), so the total radiative heating rate anomalies tend to follow the pattern of the longwave anomalies (Figure 4-6c). The increased magnitude of clear sky column longwave convergence in the dry regions is similar to that of the total column longwave convergence, indicating it is primarily a clear sky, not cloud, effect (Figure 4-7b). Later in the simulation, as the dry perturbation amplifies and the lower troposphere also becomes drier, there is anomalous longwave heating of the lower levels due to the decreased low-level emissivity such that the total column longwave cooling is reduced in the dry regions (analogous to path A $\rightarrow$ B in Figure 4.12). This is represented in Figure 4-4c as a transition (around day thirty) from positive to negative values of the longwave feedback in the driest columns. A more complete description of this process, including the response of deep convection, can be found in Emanuel et al. (2013). A calculation of the longwave feedback term, $\hat{h}'\mathrm{NetLW}'$, using the clear sky longwave fluxes reveals that a large part of the positive longwave feedback at the beginning of the circulation (Figure 4-4c) is captured by the clear sky processes (Figure 4-10b). This is in contrast to the results of Muller and Held (2012), who claimed that longwave cooling at the top of low clouds in the dry region was responsible for self-aggregation. The clear sky longwave feedback does switch from positive to negative sooner than the total longwave feedback, so clouds may be important after the initiation of aggregation.

Regarding the maintenance of the cluster once it exists, the longwave feedback is strongly positive in the very moistest regions where all the deep clouds are concentrated (Figure 4-9), primarily because the column longwave cooling is strongly reduced by the longwave opacity and low temperature of high clouds. The clear sky column longwave flux convergence (Figure 4-8b) also indicates slightly reduced longwave cooling in these regions, but is not nearly as large in magnitude as the reduction of longwave cooling by high clouds. A comparison of the clear sky longwave feedback term (Figure 4-10b) to the total longwave feedback term (Figure 4-4c) emphasizes

that the positive longwave feedback maintaining the cluster is overwhelmingly a cloud effect.

4.3.3 Surface Enthalpy Fluxes

We noted in section 6 that the surface flux feedback due to variations in the surface wind speed (Figure 4-4d) was positive. The mechanism for this wind-induced surface heat exchange ("WISHE") feedback is that larger surface winds due to convective gustiness in the moist, intensely convecting regions enhance the surface fluxes there. The WISHE feedback in the early stages of aggregation is strongest in the driest regions, while from day 70 onward it is strong near the periphery of the mature cluster, (columns 200-240, in Figure 4-4b), which corresponds to the location of the strongest surface winds. In each of these two areas, the positive WISHE feedback is able to overcome the negative air-sea enthalpy disequilibrium feedback and cause the total surface flux feedback to be positive. The mechanism governing the negative air-sea enthalpy disequilbrium feedback (Figure 4-4f) is straightforward. Because the simulations have a fixed, uniform sea surface temperature and the surface enthalpy flux is dominated by the latent heat component, the air-sea enthalpy disequilibrium primarily depends on the boundary layer water vapor mixing ratio. The boundary layer water vapor mixing ratio is larger in the moist regions, where $\hat{h}'$ is positive, than the dry regions. The air-sea disequilibrium is anomalously negative in the moist regions, suppressing surface fluxes there.

4.4 Temperature Dependence

4.4.1 Insights from Feedback Analysis

The feedback analysis, as described in the preceding sections, was repeated for the other simulations that self-aggregated (301K, 303 K, 305 K, 307 K, and 310 K on a large domain). The results are qualitatively similar to those presented for the 305 K case. The magnitudes of the feedback terms, when normalized by the domain average

FMSE variance, $\{\hat{h}'^2\}$, are also comparable. For completeness, versions of Figure 4-4 (evolution of feedback terms in moisture space) for the simulations at 301 K, 303 K, 307 K, and 310 K are shown in Appendix C. There are differences in the timing of the aggregation transitions amongst the simulations at different temperatures, such as the switch of the longwave feedback term from positive to negative in the driest regions. These differences in timing are not monotonic with temperature, and as we noted in Chapter 2, random noise causes the timing of aggregation to vary as much as changing the temperature does. Therefore, comparing the results of the feedback analysis at different temperatures does little to help us understand the temperature dependence of aggregation.

It is also difficult to use this analysis framework to determine which mechanism is responsible for the temperature threshold for self-aggregation because it cannot be applied to the simulations at colder temperatures which do not aggregate. However, these results do provide several insights which, combined with the results of Emanuel et al. (2013), point to the longwave radiation feedback as the culprit. First, the sensitivity tests described in Chapter 3 indicate that the shortwave radiation feedback is not essential for self-aggregation to occur. The simulation in which the shortwave heating rate was given by a prescribed profile fixed in space in time still aggregated, as did the simulation in which the water vapor used in the shortwave radiation calculation was a fixed profile rather than the model-calculated values. Conversely, the simulations in which the longwave heating rate is fixed or the water vapor used in the longwave radiation calculation is a fixed profile do not aggregate. When we analyzed the anomalies in radiative heating rates in the developing dry patch, the anomalies in the longwave heating rates dominated the anomalies in the shortwave heating rates. Additionally, our feedback analysis showed that the longwave feedback term was larger than the shortwave feedback term in the very initial stages of aggregation. The surface flux feedback term is also an important positive feedback in the early stages of aggregation, but it is not obvious why it should be sensitive to temperature. The radiative feedbacks, on the other hand, occur because of interactions with water vapor, which depends exponentially on temperature through the

Clausius-Clapeyron equation. In particular, the fact that the longwave feedback can be positive or negative depending on the balance of opposing responses to a moisture perturbation suggests it as a candidate for explaining the temperature dependence of self-aggregation.

Emanuel et al. (2013) performed simulations with a single column model that provide further evidence that longwave radiation, rather than shortwave, is responsible for the temperature dependence of self-aggregation. They ran the single-column model into radiative-convective equilibrium with prescribed surface temperature, then ran the model in WTG (weak temperature gradient) mode. The RCE state with a humidity perturbation was used as an initial condition for the WTG run. If the WTG simulation reached a different equilibrium state than the original RCE state, the RCE state was deemed to be unstable. They performed these experiments at a range of SSTs and found that instability occurred in the simulations above 303 K. Emanuel et al. (2013) then examined the perturbation shortwave and longwave radiative heating rates in response to a reduction of specific humidity at each model level, at the different temperatures. In all cases, drying led to reduced shortwave heating. At low SST, drying led to increased longwave cooling, but at high SST, there was instead reduced longwave cooling at low-levels. The change in sign of the net radiative heating perturbation at low levels is thus due to the longwave response, not the shortwave. They also noted that the perturbation longwave cooling rates change much more than the perturbation shortwave rates do as one changes temperature, so the shortwave feedback is fractionally less important at higher temperature.

4.4.2 Linear Two-Layer Model

Emanuel et al. (2013) developed a simple theory for the RCE instability, which is manifested as self-aggregation. This simple theory consists of a two layer model that expands on the two-layer representation of longwave radiative fluxes described in Section 4.3.2. The simple model is briefly reviewed here, along with a discussion of its implications for the temperature dependence of self-aggregation.

A schematic of the two-layer model of Emanuel et al. (2013) is shown in Figure 4-

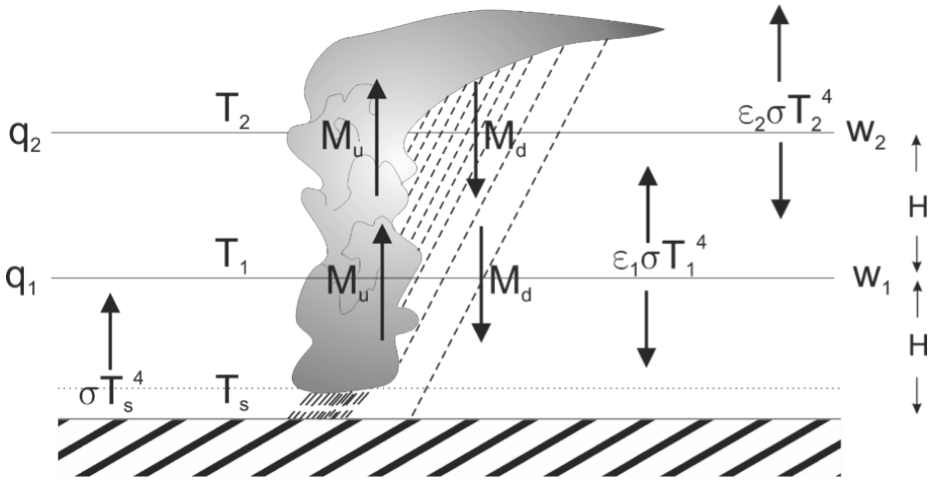

Figure 4-12: The two-layer model. Surface temperature and temperatures of each layer are specified and constant. The emissivities, ϵ, updraft and downdraft mass fluxes, M_u and M_d, large-scale vertical velocities, w, and specific humidities q, are variable. The vertical arrows depict the convective and radiative fluxes. From Emanuel et al. (2013).

12. This model represents the longwave radiative fluxes in the same way as was done in Section 4.3.2, in which the surface temperature and temperatures of each layer are specified and constant. The emissivities of each of the two layers are variable and assumed to depend on the water vapor concentrations (although the form of this dependence is not specified). As discussed in the previous section, the longwave radiative fluxes, rather than the shortwave, are expected to be responsible for the temperature dependence of self-aggregation. Therefore, shortwave radiative fluxes are neglected. We showed in Section 4.2 that the wind speed variation and air-sea disequilbrium variation components of the surface flux feedback tend to cancel; for simplicity, surface flux variations are neglected in this model. This is a somewhat questionable assumption, since the overall surface flux feedback is large and positive during the early stages of aggregation, but the two-layer model is able to become unstable without this feedback. We also showed in Section 4.4 that the radiative feedbacks in the early stages of aggregation were dominated by clear-sky effects; therefore, clouds are neglected in the simple model. In addition to radiative fluxes, the two-layer model contains convective updraft and downdraft mass fluxes, which are represented according to boundary layer quasi-equilibrium theory (Raymond, 1995;

Emanuel, 1995). In the simplest version of the model, the convective mass fluxes are taken to be the same in both layers and depend on the vertical velocity and surface enthalpy fluxes. The convective mass flux also increases with tropospheric moisture. Finally, the perturbation-scale vertical velocities are defined in each layer and are calculated according to the weak temperature gradient (WTG) approximation. In the WTG approximation, the vertical velocity is that which is necessary to hold the temperature constant at each level above the boundary layer.

The above described two-layer model is used to determine whether the feedback to an initial moisture perturbation is positive, zero, or negative corresponding to instability, neutrality, or stability. The time dependence enters through the moisture budget, which is developed through the budget of moist static energy. This is then linearized about the RCE state. This results in a linear matrix eigenvalue equation that can be solved for the linear growth or decay rate of the moisture perturbation (Equation 4.13).

$$L_v \frac{\partial q_i'}{\partial t} = -\left(\frac{\partial \bar{h}}{\partial z}\right)_i \sum_j \frac{\partial w_i}{\partial q_j} q_j' - \sum_j \frac{\partial^2 F_{ci}}{\partial z \partial q_j} q_j' + \sum_j \frac{\partial \dot{Q}}{\partial q_j} q_j'. \tag{4.13}$$

The details of the derivation can be found in Emanuel et al. (2013). Using the assumptions described above, the resulting matrix equation is

$$L_v \begin{pmatrix} \frac{\partial q_1'}{\partial t} \\ \frac{\partial q_2'}{\partial t} \end{pmatrix} = \begin{pmatrix} c_{11} & c_{12} \\ c_{21} & c_{22} \end{pmatrix} \begin{pmatrix} q_1' \\ q_2' \end{pmatrix}, \tag{4.14}$$

where the coefficients are

$$\begin{aligned} c_{11} &\equiv \frac{\partial \dot{Q}_1}{\partial q_1} \\ c_{12} &\equiv \frac{\partial \dot{Q}_1}{\partial q_2} \\ c_{21} &\equiv \epsilon_p \frac{S_2}{S_1} \frac{\partial \dot{Q}_1}{\partial q_1} + \frac{\partial \dot{Q}_2}{\partial q_1} (1 - \epsilon_p) \\ c_{22} &\equiv \epsilon_p \frac{S_2}{S_1} \frac{\partial \dot{Q}_1}{\partial q_2} + \frac{\partial \dot{Q}_2}{\partial q_2} (1 - \epsilon_p). \end{aligned} \tag{4.15}$$

The perturbations to the radiative heating depend exclusively on the dependences of the emissivities on specific humidity. All the radiative heating dependencies are negative except for the dependence of the heating of the first layer on the moisture content of the second. ϵ_p is the precipitation efficiency and S_i is the dry static stability of the RCE state (for each layer). The solutions have a growth rate of

$$\nu = \frac{1}{2L_v}\left(c_{11} + c_{22} \pm \sqrt{\left(c_{11} - c_{22}\right)^2 + 4c_{12}c_{21}}\right), \tag{4.16}$$

where the growth rate is positive if $c_{11} + c_{22} > 0$ or $c_{12}c_{21} > c_{11}c_{22}$. Instability cannot occur by the second criterion, but instability by the first criterion depends on the sensitivity of the radiative cooling of the lower layer on the emissivity (and therefore water vapor concentration) of the upper layer. This is the only positive term in the instability criterion, and is indicated by the brackets in Equation (4.17)).

$$\frac{\bar{\dot{Q}}_1}{\epsilon_1}\frac{\partial \epsilon_1}{\partial q_1} + (1-\epsilon_p)\frac{\bar{\dot{Q}}_2}{\epsilon_2}\frac{\partial \epsilon_2}{\partial q_2} + \epsilon_p \frac{S_2}{S_1}\overbrace{\frac{\sigma \epsilon_1 {T_2}^4}{\rho_1 H}\frac{\partial \epsilon_2}{\partial q_2}} > 0. \tag{4.17}$$

Instability is favored by a large dependence of the emissivity of the upper layer on its humidity and small dependence of the emissivity of the lower layer on its humidity. It is also favored by high precipitation efficiency and high emissivity of the lower layer. It is this last point that pertains to the temperature dependence. In the high temperature limit, the lower layer is opaque such that $\epsilon_1 \to 1$ and $\partial \epsilon_1 / \partial q_1 \to 0$, in which case the instability criterion becomes

$$\epsilon_p > \frac{2 - \left(\frac{T_1}{T_2}\right)^4}{\frac{S_2}{S_1}\frac{\rho_2}{\rho_1} + 2 - \left(\frac{T_1}{T_2}\right)^4}. \tag{4.18}$$

The right side of Equation (4.18) is small and positive, since $T_1 > T_2$. Therefore, in the high temperature limit, the instability criterion is easy to satisfy, which explains why self-aggregation occurs at high temperature. The instability of the two-layer model results when downward motion dries both layers. In the high temperature limit, the lower layer emissivity does not change, but the upper layer emissivity decreases.

This leads to enhanced radiative cooling of the lower layer, through the mechanism discussed in Section 4.3.2. Also, note that if only the upper layer emissivity decreases (as is true at high temperature when $\partial\epsilon_1/\partial q_1 \to 0$), the column longwave cooling increases and there is a positive longwave - water vapor feedback (Figure 4.12). The enhanced radiative cooling in the lower layer diminishes convection, leading to the cooling of both layers and reinforcing the initial downward motion and drying. In this particular model, although convection is sensitive to the free tropospheric water vapor, that sensitivity ends up canceling out and thus plays no role in the instability. In a slightly different version of the simple model, however, the sensitivity of convection to water vapor boosts the instability but cannot destabilize the model on its own. Finally, we note that as this is a linear model, the instability arise in the same manner for both drying and moistening. In our CRM simulations, the evolution of self-aggregation clearly favors the development of a dry patch, indicating the importance of non-linear effects.

Chapter 5

Conclusions and Future Directions

5.1 Summary of Results

In this work, 3-D cloud system resolving simulations of radiative-convective equilibrium were performed in a non-rotating framework, with interactive radiation and surface fluxes and fixed SST. In these simulations, interactions between the environment and convection allow convection to spontaneously organize into a single, intensely precipitating moist cluster. This process is known as "self-aggregation". Self-aggregation is found to occur only at sea surface temperatures above a certain threshold. Notably, aggregation at very high temperatures requires a larger domain size. Aggregation is characterized by several robust changes in domain-averaged quantities, including a dramatic increase in OLR and a corresponding large decrease in the column relative humidity (CRH). Unlike observations of aggregated convection in which the TOA energy budget is not significantly affected, in the simulations examined here the net TOA radiative flux decreases in magnitude (a reduction in the net downward flux). This disagreement with observations may be an artifact of the fixed SST (and resultant lack of surface energy balance) in the simulations. There is a large stochastic component of self-aggregation, with the time to aggregation varying by about twenty days when the random noise used to initialize the simulation is varied.

The evolution of the system to an aggregated state was examined. Importantly, self-aggregation begins as a dry patch that expands, eventually forcing all the con-

vection into a single clump. In particular, the upper troposphere begins drying first, but after several days the humidity throughout the troposphere in the dry patch is reduced. In the amplifying dry patch, convection quickly shuts down, clouds dissipate, and persistent subsidence develops.

Sensitivity tests suggest that wind-dependent surface fluxes and interactive longwave radiative fluxes are important for permitting self-aggregation. The dependence of the longwave radiative fluxes on spatially and temporally varying water vapor is the essential interaction. The presence of a diurnal cycle does not significantly affect self-aggregation, while the presence of a mean wind suppresses aggregation. When cold pools are eliminated by preventing low-level evaporation of precipitation, aggregation can occur below the critical SST. However, the evolution to an aggregated state is characterized by the merger of moist blobs, rather than the expansion of a dry patch, so aggregation with no cold pools may reflect a fundamentally different instability. As in previous studies (e.g., Muller and Held, 2012), we find that simulations of self-aggregation near the critical SST are sensitive to physical details such as the choice of radiation scheme. The sensitivity of aggregation to physical and numerical details may be reduced by conducting simulations with SSTs well above the threshold value, although this would compete against domain size limitations. As was shown here, a larger domain is necessary for aggregation to occur at high temperatures.

A novel approach was introduced to analyze the various physical mechanisms that play a role in the self-aggregation. Since the column radiative flux convergence and surface enthalpy fluxes are diabatic sources and sinks of vertically integrated frozen moist static energy, using a budget of the spatial variance of vertically integrated FMSE ($\hat{h}'^2$) enables a quantification of the radiative and surface flux feedbacks in a simulation that self-aggregated. Additionally, partitioning the surface enthalpy flux anomalies into a part due to surface wind speed anomalies, a part due to air-sea enthalpy disequilibrium anomalies, and an eddy term involving the product of the wind speed and air-sea disequilibrium anomalies permits a determination of the role of each separately in the surface flux feedback.

A key finding is that all the terms in the $\hat{h}'^2$ budget are of similar magnitude, so

shortwave radiative feedbacks, longwave radiative feedbacks, and surface flux feedbacks are all important for self-aggregation. Multiple mechanisms work together to permit the convection to aggregate; it is truly an interplay between convection, radiation, moisture, and circulation. The shortwave radiative feedback is a key positive feedback throughout the evolution of self-aggregation and is due to increased absorption of water vapor by atmospheric water vapor in the moist regions compared to the dry regions. The longwave radiative feedback is initially a positive feedback in the dry regions, but is later negative (in both cases, due mostly to clear sky effects). This is because the response of longwave cooling to a dry perturbation has two opposing effects, the net result of which varies in both space and time in our simulations. The positive longwave feedback in the early stages of aggregation is primarily a clear sky effect, in which decreased humidity causes enhanced longwave cooling of the atmosphere, which suppresses convection in the dry regions. The surface flux feedback is negative throughout much of the simulation, due to a strongly negative surface flux-enthalpy disequilibrium feedback, which is only partially counteracted by a positive surface flux-wind (WISHE) feedback. Without the WISHE feedback, which is of comparable magnitude to the radiative feedbacks, the total surface flux feedback would be very strongly negative (perhaps negative enough to prevent, or at least, slow down, self-aggregation). In the early stages of aggregation, however, the negative disequilbrium feedback does not develop as quickly as the positive WISHE feedback does, leading to a positive overall surface flux feedback. In the intermediate stages of aggregation, the column integrated convergence of the FMSE flux by the circulation also plays an important role. In contrast to the evolution of self-aggregation, during which all the different feedbacks are relevant, the longwave radiation-cloud feedback dominates in maintaining the cluster once it is formed. This important distinction between feedbacks that maintain a cluster, and feedbacks that establish one, point to the limitations of mechanism denial studies. The approach taken here is valuable because it elucidates the relevant feedbacks during all stages of aggregation.

The sensitivity tests and results of the feedback analysis point to the longwave radiation, rather than shortwave, as the most likely cause of the temperature depen-

dence of self-aggregation. Indeed, these results combined with those of a companion study (Emanuel et al., 2013) reveal that the temperature dependence is due to the longwave feedback term and enters through the longwave opacity of the lower troposphere. This is a function of the lower tropospheric water vapor which, in turn, depends on temperature. Radiative-convective equilibrium becomes unstable at high surface temperatures, which is demonstrated in a simple two-layer model by Emanuel et al. (2013). The instability results because, at high temperature, the emissivity of the lower troposphere is large enough (due to high water vapor concentration) that variations of its radiative cooling depend primarily on variations in upper tropospheric water vapor. This fundamental instability is manifested as the self-aggregation of convection in 3D simulations. Our results also suggest that, while moisture-convection feedbacks may enhance the instability, they may not be sufficient by themselves to cause it.

5.2 Implications and Directions for Future Research

5.2.1 Climate Models and Convective Parameterizations

Organized tropical convection is responsible for much of the rainfall and cloudiness in the tropics, yet is poorly represented in climate models. To the extent that the physics of self-aggregation is important to phenomena such as tropical cyclones and the Madden-Julian Oscillation, inaccurate treatment of such physics may affect the ability of models to properly simulate these phenomena. Furthermore, the degree of convective aggregation has a dramatic impact on the cloudiness, humidity, and radiative fluxes over the surrounding environment, in both cloud resolving simulations and observations. Therefore, the lack of organized convection in climate models may compromise their simulation of cloud and water vapor feedbacks and climate sensitivity. In particular, if the degree of aggregation increases as the climate warms, the consequent reduction in relative humidity would weaken the water vapor feedback. A change in the degree of aggregation could also impact the large-scale circulation,

as hypothesized by Tobin et al. (2013).

The ability of different models to simulate self-aggregation of convection depends on their representation of the physics underlying the RCE instability. We showed that the initiation of self-aggregation was driven by feedbacks between water vapor and radiation, and that these feedbacks were primarily clear-sky effects. These interactions should be easily simulated by the radiation schemes used in weather and climate models. However, the surface flux feedback was also an important positive feedback in the early stages of aggregation, and this depends on the inclusion of convective gustiness in the models surface flux calculation. Some convective schemes do not include this effect and therefore may be missing an important positive feedback. The Emanuel and Zivkovic-Rothman (1999) convection scheme, which was used in the single-column model experiments of Emanuel et al. (2013), is an example of a scheme that does produce a gustiness factor that is incorporated into the surface flux calculation. Finally, the instability also depends on the response of deep convection to drying, which is likely to vary across different convection schemes. Tobin et al. (2013) suggest that the inclusion of a prognostic variable describing the aggregation state of convection may be necessary for convective parameterizations to reproduce the modulation of environmental variables by aggregated convection. To implement this, more research is needed on how aggregation modulates the interaction between convection and the environment (for example, the modification of entrainment rates or precipitation efficiency by the amount of aggregation).

5.2.2 Climate Sensitivity

Another potential implication of self-aggregation is regarding climate sensitivity. If increased aggregation in a warmer climate were to decrease the relative humidity, this could weaken the water vapor feedback and reduce climate sensitivity. Additionally, Tobin et al. (2013) proposed that convective aggregation may act as a "convective regulating mechanism", by affecting couplings between convection, radiation, and large-scale ascent and between convection and moisture. While our results indicate that self-aggregation is favored by increased surface temperature, it is not known how

global aggregation statistics would change with warming. A dramatic decrease in the humidity of the environment is seen in cloud resolving simulations that aggregate, but these limited domain, homogeneous simulations do not have much horizontal mixing of water vapor. Horizontal mixing of water vapor in the real atmosphere by wave disturbances, wind shear, and the large scale circulation might reduce the sensitivity of humidity to convective aggregation. Running global models in radiative-convective equilibrium (as in, for example, Held et al. (2007)) may be a useful way of investigating these issues.

In rotating RCE simulations, Khairoutdinov and Emanuel (2012) found that the presence of tropical cyclones decreases the climate sensitivity of the RCE state. They estimated climate sensitivity by computing the change of the net TOA flux for a given change in SST, for simulations that spontaneously formed tropical cyclones and those that did not. Similarly, examining the change in domain average OLR (Figure 2-1)) with SST for the simulations performed here indicates that OLR increases more with SST for the aggregated simulations than the disaggregated ones. It is not clear what exact mechanism would cause a decrease in climate sensitivity with aggregation; it could be related to a decreased water vapor feedback because of the relative humidity reduction, or perhaps a change in the lapse rate feedback. More research is needed to determine the link between aggregation and climate sensitivity; as of now, it is highly speculative.

5.2.3 Madden-Julian Oscillation

The Madden-Julian Oscillation is one of the more likely real-world phenomenon in which self-aggregation physics could be playing a role. SST gradients and wind shear are weak over the Indian Ocean/ western Pacific warm pool, where the MJO is the dominant disturbance, so there is an opportunity for other organizing mechanisms to occur. Numerous studies have suggested that processes that alter the column integrated moist static energy are essential to the MJO (e.g., Raymond and Fuchs, 2007; Sobel et al., 2008; Maloney, 2009). Such processes include surface enthalpy fluxes (e.g., Sobel et al., 2008) and interactions between moisture and radiative heating

(e.g., Bony and Emanuel, 2005). These are the exact same processes that control self-aggregation. Self-aggregation could be described as the result of feedbacks between moist convection and sources of column moist static energy that cause the atmosphere to be unstable to perturbations in the column moist static energy. Sobel and Maloney (2012) proposed an idealized framework for modeling the MJO that resonates with this description of self-aggregation. They hypothesized that the MJO was a moisture mode in which thermodynamic feedbacks involving sources and sinks of column moist static energy were important energy sources. In a modified framework, Sobel and Maloney (2013) found that eastward propagating modes (as the MJO is) can only be unstable because of cloud-radiative feedbacks, which are also important in the maintenance of self-aggregation. It is therefore possible that the MJO is self-aggregation on an equatorial beta plane. The potential for self-aggregation physics to be important in the initiation and maintenance of the MJO is one of the most promising applications of this work to tropical convective variability in the real world.

5.2.4 Finite Amplitude Perturbation

The radiative-convective instability described here and in Emanuel et al. (2013) could be characterized as a subcritical bifurcation of the RCE state. In such a regime, the RCE state is stable to small amplitude perturbations below the critical SST. Sufficiently large perturbations, however, may transition the state to a state with upward motion and deep convection in one part of the domain and dry, subsiding air in the rest of the domain. The existence of multiple equilibria of RCE was first pointed out by Raymond and Zeng (2000) and subsequently described by Sessions et al. (2010) and Sobel et al. (2007). Above the critical SST, the RCE state is unstable and the transition is spontaneous, corresponding to self-aggregation. A subcritical bifurcation of the RCE state was first proposed by Emanuel and Nolan (2004). We have focused on what happens above the critical SST, but have not investigated the subcritical state. As noted in Chapter 1, when rotating dynamics are enabled, the self-aggregated cluster may take the form of a tropical cyclone. Nolan et al.

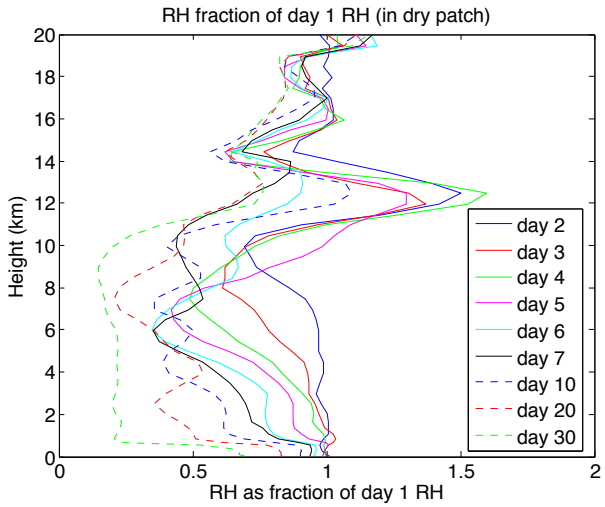

Figure 5-1: Relative humidity as a fraction of the relative humidity profile at day 1, averaged over the area that is the driest 48 x 48 km^2 block at day 10 of the 305 K simulation.

(2007) demonstrated that tropical cyclogenesis occurs below the critical temperature if a finite amplitude perturbation is introduced. Whether the same occurs for non-rotating aggregation is an unanswered question.

The hypothesis that self-aggregation represents a subcritical bifurcation of the RCE state could be tested by inserting a finite amplitude moisture perturbation into a simulation that is below the critical SST. Self-aggregation has been shown to exhibit hysteresis (Khairoutdinov and Emanuel, 2010; Muller and Held, 2012). Muller and Held (2012) found that when initialized with a moist bubble rather than white noise, the horizontal resolution dependence of aggregation disappears. This approach assumes an aggregated state from the beginning. In order to capture the instability process that leads to self-aggregation, one could insert a dry patch into a simulation below the critical SST. This would mimic the evolution of self-aggregation discussed in Chapter 2. The structure of this dry patch would be inspired by the dry patch that develops in the simulations that do aggregate. For example, Figure 5-1 shows the relative humidity averaged over the area that is the driest 48 x 48 km^2 block at day 10 of the 305 K simulation, as a fraction of the relative humidity profile at day 1. Large relative humidity reductions develop early in the simulation and are initially largest in the upper troposphere before amplifying and shifting downwards. By day 10, the

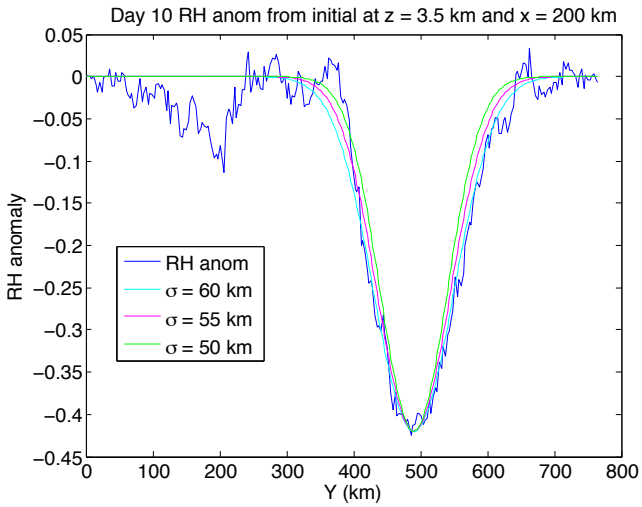

Figure 5-2: Anomaly of relative humidity at day 10 from the initial relative humidity profile, for the 305 K simulation. A cross section at X = 200 km of the RH anomaly at 3.5 km is plotted in the blue curve. The cyan, pink, and green curves are Gaussians with different standard deviations.

humidity perturbation is relatively uniform with height in the troposphere (which motivated the uniform humidity reduction experiments of Emanuel et al. (2013)). The relative humidity perturbation that is inserted into a non-aggregated simulation would be inspired by these profiles, but would be a simpler function of height, so that the sensitivity to the shape of the profile can be easily tested. It is preferable to apply the relative humidity perturbation in terms of a fraction of the existing humidity, (rather than a difference), to avoid accidentally causing a negative specific humidity. A simple Gaussian would be an appropriate horizontal structure for the moisture perturbation, based on the dry patch in the self-aggregating simulations (Figure 5-2). This moisture perturbation could be applied to the existing water vapor field part way through non-aggregating simulation. Applying the perturbation several days into the simulation rather than initializing with it will make it easier to quantify the feedback processes that cause the perturbation to decay or grow, using the analysis framework described in Chapter 4. Sensitivity tests in which the magnitude of the perturbation is varied could yield insights regarding how large of a perturbation is necessary to push the system into the aggregated state, and whether the necessary magnitude depends on temperature. These simulations could also help determine the

lower limit of the subcritical bifurcation and if there is a lower SST threshold below which transition to the aggregated state is impossible.

5.2.5 Tropical Cyclogenesis

One particularly dramatic example of the importance of cloud clusters is their role as precursors of tropical cyclones. The problem of tropical cyclogenesis remains poorly understood. In recent years, however, the marsupial pouch paradigm has emerged as a promising theoretical framework for tropical cyclogenesis. In this paradigm, genesis tends to occur near the critical layer of a tropical wave (Dunkerton et al., 2008). The wave critical layer is a region of closed circulation that is favorable for the development of a tropical cyclone, as the incipient disturbance is protected from potentially adverse conditions in the surrounding environment. Dunkerton et al. (2008) point out that the pouch region is a preferred region for genesis not only because it is protected from the entrainment of dry air from the environment but also that convection in the pouch repeatedly moistens the column. The idea of preservation of a moist area that is favorable for convection is also fundamental to the phenomenon of self-aggregation. This suggests that the mechanisms underlying self-aggregation may also be relevant to understanding tropical cyclogenesis.

One direction for future work is to investigate the role of convective self-aggregation in spontaneous tropical cyclogenesis by extending the analysis framework established here to cloud resolving simulations in rotating radiative-convective equilibrium. Previous studies of rotating radiative-convective equilibrium have examined the sensitivity of tropical cyclogenesis and tropical cyclone intensity, size, and frequency to environmental parameters (Nolan et al., 2007; Held and Zhao, 2008; Khairoutdinov and Emanuel, 2013). Nolan et al. (2007) suggested that the initial development of a broad circulation in a case of spontaneous tropical cyclogenesis was due to the same radiative-convective feedbacks that cause non-rotating self-aggregation. Performing the feedback analysis as described in Chapter 4 would allow comparison between the spontaneous genesis of a tropical cyclone and the development of a non-rotating self-aggregated cluster.

5.2.6 Self-Aggregation in an Inhomogeneous Environment

The simulations studied here were constructed in a very idealized manner; there was no large scale forcing and no mean wind. This was by design because we sought to eliminate any external factors and isolate the effect of convection interacting with the environment. However, these idealizations limit the applicability of our results to the real world, since in nature there are large-scale circulations and asymmetries that affect convective organization. Therefore, one extension of this work would be to study the mechanisms of convective organization in more realistic cloud resolving simulations with asymmetries such as forcing a wave disturbance to pass through the domain and imposing vertical wind shear.

A wave disturbance passing through the domain may help generate convective organization; for example, Frank and Roundy (2006) showed that tropical waves play a significant role in the formation of tropical cyclones by enhancing low-level convergence and low-level rotation. The same frozen moist static energy variance analysis as described above may be used to analyze the feedbacks under these circumstances and determine what role, if any, the radiative-convective feedbacks that drive spontaneous aggregation play when there is external forcing applied.

Rappin et al. (2010) studied tropical cyclogenesis in rotating radiative-convective equilibrium with shear and noted that shear suppressed aggregation. Regarding non-rotating radative-convective equilibrium, Robe and Emanuel (2001) demonstrated that vertical wind shear causes convection to become organized into lines. However, they used a specified, constant radiative cooling rate, which prevented the type of aggregation examined here. It would be interesting to investigate how the feedbacks that lead to self-aggregation are modified when wind shear is applied. If wind shear does suppress self-aggregation, an potential avenue of research would be to apply shear to a simulation that has already aggregated and examine the physical mechanisms controlling the break up of the aggregated cluster under those circumstances. In previous studies, self-aggregation has been found to exhibit strong hysteresis (Muller and Held, 2012; Khairoutdinov and Emanuel, 2010), so it would be informative to

determine what is required to disaggregate an existing cluster.

Appendix A

Surface Flux Exchange Coefficients

The surface fluxes of sensible and latent heat between the sea surface and atmosphere in SAM (Khairoutdinov and Randall, 2003) are computed using Monin-Obukhov similarity. The sensible and latent heat exchange coefficients, c_H and c_E, respectively, are calculated iteratively and vary in both space and time. The surface flux calculation depends on the bottom level pressure, bottom level wind speed, bottom level specific humidity, bottom level temperature, bottom level height above surface, and sea surface temperature. Of these, bottom level height above surface and sea surface temperature are external parameters that are constant. The bottom level pressure that is used in the surface flux calculation varies only slightly. This leaves bottom level wind speed, bottom level specific humidity, and bottom level temperature as the variables that control the variation in the exchange coefficients.

We vary these quantities over a reasonable range of values in an offline calculation using SAM's surface flux code. From a snapshot at day 100 of the simulation at 305 K, we estimate reasonable values for each variable needed as an input to the surface flux code (Table A.1). Note that although bottom level wind speeds as low as $0.0104\,m/s$ are found in this snapshot, the model uses a minimum wind speed of $1\,m/s$ in its surface flux calculation. We successively vary T_{bot}, q_{bot}, and U, while holding one out of the three fixed at its horizontal mean. The results are shown in Figure A-1. Although it is q_{bot} and T_{bot} that we vary, we plot c_H and c_E as a function of Δq and ΔT. It is these air-sea disequilbria that are relevant in our surface flux

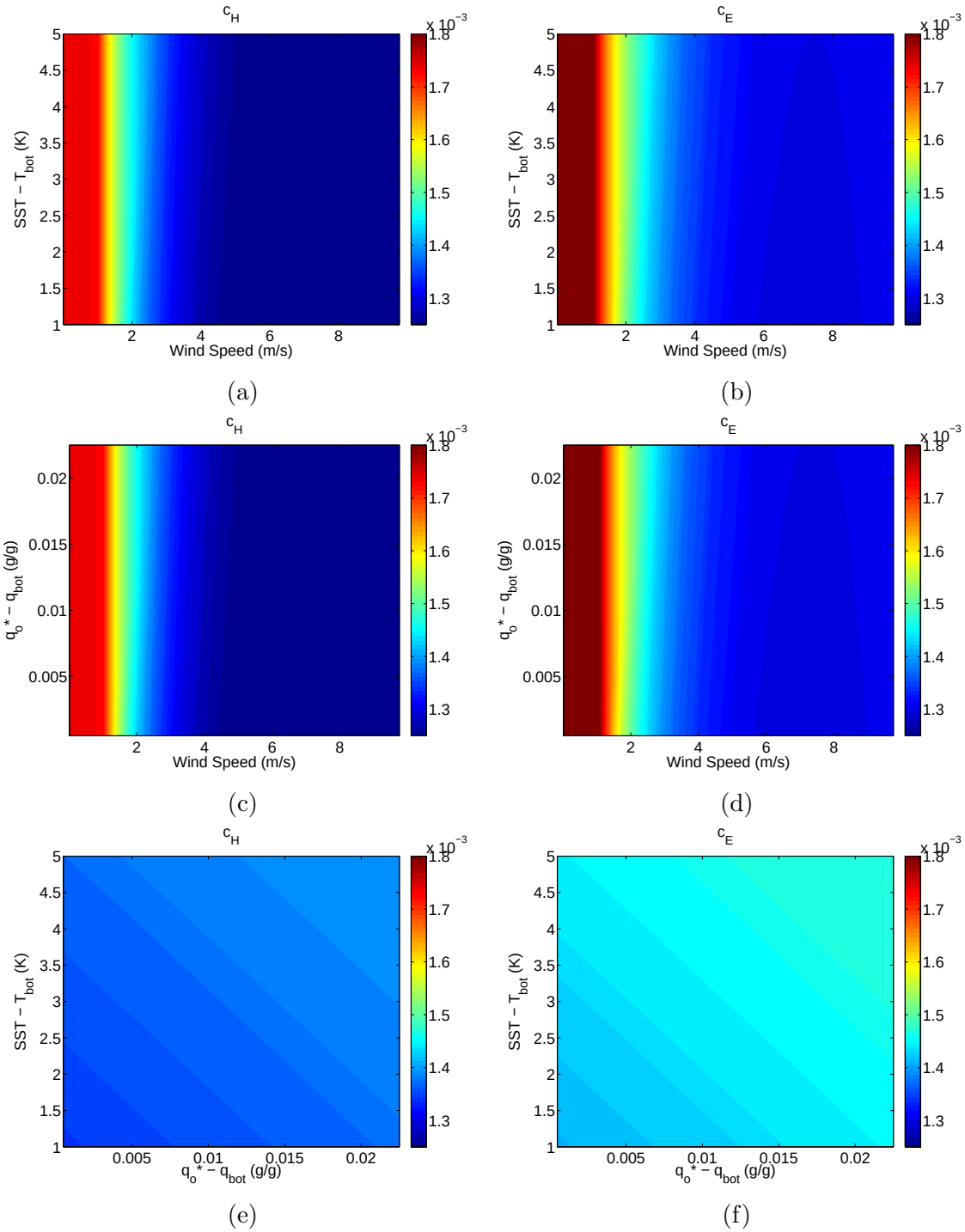

Figure A-1: Variation in sensible and latent heat exchange coefficients (c_H and c_E, respectively). Top row: T_{bot} and U varied, q_{bot} held fixed. Middle row: q_{bot} and U varied, T_{bot} held fixed. Bottom row: T_{bot} and q_{bot} varied, U held fixed.

Table A.1: Inputs to Surface Flux Calculation

Variable	Value(s)	Description
SST	305 K	Sea Surface Temperature
z_{bot}	$37\,m$	Bottom level height above surface
P_s	$1007.8\,mb$	Bottom level pressure
T_{bot}	300 K : 304 K	Bottom level temperature
q_{bot}	$0.008\,g/g$: $0.03\,g/g$	Bottom level specific humidity
U	$0.01\,m/s$: $10\,m/s$	Bottom level wind speed

partitioning (see Chapter 4). It is evident that the exchange coefficients depend strongly on the surface wind speed (Figure A-1a-d)[1]. When Δq and ΔT are varied, the exchange coefficients vary over a much smaller range of values. Note that if the sea surface temperature was allowed to vary, we might expect a stronger dependence on ΔT (i.e., if the air-sea temperature disequilibrium changed sign). c_H and c_E differ slightly and c_H is generally smaller than c_E (compare left and right columns of Figure A-1). Figure A-2 shows the difference between c_H and c_E as U, T_{bot}, and q_{bot} are varied. This difference is between one and two orders of magnitude smaller than the values of c_H and c_E themselves, and is largest at low wind speeds.

Based on these results, we ignore the dependence of c_H and c_E on the air-sea disequilibrium. We combine c_H and c_E with the surface wind speed when calculating the surface flux anomalies (see Equation (4.9)). Although the above results show that c_H and c_E are close in magnitude, we calculate the sensible and latent heat flux anomalies separately, and thus take into account the difference between c_H and c_E.

[1]Despite the axis on the plot ranging between 0 and 9 m/s, because the minimum wind speed in the surface flux calculation is 1 m/s, there is no variation of the exchange coefficients plotted below that value.

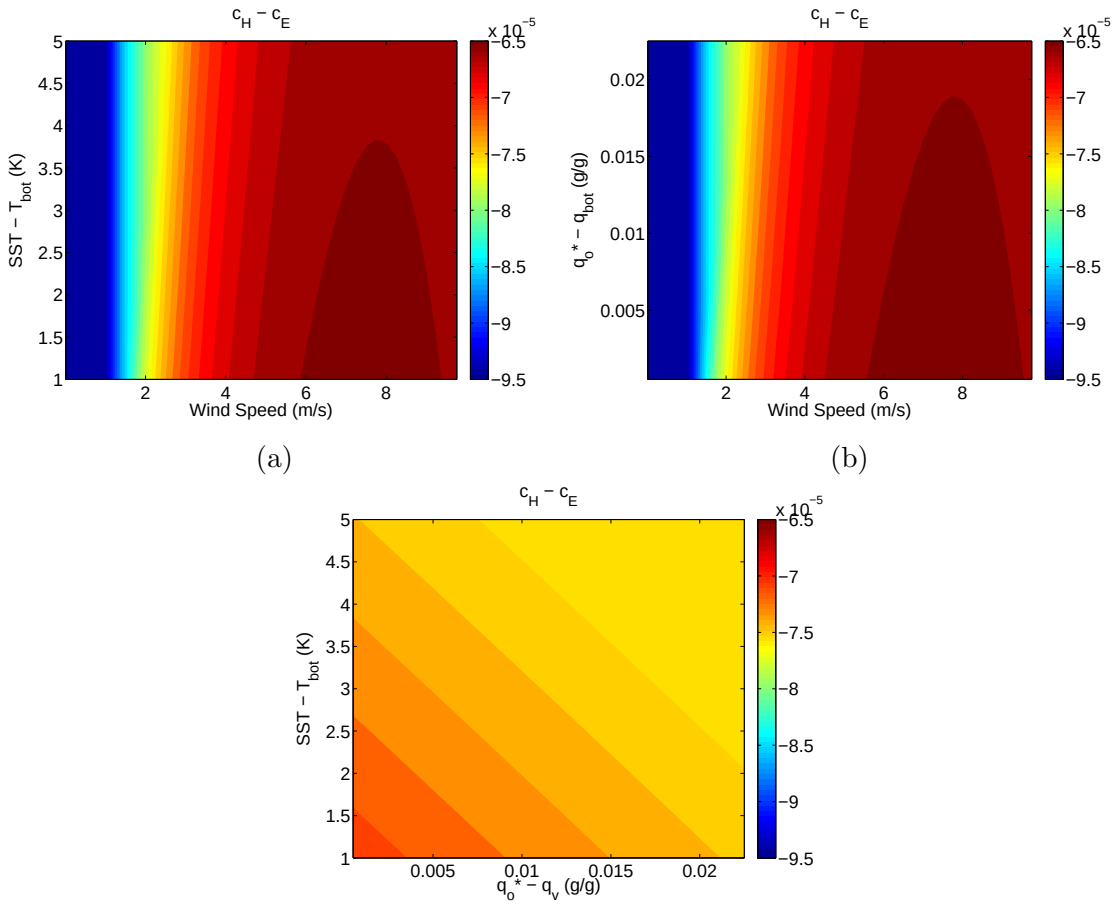

Figure A-2: Difference between sensible and latent heat exchange coefficients when U, T_{bot}, and q_{bot} are varied.

Appendix B

FMSE Variance Budget as a Function of CRH

In Chapter 4, we introduced a novel method for quantifying the magnitudes of the feedbacks that control self-aggregation within the framework of the budget for the spatial variance of column-integrated frozen moist static energy $\left(\hat{h}'^2\right)$. We averaged each term over a day and 48 x 48 km^2 blocks, and then sorted those blocks according to their values of column relative humidity (CRH). We analyzed each feedback term in moisture-time space by plotting them as a function of the rank of each column, according to its CRH value. However, it is also informative to plot each term against the actual CRH values that correspond those ranks. Therefore, as a complement to Figure 4-4, the individual terms in the $\hat{h}'^2$ budget are displayed as a function of time and CRH in Figure B-1. We re-calculate the moisture-sorting function for each day; therefore, the CRH value of any given rank changes with time, as does the ordering of the columns. While this is hidden in Figure 4-4, it is obvious in Figure B-1. Plotting against CRH itself emphasizes the expansion of the dry patch. Figure 4-4, however, better indicates the amount of area covered by positive or negative feedbacks, in addition to emphasizing the early stages of aggregation when the range in CRH is small.

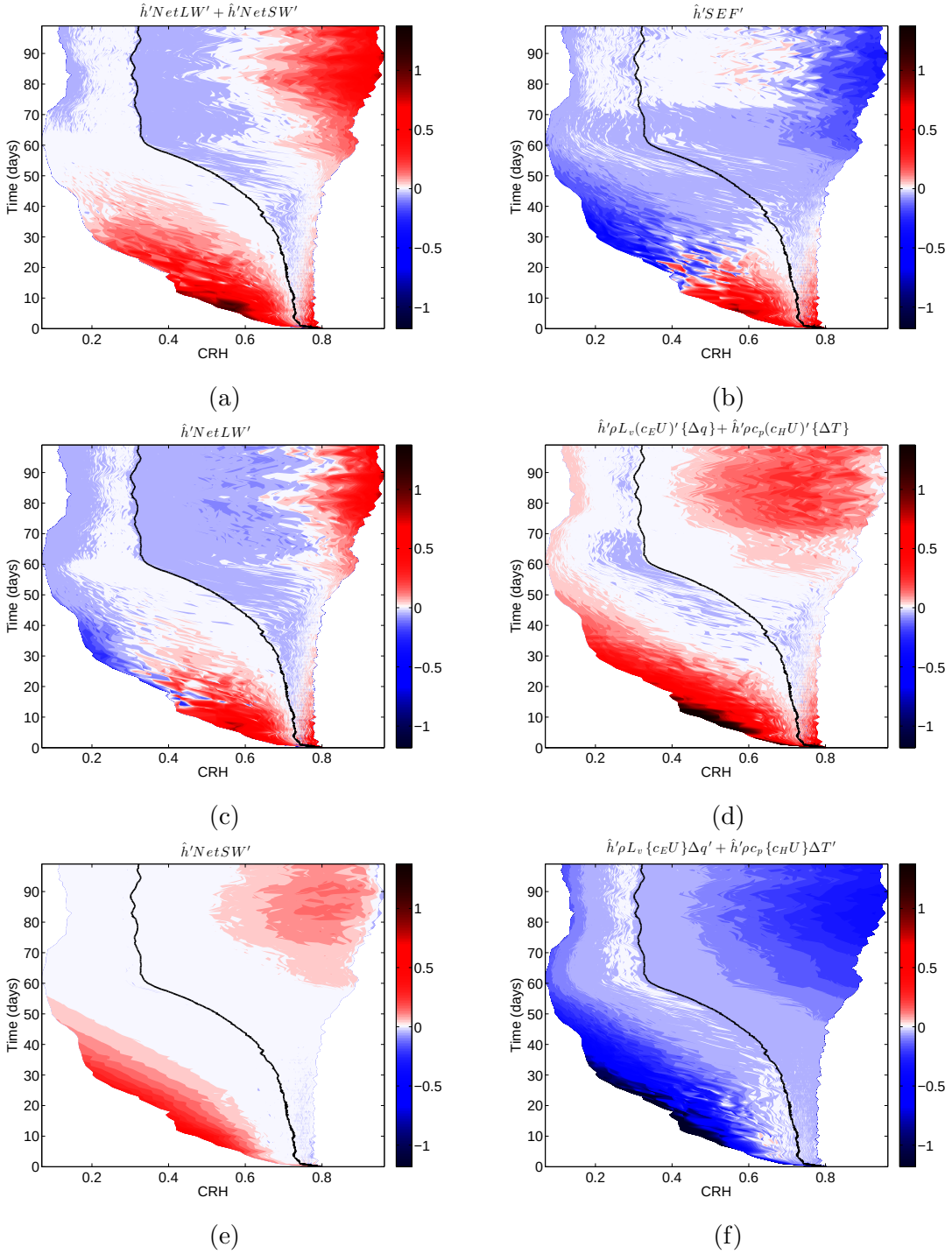

Figure B-1: Terms in the $\hat{h}'^2$ budget, plotted against column relative humidity (CRH). All terms have been averaged over each day and over 48×48 km^2 blocks, normalized by $\{\hat{h}'^2\}$, are from the simulation at 305 K, and have units of days^{-1}. On the x-axis, dry regions are on the left and moist regions are on the right, sorted according to block-averaged CRH. The black line is the $\hat{h}' = 0$ contour, plotted as a reference. Note that the color bar saturates in a few places.

Appendix C

FMSE Variance Budget at Other SSTs

The feedback analysis in terms of the budget for the spatial variance of vertically integrated frozen moist static energy is repeated for the simulations that aggregate at 301 K, 303 K, 307 K, and 310 K. The 301 K, 303 K, and 307 K simulations are performed with a domain size of 768 x 768 km^2, the same as in the 305 K simulation that was analyzed in Chapter 4. The 310 K simulation uses a larger domain of 1536 x 1536 km^2. As discussed in Chapters 2 and 3, a larger domain size is needed for higher temperature simulations to aggregate. In all cases, the terms have been averaged over each day and over 48 x 48 km^2 blocks. Because of the larger domain size of the 310 K simulation, there are 1024 such blocks, rather than 256. The results at different temperatures are very similar to those presented for the 305 K case.

The magnitudes of the normalized [1] feedback terms tend to increase slightly with SST but are generally quite comparable. The magnitude of the non-normalized feedback terms increases with SST, but $\{\hat{h}'^2\}$ also increases with SST to compensate. The range of column relative humidity values achieved are similar for the different simulations, as is the tendency for the dry regions to get drier before the moist regions get moister. The zero anomaly contour ($\hat{h}'^2 = 0$) stabilizes at approximately the same rank, indicating the moist and dry regions cover similar fractions of the domain at

[1] Normalized by the domain mean FMSE variance, $\{\hat{h}'^2\}$.

different temperatures.

As in the 305 K simulation, the LW feedback term (panel c of Figures C-1 - C-4) and surface flux feedback term (panel b of Figures C-1 - C-4) transition from being positive in the early stages of aggregation to negative in the intermediate stages. The timing of these transitions varies somewhat between simulations at different SSTs. For example, the LW feedback in the 307 K simulation (Figure C-3c) switches from positive to negative in the driest regions around day 20, while in the 310 K simulation (Figure C-4c), it doesn't change signs until day 30. The different timing of the surface flux feedback transition is related to the development of the negative air-sea disequilbrium feedback (panel f of Figures C-1 - C-4). In the 310 K simulation, the disequilibrium feedback is actually positive until day 20 (Figure C-4f), while in the 307 K simulation, a negative feedback is established right away. The longer it takes the negative disequilbrium feedback to become established, the longer the total surface flux feedback can remain positive. However, these differences in timing between the simulations at different SSTs should not be over-interpreted, since they don't depend monotonically on temperature and there are also large differences in the timing of self-aggregation in an ensemble of simulations at the same SST (Chapter 2).

The simulation at 301 K exhibits more variability during the mature phase of aggregation than the other simulations. Over periods of several days, the cluster disperses, then contracts. This variability is reflected in the feedback terms as oscillations in their strength, as well as in the spatial extent of the feedbacks in the moist region. The cause of this variability is unknown. A final notable difference between the feedback analysis at different SSTs is that the positive shortwave feedback is weaker in the 310 K simulation (Figure C-4e) than in the others. In particular, it is weaker and less widespread in the moist regions during the mature phase of aggregation. It is unknown whether this is a robust feature of self-aggregation at higher temperature, or simply random noise.

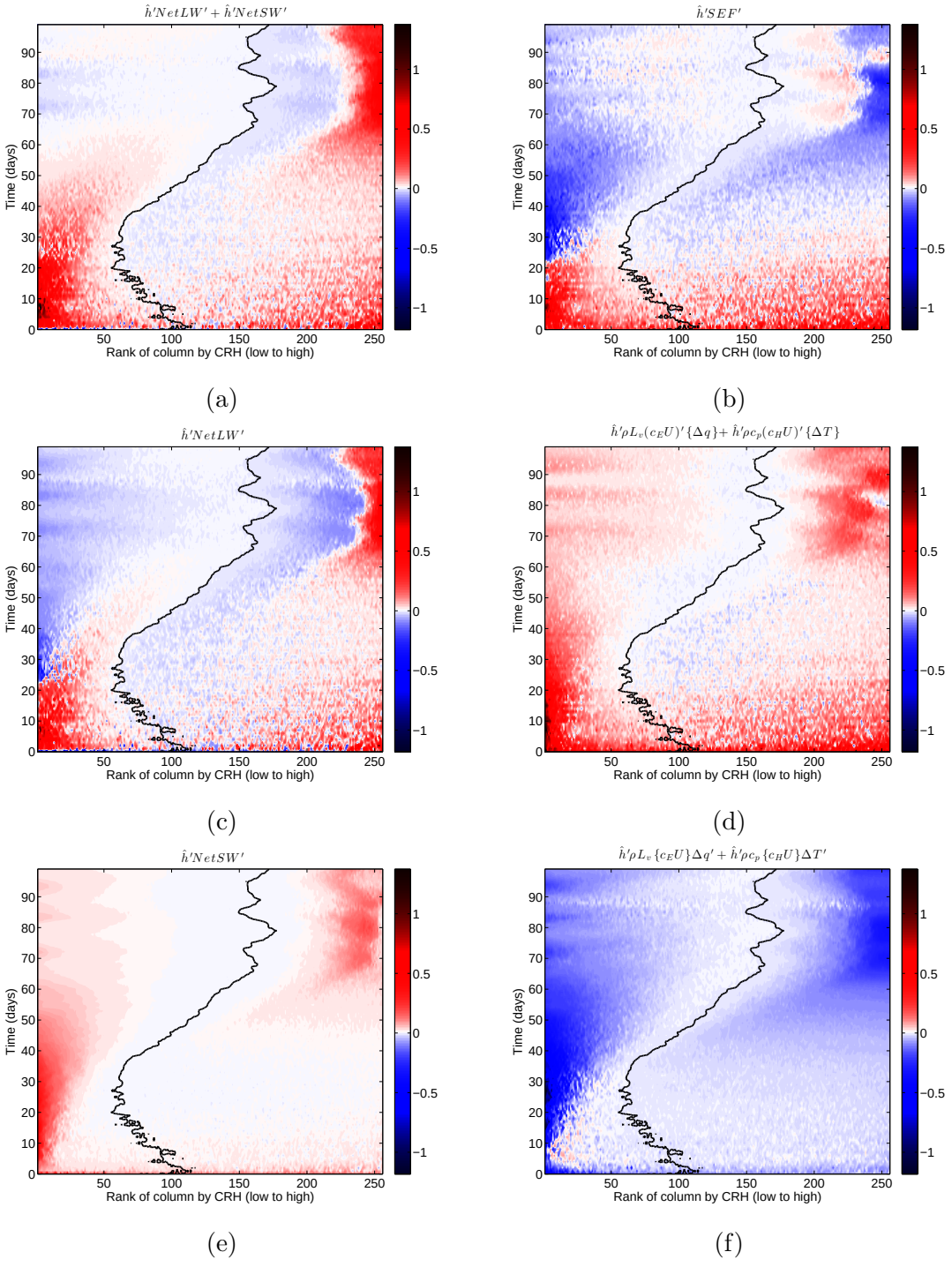

Figure C-1: Terms in the $\hat{h}'^2$ budget. All terms have been averaged over each day and over 48×48 km^2 blocks, normalized by $\{\hat{h}'^2\}$, are from the simulation at 301 K, and have units of days^{-1}. On the x-axis, dry regions are on the left and moist regions are on the right, sorted according to block-averaged CRH. The black line is the $\hat{h}' = 0$ contour, plotted as a reference. Note that the color bar saturates in a few places.

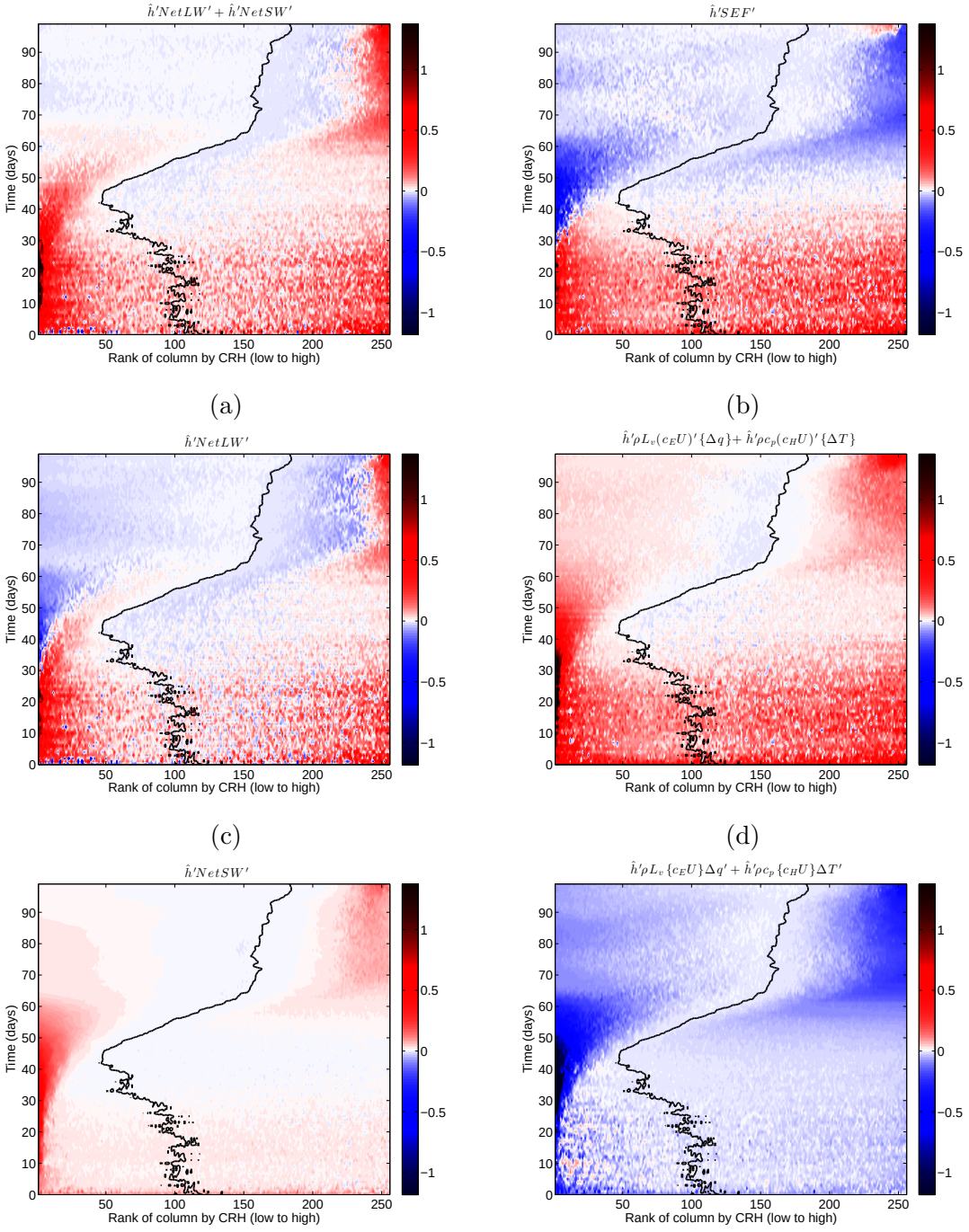

Figure C-2: Same as Figure C-1, but for simulation at 303 K.

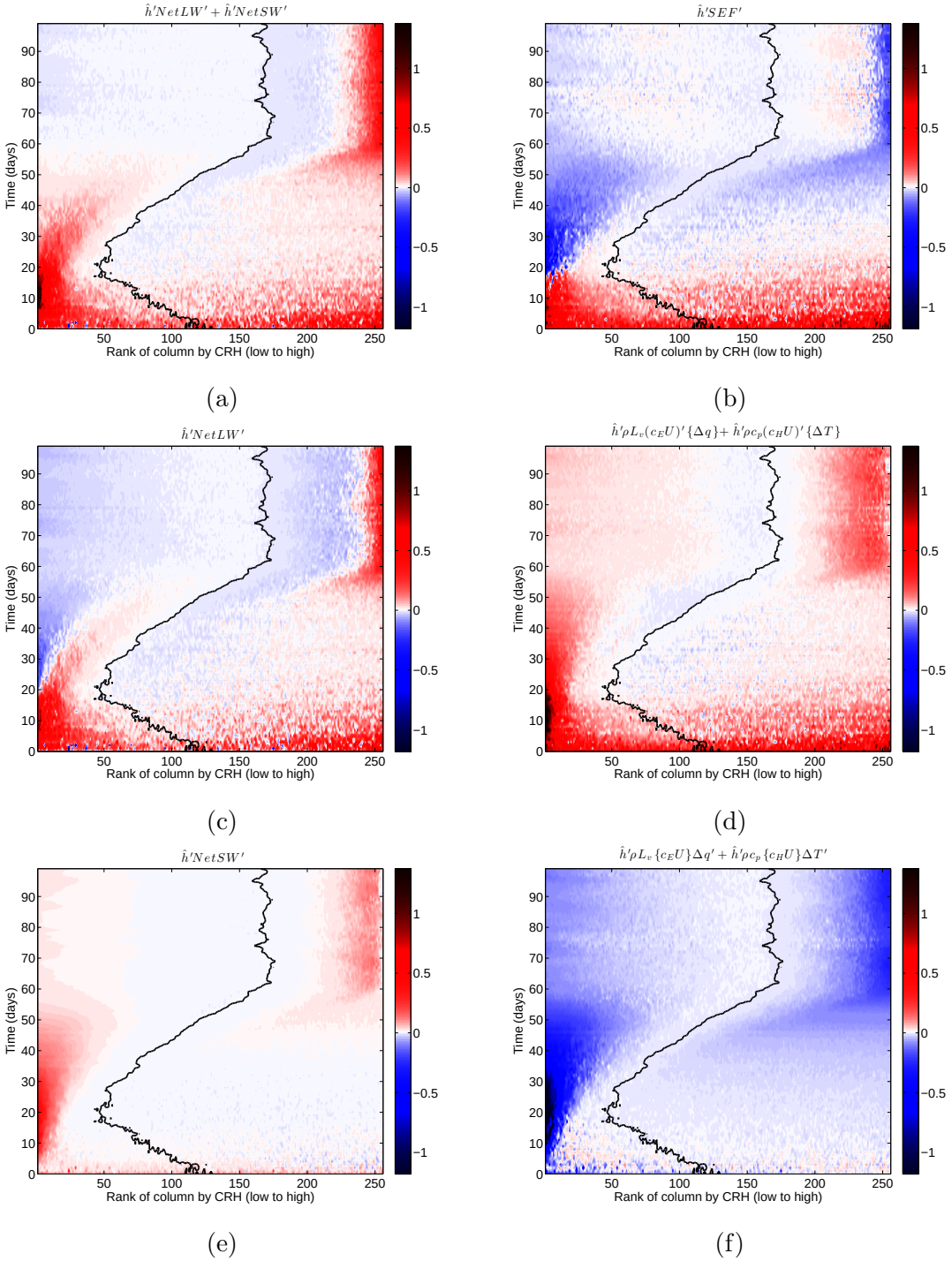

Figure C-3: Same as Figure C-1, but for simulation at 307 K.

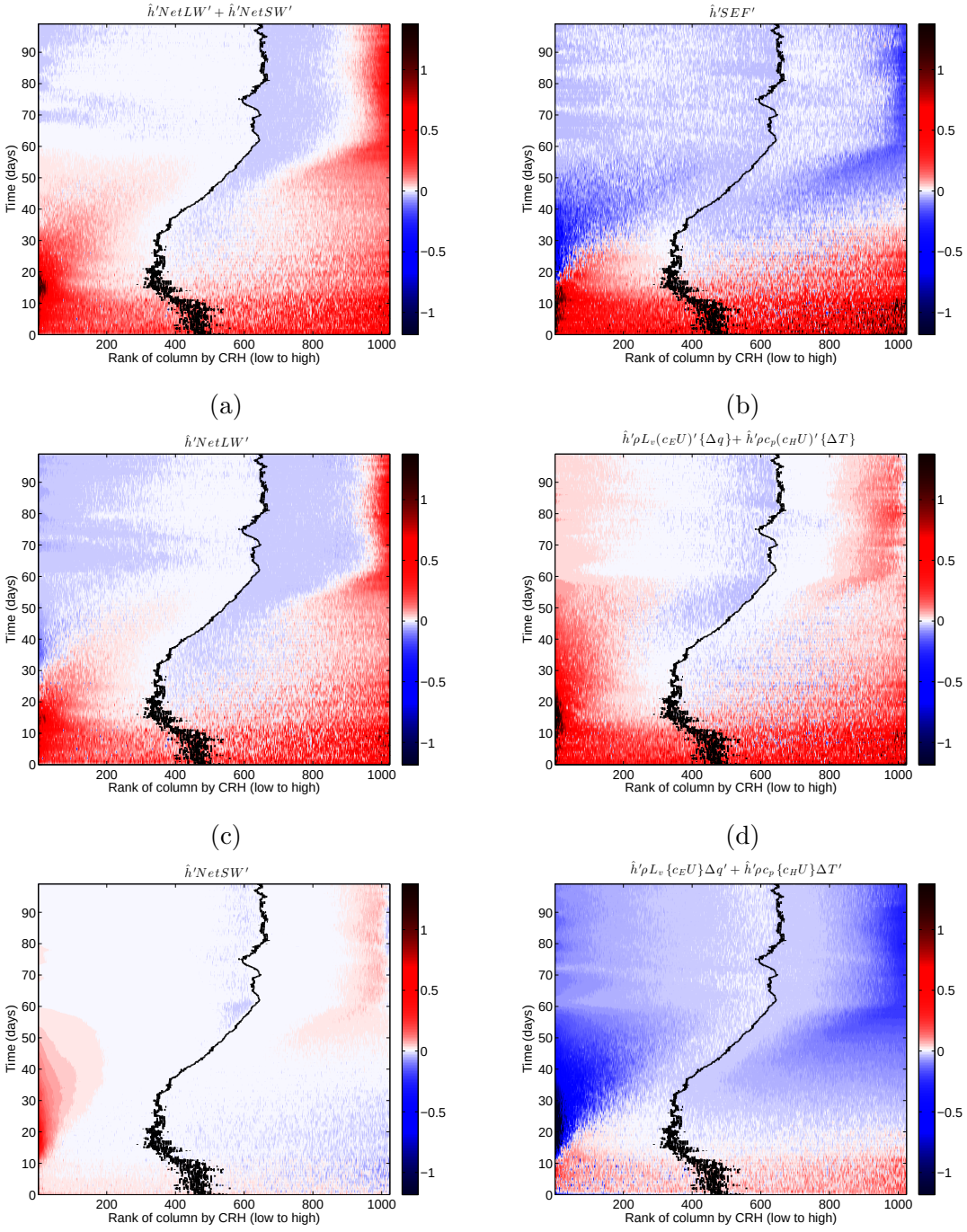

Figure C-4: Same as Figure C-1, but for simulation at 310 K.

Bibliography

Arakawa, A. and W. Schubert, 1974: Interaction of a cumulus cloud ensemble with the large-scale environment, Part I. *J. Atmos. Sci.*, **31**, 674–701.

Bony, S. and K. A. Emanuel, 2005: On the role of moist processes in tropical intraseasonal variability: cloud radiation and moisture convection feedbacks. *J. Atmos. Sci.*, **62**, 27702789.

Bretherton, C. S., P. N. Blossey, and M. Khairoutdinov, 2005: An energy-balance analysis of deep convective self-aggregation above uniform SST. *J. Atmos. Sci.*, **62**, 4237–4292.

Challa, M. and R. L. Pfeffer, 1990: Formation of Atlantic hurricanes from cloud clusters and depressions. *J. Atmos. Sci.*, **47**, 909–927.

Chavas, D. R., 2013: Tropical cyclone size in observations and in radiative-convective equilibrium. Ph.D. thesis, Mass. Inst. of Technol., Cambridge, Mass.

Chavas, D. R. and K. A. Emanuel, 2014: Equilibrium tropical cyclone size in an idealized state of radiative-convective equilibrium. *J. Atmos. Sci.*, **accepted**.

Clough, S. A., M. W. Shephard, E. J. Mlawer, J. S. Delamere, M. J. Iacono, K. Cady-Pereira, S. Boukabara, and P. D. Brown, 2005: Atmospheric radiative transfer modeling: A summary of the AER codes. *J. Quant. Spectrosc. Radiat. Transfer*, **91**, 233–244.

Collins, W. D., et al., 2006: The formulation and atmospheric simulation of the Community Atmosphere Model version 3 (CAM3). *J. Climate*, **19**, 2144–2161.

Craig, G. C. and J. M. Mack, 2013: A coarsening model for self-organization of tropical convection. *J. Geophys. Res. Atmos.*, **118**, 8761–8769, doi:10.1002/jgrd.50 674.

Dunkerton, T. J., M. T. Montgomery, and Z. Wang, 2008: Tropical cyclogenesis in a tropical wave critical layer: Easterly waves. *Atmos. Chem. Phys. Discuss.*, **8**, 11 149–11 292.

Emanuel, K., A. A. Wing, and E. M. Vincent, 2013: Radiative-convective instability. *J. Adv. Model. Earth Syst.*, **5**, doi:10.1002/2013MS000 270.

Emanuel, K. A., 1986: An air-sea interaction theory for tropical cyclones. Part I: Steady state maintenance. *J. Atmos. Sci.*, **43**, 585–604.

Emanuel, K. A., 1994: *Atmospheric Convection*. Oxford University Press, 580 pp.

Emanuel, K. A., 1995: The behavior of a simple hurricane model using a convective scheme based on subcloud-layer entropy equilibrium. *J. Atmos. Sci*, **52**, 3959–3968.

Emanuel, K. A. and D. S. Nolan, 2004: Tropical cyclone activity and global climate. Preprints. *26th Conf. on Hurricanes and Tropical Meteorology*, Miami, FL, Amer. Meteor. Soc., 240–241.

Emanuel, K. A. and M. Zivkovic-Rothman, 1999: Development and evaluation of a convection scheme for use in climate models. *J. Atmos. Sci.*, **56**, 1766–1782.

Frank, W. M. and P. E. Roundy, 2006: The role of tropical waves in tropical cyclogenesis. *Mon. Wea. Rev.*, **134**, 2397–2417.

Futyan, J. M. and A. D. Del Genio, 2007: Deep convective system evolution over Africa and the tropical Atlantic. *J. Climate*, **20**, 5041–5060.

Held, I. M., R. S. Hemler, and V. Ramaswamy, 1993: Radiative-convective equilibrium with explicity two-dimensional moist convection. *J. Atmos. Sci*, **50**, 3909–3927.

Held, I. M. and M. Zhao, 2008: Horizontally homogenous radiative-convective equlibria at GCM resolution. *J. Atmos. Sci.*, **65**, 2003–2013.

Held, I. M., M. Zhao, and B. Wyman, 2007: Dynamic radiative-convective equilibria using GCM column physics. *J. Atmos. Sci.*, **64**, 228–238.

Hennon, C. C., C. N. Helms, K. R. Knapp, and A. R. Bowen, 2011: An objective algorithm for detecting and tracking tropical cloud clusters: Implications for tropical cycloge prediction. *J. Atmos. Oceanic Technol.*, **28**, 1007–1018.

Hennon, C. C., et al., 2013: Tropical cloud cluster climatology, variability, and genesis productivity. *J. Climate*, **26**, 3046–3066.

Houze, R., 1977: Structure and dynamics of a tropical squall-line system. *Monthly Weather Review*, **105**, 1540–1567.

Houze Jr., R., 2004: Mesoscale convective systems. *Reviews of Geophysics*, **42**, RG4003.

Iacono, M. J., J. S. Delamere, E. J. Mlawer, M. W. Shephard, S. A. Clough, and W. D. Collins, 2008: Radiative forcing by long-lived greenhousegases: calculations with the AER radiative transfer models. *J. Geophys. Res.*, **113**, doi:/10.1029/2008JD009944.

Islam, S., R. L. Bras, and K. Emanuel, 1993: Predictability of mesoscale rainfall in the tropics. *J. Applied Meteor.*, **32**, 297–310.

Jeevanjee, N. and D. M. Romps, 2013: Convective self-aggregation, cold pools, and domain size. *Geophys. Res. Lett.*, **40**, doi:10.1002/grl.50204.

Khairoutdinov, M. and K. Emanuel, 2013: Rotating radiative-convective equlibrium simulated by a cloud-resolving model. *J. Adv. Model. Earth Syst.*, **5**, 816–825, doi:10.1002/2013MS000 253.

Khairoutdinov, M. F. and K. A. Emanuel, 2010: Aggregation of convection and the regulation of tropical climate. Preprints. *29th Conference on Hurricanes and Tropical Meteorology*, Tucson, AZ, Amer. Meteorol. Soc.

Khairoutdinov, M. F. and K. A. Emanuel, 2012: The effects of aggregated convection in cloud-resolved radiative-convective equilibrium. Preprints. *30th Conference on Hurricanes and Tropical Meteorology*, Ponte Vedra Beach, FL, Amer. Meteorol. Soc.

Khairoutdinov, M. F. and D. A. Randall, 2003: Cloud resolving modeling of the ARM summer 1997 IOP: Model formulation, results, uncertainties, and sensitivities. *J. Atmos. Sci.*, **60**, 607–625.

Kiehl, J. T., J. J. Hack, G. B. Bonan, B. A. Boville, D. L. Williamson, and P. J. Rasch, 1998: The National Center for Atmospheric Research Community Climate Model: CCM3. *J. Climate*, **11**, 1131–1149.

Laing, A. G. and J. M. Fritsch, 1997: The global population of mesoscale convective complexes. *Q. J. R. Meteorol. Soc.*, **123**, 389–405.

Laing, A. G. and M. Fritsch, 1993a: Mesoscale convective complexes in Africa. *Monthly Weather Review*, **121**, 2254–2263.

Laing, A. G. and M. Fritsch, 1993b: Mesoscale convective complexes over the Indian monsoon region. *J. Climate*, **6**, 911–919.

Lee, C. S., 1989: Observational analysis of tropical cyclogenesis in the western North Pacific. Part I: Structural evolution of cloud clusters. *J. Atmos. Sci.*, **46**, 2580–2598.

Liu, C. and E. J. Zipser, 2008: Diurnal cycles of precipitation, clouds, and lightning in the tropics from 9 years of TRMM observations. *Geophys. Res. Lett.*, **35**, L04 819, doi:10.1029/2007GL032 437.

Machado, L. A. T. and W. B. Rossow, 1993: Structural characteristics and radiative properties of tropical cloud clusters. *Monthly Weather Review*, **121**, 3234–3260.

Machado, L. A. T., W. B. Rossow, R. L. Guedes, and A. W. Walker, 1998: Life cycle variations of mesoscale convective systems over the Americas. *Monthly Weather Review*, **126**, 1630–1654.

Madden, R. A. and P. R. Julian, 1971: Detection of a 40-50 day oscillation in the zonal wind in the tropical pacific. *J. Atmos. Sci.*, **28**, 702–708.

Maddox, R. A., 1980: Mesoscale convective complexes. *Bull. Amer. Meteor. Soc.*, **61**, 1374–1387.

Maloney, E., 2009: The moist static energy budget of a composite tropical intraseasonal oscillation in a climate model. *J. Climate*, **22**, 711–729.

Mapes, B., R. Milliff, and J. Morzel, 2009: Composite life cycle of maritime tropical mesoscale convective systems in scatterometer and microwave satellite observations. *J. Atmos. Sci.*, **66**, 199–208.

Mapes, B. E., 1993: Gregarious tropical convection. *J. Atmos. Sci.*, **50**, 2026–2037.

Mapes, B. E. and R. A. Houze Jr., 1993: Cloud clusters and superclusters over the oceanic warm pool. *Monthly Weather Review*, **121**, 1398–1415.

Miller, D. and J. M. Fritsch, 1991: Mesoscale convective complexes in the western Pacific region. *Monthly Weather Review*, **119**, 2978–2992.

Mlawer, E. J., S. J. Taubman, P. D. Brown, M. J. Iacono, and S. A. Clough, 1997: Radiative transfer for inhomogeneous atmospheres: RRTM, a validated correlated-k model for the longwave. *J. Geophys. Res.*, **102**, 16 663–16 682.

Morrison, H., J. A. Curry, and V. I. Khvorostyanov, 2005: A new double-moment microphysics scheme for application in cloud and climate models: Part 1: Description. *J. Atmos. Sci.*, **62**, 1665–1677.

Muller, C. J., L. E. Back, P. A. O'Gorman, and K. A. Emanuel, 2009: A model for the relationship between tropical precipitation and column water vapor. *Geophys. Res. Lett.*, **36**, L16 804.

Muller, C. J. and I. M. Held, 2012: Detailed investigation of the self-aggregation of convection in cloud resovling simulations. *J. Atmos. Sci.*, **69**, 2551–2565.

Nesbitt, S. W., E. J. Zipser, and D. J. Cecil, 2000: A census of precipitation features in the tropics using TRMM: Radar, ice scattering, and lightning observations. *J. Climate*, **13**, 4087–4106.

Nolan, D. S., E. D. Rappin, and K. E. Emanuel, 2007: Tropical cyclonegenesis sensitivity to environmental parameters in radiative-convective equilibrium. *Q. J. R. Meteorol. Soc.*, **133**, 2085–2107.

Pauluis, O. and J. Schumacher, 2011: Self-aggregation of clouds in conditionally unstable moist convection. *Proc. Natl. Acad. Sci.*, **108**, 12 623–12 628.

Peters, O. and J. Neelin, 2006: Critical phenomena in atmospheric precipitation. *Nature Physics*, **2**, 393396, doi:10.1038/nphys314.

Peters, O., J. D. Neelin, and S. W. Nesbitt, 2009: Mesoscale convective systems and critical clusters. *J. Atmos. Sci.*, **66**, 2913–2924.

Rappin, E. D., D. S. Nolan, and K. A. Emanuel, 2010: Thermodynamic control of tropical cyclogenesis in environments of radiative-convective equilbrium. *Q. J. R. Meteorol. Soc.*, **136**, 1954–1972.

Raymond, D. J., 1995: Regulation of moist convection over the west pacific warm pool. *J. Atmos. Sci.*, **52**, 3945–3959.

Raymond, D. J. and Z. Fuchs, 2007: Convectively coupled gravity and moisture modes in a simple atmospheric model. *Tellus, Ser. A*, **59**, 627–640.

Raymond, D. J. and X. Zeng, 2000: Instability and large-scale circulatoin in a two-column model of the tropical troposphere. *Q. J. R. Meteorol. Soc.*, **124**, 3117–3135.

Robe, F. R. and K. A. Emanuel, 2001: The effect of vertical wind shear on radiative-convective equilibrium states. *J. Atmos. Sci.*, **58**, 1427–1445.

Sessions, S. L., S. Sugaya, D. J. Raymond, and A. H. Sobel, 2010: Multiple equilibria in a cloud-resolving model using the weak temperature gradient approximation. *J. Geophys. Res.*, **115**, D12 110, doi:10.1029/2009JD013 376.

Simpson, J., E. Ritchie, G. J. Holland, J. Halverson, and S. Stewart, 1997: Mesoscale interactions in tropical cyclone genesis. *Monthly Weather Review*, **125**, 2643–2661.

Sobel, A. and E. Maloney, 2012: An idealized semi-empirical framework for modeling the Madden-Julian Oscillation. *J. Atmos. Sci.*, **69**, 1691–1705.

Sobel, A. and E. Maloney, 2013: Moisture modes and the eastward propagation of the MJO. *J. Atmos. Sci.*, **70**, 187–192.

Sobel, A. H., G. Bellon, and J. Bacmeister, 2007: Multiple equilibria in a single-column model of the tropical atmosphere. *Geophys. Res. Lett.*, **34**, L22 804, doi:10.1029/2007GL031 320.

Sobel, A. H., E. D. Maloney, G. Bellon, and D. M. Frierson, 2008: The role of surface fluxes in tropical intraseasonal oscillations. *Nature Geoscience*, **1**, 653–657.

Stechmann, S. M. and A. J. Majda, 2009: Gravity waves in shear and implications for organized convection. *J. Atmos. Sci.*, **66**, 2579–2599.

Stephens, G. L., S. van den Heever, and L. Pakula, 2008: Radiative-convective feedbacks in idealized states of radiative-convective equilibrium. *J. Atmos. Sci.*, **65**, 3899–3916.

Tobin, I., S. Bony, C. E. Holloway, J. Y. Grandpeix, G. Seze, D. Coppin, S. J. Woolnough, and R. Roca, 2013: Does convective aggregation need to be represented in cumulus parameterizations? *J. Adv. Model. Earth Syst.*, **5**, doi:/10.1002/jame.20 047.

Tobin, I., S. Bony, and R. Roca, 2012: Observational evidence for relationships between the degree of aggregation of deep convection, water vapor, surface fluxes, and radiation. *J. Climate*, **25**, 6885–6904.

Tompkins, A. and G. Craig, 1998: Radiative-convective equilibrium in a three-dimensional cloud-ensemble model. *Q. J. R. Meteorol. Soc.*, **124**, 2073–2097.

Tompkins, A. M., 2001a: Organization of tropical convection in low vertical wind shears: The role of cold pools. *J. Atmos. Sci.*, **58**, 1650–1672.

Tompkins, A. M., 2001b: Organization of tropical convection in low vertical wind shears: The role of water vapor. *J. Atmos. Sci.*, **58**, 529–545.

Velasco, I. and J. M. Fritsch, 1987: Mesoscale convective complexes in the Americas. *J. Geophys. Res.*, **92**, 9591–9613.

Wing, A. A. and K. A. Emanuel, 2012: Organization of tropical convection: dependence of self-aggregation on SST in an idealized modeling study. Preprints. *30th Conference on Hurricanes and Tropical Meteorology*, Ponte Vedra Beach, FL. Amer. Meteorol. Soc.

Wing, A. A. and K. A. Emanuel, 2013: Physical mechanisms controlling self-aggregation of convection in idealized numerical modeling simulations. *J. Adv. Model. Earth Syst.*, **5**, doi:10.1002/2013MS000 269.

Xu, K. and K. A. Emanuel, 1989: Is the tropical atmosphere conditionally unstable? *Mon. Wea. Rev.*, **117**, 1471–1479.

Yuan, T., 2011: Cloud macroscopic organization: order emerging from randomness. *Atmospheric Chemistry and Physics*, **11 (15)**, 7483–7490, doi:10.5194/acp-11-7483-2011.

Zhou, W., I. Held, and S. Garner, 2014: Parameter study of tropical cyclones in rotating radiative-convective equilibrum with column physics and resolution of a 25 km GCM. *J. Atmos. Sci.*, **in press**, doi:10.1175/JAS–D–13–0190.1.